UNIVERSITÀ
DEGLI STUDI
DI PADOVA

Sede amministrativa: Università degli Studi di Padova
Dipartimento di Fisica e Astronomia

SCUOLA DI DOTTORATO DI RICERCA IN: ASTRONOMIA
CICLO XXVIII

CLUSTERING AND LENSING PROPERTIES OF DARK MATTER HALOES IN EUCLID ERA

Direttore della scuola: Ch.mo Prof. Giampaolo Piotto
Supervisore: Ch.mo Prof. Giuseppe Tormen
Co-Supervisore: Dott. Massimo Meneghetti

Dottorando: Michele Boldrin

Contents

Abstract

Following the most accredited cosmological model, the ΛCDM model, only 4% of the Universe is formed by baryonic matter, while about 26% is made up of Cold Dark Matter (CDM) and the remaining 70% is given by the component responsable of the cosmic accelerated expansion, called dark energy or Λ. Primordial perturbations in the CDM distribution that oppose to cosmic expansion and begin to collapse origin the potential wells where baryonic matter condense to form galaxies and stars. Observed on scales minor than some Mpc, the Universe is far from being homogeneous: galaxies are embedded by collapsed dark matter haloes. Therefore, the study of the substratum of dark matter in which the baryonic matter lies is fundamental to understand the formation and evolution of cosmic structures.

Every object we observe come from an aggregation history of dark matter haloes, which generally enter in a host halo and orbit around the center of mass, becoming satellites. During this motion, several dynamical phenomenons may cause partial or total satellite mass-loss, or they can brake it through loss of angular momentum, so the satellite fall in the center of the host halo. In any case, the evolution of the satellite mass is very different from the evolution of a single halo. In this work we analyse the average relations between the satellite mass at the time of accretion and the mass at a given later observation moment. In particular, we wonder how can we estimate the former by the latter and viceversa. Using the new set of cosmological simulations `LE SBARBINE`, developed in the Physics and Astronomy Department of the University of Padova, we test the law that regulates the average mass-loss rate of satellites and we develop a new relation between the mass observed at a certain redshift and the average mass it could have at the accretion time. Furthermore, we discuss some factors that originate anomallies in the satellite mass evolution with respect to the average law we found, with particular attention to major mergers.

In the context of the structure formation, galaxy clusters rapresent the last phase of the aggregation process of dark matter haloes. Being the largest and more recent objects in the Universe, every their feature or behaviour is a probe for the reference cosmological model. This is even more important in this epoch of technological progress, as the statistical study of these objects requires large and deep observations. An optimal example of those future innovative instruments is given by the spatial telescope Euclid (ESO), which will be launched in $2019 - 2020$ and will observe a main 15000 $\deg^2$ of extragalactic sky, collecting images and spectra with excellent resolution and quality in optical and NIR bands. One of the research field that will be mostly improved by future observations is arc statistics, that is the cosmological research through the observation of giant gravitational arcs, the most magnificent effects of strong gravitational lensing. In the last decades, the study and the observations of gravitational lensing phenomenons has increased, following the rate of technological development. In particular, giant

gravitational arcs, which are mainly created by galaxy clusters, need detailed and deep observations to be identified and used in statistical inventigations. Because of the strong dependence of the number of those objects in the sky on the cosmology, we study as the number of arcs visible in the main survey of Euclid is dependent on the cosmological parameters Ω_m and σ_8, the two that mostly determine the structure formation process. Moreover, we analise the effect of the survey size and of the application of a selection function on our estimates.

The thesis is structured as follows:

- in Chapters 1 and 2 we introduce the cosmological ΛCDM model;
- in Chapter 3 we briefly describe the methods for numerical simulations, we give some features of the two simulations we will deal with, namely `GIF2` and `LE SBARBINE` and we describe the methods usedin both of them to identify haloes and to define their accretion history;
- in Chapter 4, after a description of the code we developed and the consistency tests with previous works, we present the results obtained in the frame of satellite statistics;
- in Chapter 5 we briefly introduce the formalism of gravitational lensing;
- in Chapter 6 we present the spatial telescope Euclid and the method adopted to estimate the theoretica number of arcs visible in the sky, then we describe the study of the influence on this number of cosmological parameters Ω_m and σ_8, with a discussion about the effect given by the survey size and the selection function.

Sommario

Secondo il più accreditato modello cosmologico oggigiorno, il modello ΛCDM, solamente il 4% dell'Universo sarebbe composto da materia barionica, mentre circa il 26% sarebbe formato da materia oscura fredda (CDM) e il restante 70% da una componente ritenuta responsabile dell'espansione cosmica accelerata, chiamata energia oscura o Λ. Le perturbazioni primordiali nella distribuzione di CDM che vincono l'espansione cosmica e riescono a contrarsi, formano le buche di potenziale nelle quali la materia barionica condensa formando galassie e stelle. Osservato su scale minori di circa 1 Mpc, l'Universo è quindi tutt'altro che omogeneo: la materia oscura collassata in aloni ospita le galassie che noi osserviamo. Lo studio della formazione del substrato di materia oscura nel quale è ospitata la materia barionica condensata risulta perciò di fondamentale importanza per capire la formazione e l'evoluzione delle strutture cosmiche.

Ogni oggetto che osserviamo deriva da una storia di aggregazione di aloni di materia oscura, i quali generalmente entrano in un alone ospite e orbitano attorno al suo centro di massa, divenendo suoi satelliti. Durante questo moto, vari fenomeni dinamici possono causare perdita di massa parziale o totale del satellite, oppure possono frenarlo facendogli perdere momento angolare e quindi spiraleggiare verso il centro dell'ospite. In ogni caso, l'evoluzione della massa del satellite risulta molto diversa dall'evoluzione di un alone singolo. In questo lavoro analizziamo le relazioni medie fra la massa dei satelliti al momento dell'accrescimento e la massa ad un certo momento di osservazione. In particolare, ci domandiamo come stimare la prima dalla seconda e viceversa. Facendo uso del nuovo set di simulazioni cosmologiche `LE SBARBINE`, sviluppato nel dipartimento di Fisica e Astronomia dell'Università di Padova, testeremo la legge precedentemente trovata per il tasso medio di perdita di massa dei satelliti e svilupperemo una relazione fra la massa osservata di un satellite ad un certo redshift e la massa media che aveva al momento dell'accrescimento. Inoltre commenteremo i fattori che determinano delle anomalie nell'evoluzione della massa dei satelliti rispetto alla legge trovata, con particolare attenzione ai major mergers.

Nel contesto della formazione delle strutture, gli ammassi di galassie rappresentano l'ultimo stadio del processo di aggregazione di aloni di materia oscura. Essendo gli oggetti più grandi e più giovani dell'Universo, ogni loro caratteristica o comportamento funziona da test per il modello cosmologico di riferimento. Questo è ancora più importante in questa epoca di forte progresso tecnologico, poiché lo studio statistico di tali oggetti richiede osservazioni di porzioni di cielo più estese possibili e con ottima risoluzione. Un ottimo esempio di futuri strumenti innovativi è il telescopio spaziale Euclid, dell'European Spatial Observatory, che verrà lanciato nel $2019 - 2020$ e osserverà 15000 gradi quadri di cielo extragalattico raccogliendo immagini e spettri di eccellente qualità in ottico e vicino infrarosso. Uno dei campi di ricerca che verranno maggiormente rivoluzionati dalle future osservazioni è quello della statistica degli archi,

ovvero la ricerca cosmologica attraverso l'osservazione di archi gravitazionali giganti, i più eclatanti effetti di lensing gravitazionale forte. Negli ultimi decenni, infatti, lo studio e le osservazioni dei fenomeni di lensing gravitazionale è andato via via aumentando, di pari passo con lo sviluppo tecnologico. In particolare, gli archi gravitazionali giganti, prodotti dagli ammassi di galassie, necessitano di osservazioni dettagliate e profonde per essere identificati e utilizzati in studi di tipo statistico. Data la forte dipendenza cosmologica del numero di questi oggetti visibili nel cielo, ci proponiamo di studiare come il numero di archi visibili nella survey principale di Euclid è dipendente dai parametri cosmologici Ω_m e σ_8, i due che maggiormente influenzano la formazione delle strutture. Inoltre, abbiamo analizzato l'effetto della dimensione della survey e dell'applicazione di una funzione di selezione sulle nostre previsioni.

La tesi è strutturata come segue:

- nei Capitoli 1 e 2 introduciamo il modello cosmologico ΛCDM;
- nel Capitolo 3 descriviamo brevemente le tecniche di simulazione numeriche, diamo le caratteristiche delle due simulazioni cosmologiche che tratteremo nel lavoro, ovvero le `GIF2` e `LE SBARBINE` e descriviamo i metodi utilizzati in entrambe le simulazioni per l'dentificazione degli aloni e la definizione della loro storia di accrescimento;
- nel Capitolo 4, dopo aver descritto il codice usato per il nostro lavoro e i test di consistenza con i lavori precedenti, presentiamo i risultati ottenuti nell'ambito della statistica dei satelliti di materia oscura;
- nel Capitolo 5 introduciamo brevemente il formalismo del lensing gravitazionale;
- nel Capitolo 6 presentiamo il telescopio spaziale Euclid e il metodo utilizzato per dare una stima teorica del numero di archi nel cielo osservati da Euclid, poi illustriamo lo studio dell'influenza su tale numero dei parametri cosmologici Ω_m e σ_8, accompagnato da una discussione sull'effetto della dimensione della survey e della funzione di selezione.

Chapter 1

The Smooth Universe

The first step toward a description of the Universe is the construction of a robust thoretical model which describes what we observe. Such a model must lie on the known physics and it must depend on the minimum number of assumptions as possible. Nowadays, the most accredited cosmological model is given by the *Big Bang* theory, together with the *inflation* theory.

1.1 The Robertson-Walker Metric

The starting point of the Big Bang model is the *cosmological principle*: on large scale, namely on scales of about hundred Mpc, the Universe appears isotropic and homogeneous, that is the density of cosmic structures is the same in every point, so there is no special positions or direction. Before the descovering of the Cosmic Microwave Background (CMB) and the expansion of the Universe, the cosmological principle was also said *perfect*, so there were no preferred times (the Universe was supposed to be static) and the creation of matter from nothing was an allowed thought. The discover of the CMB put some new problems such as the creation of photons from nothing and the expansion of the Universe, and it was clear the Universe was not static and the adjective *perfetto* was not used anymore. Nevertheless, the CMB proves the Universe homogeneity, because the average observed temperature fluctuation is in the order of 10^{-5}.

The second assumption we take to build our cosmological model is that the gravitational force dominates on the other fundamental forces on large scale. Gravity behaviour is well described by Einstein's General Relativity, which states that the geometrical properties of space-time are defined by its energetic content.

The general metric in space-time which established a relation between two points with different t, x, y and z coordinates has the followin form:

$$\mathrm{d}s^2 = g_{\alpha\beta}\mathrm{d}x^\alpha \mathrm{d}x^\beta = g_{00}\mathrm{d}t^2 - 2g_{0i}\mathrm{d}t\mathrm{d}x^i - g_{ij}\mathrm{d}x^2, \tag{1.1}$$

where $g_{\alpha\beta}$ is the metric tensor and $\alpha, \beta = 0, 1, 2, 3$ are the space-time coordinates ($i, j = 1, 2, 3$ identify the spatial ones).

Assuming isotropy and homogeneity, we obtain the *Robertson-Walker* metric:

$$\mathrm{d}s^2 = c^2\mathrm{d}t^2 - a^2(t)[\frac{\mathrm{d}r^2}{1 - Kr^2} + r^2(\mathrm{d}\theta^2 + \sin^2\theta\mathrm{d}\phi^2)], \tag{1.2}$$

where r, θ e ϕ are the comoving sferic coordinates, t is the cosmic time, $a(t)$ is the *scale factor*, which contains the dependence on time of the spatial part of the metric, and k is the *curve parameter*. the space can be thought as a sum of iper-surveys at different times, and their shape depends on the cosmic geometry, we may be flat, spherical or hyperbolic depending on the value of k, 0, 1 or -1.

1.2 Redshift

An important quantity related to the scale factor is the *redshift*, which is defined as

$$z \equiv \frac{\Delta\lambda}{\lambda} = \frac{\lambda_{obs} - \lambda_{th}}{\lambda_{th}}, \tag{1.3}$$

that is the difference between the observed and the theoretical wavelenghts λ of a radiation. The wavelenght of a radiation emitted by a far source is connected to the scale factor through the relation

$$\frac{a_0}{\lambda_0} = \frac{a_E}{\lambda_E},$$

where subscripts 0 and E indicate the time of observation and the time of emission, respectively. Using eq. (1.3), the relation could be written as

$$1 + z_E = \frac{a_0}{a_E}. \tag{1.4}$$

Hence, since the scale factor a is a monotonically increasing function of time, its variation from t_E to t_0 causes a net shift of the observed wavelenght toward the redder regions of the spectrum. If we define today as t_0 and $a(t_0) = 1$, we can write

$$1 + z = \frac{1}{a(t)}.$$

Thus, the redshift tells how much far from us is a source along the space-time, relating an observable, λ, to a cosmological factor, $a(t)$.

1.3 The Friedmann Equations

In order to know how the scale factor evolves with time, we need to solve Einstein's field equation:

$$R_{ij} - \frac{1}{2}g_{ij}R - \Lambda g_{ij} = \frac{8\pi G}{c^4}T_{ij}, \tag{1.5}$$

where R is the Ricci's tensor, g is the metric tensor and T is the energy-impulse tensor. The term Λg_{ij} was added my Einstein to obtain a model of a static Universe, but it was removed after the discover of the cosmic expansion. During the last decades the term Λ has been reconsidered to explain the accelerated expansion of the Universe, and it represents the contribute of the Dark Energy on the field equation.

Friedmann solved the filed equation through the following two assumptions:

- the cosmological principle, thus g is given by the Robertson-Walker metric;
- the matter that fills the Universe is thgouth as a perfect fluid, so the energy-impulse tensor has the shape $T_{ij} = -Pg_{ij} + (P + \rho c^2)u_i u_j$, where P is the pression, ρ the mean density and u_i is the velocity quadrivector.

Friedmann's solutions are therefore:

$$\left(\frac{\ddot{a}}{a}\right) = -\frac{4\pi G}{3}\left(\rho + \frac{3P}{c^2}\right) \tag{1.6}$$

$$\left(\frac{\dot{a}}{a}\right)^2 = \frac{8\pi G}{3}\rho - \frac{Kc^2}{a^2} + \frac{\Lambda c^2}{3}, \tag{1.7}$$

both linked to the condition of an adiabatic expansion of the Universe

$$\frac{\mathrm{d}}{\mathrm{d}t}\left(a^3\rho c^2\right) - P\frac{\mathrm{d}a^3}{\mathrm{d}t} = 0. \tag{1.8}$$

In order to solve this system, we need a state equation that connect the pression to the density. The most general form is

$$P = w\rho c^2, \tag{1.9}$$

where the value of w depends on the considered component of the Universe, since it is given by the medium sound velocity (dealing with Dark Matter, which is non-collisional, we will talk about velocity dispersion instead of sound velocity). Typically, matter has thermal velocities much smaller than c^2, so $P \ll \rho c^2$; photons and relativistic particles have the state equation $P_R = \frac{1}{3}\rho_R c^2$; in order to get the state equaion of Dark Energy, we recover the energy-impulse tensor from the field equation in empty space

$$\Lambda g_{ij} = \frac{8\pi G}{c^4}T_{ij} \to T_{ij} = \frac{\Lambda c^4}{8\pi G}g_{ij}$$

given that $T_{ij} = -Pg_{ij} + (P + \rho c^2)u_i u_j$, hence we obtain

$$P_\Lambda = -\frac{\Lambda c^4}{8\pi G} \quad \text{e} \quad P\rho c^2 = 0 \to P = -\rho c^2. \tag{1.10}$$

Therefore, the parameter w in the state equation may have the following values:

$$w = \begin{cases} 0 & \text{matter} \\ 1/3 & \text{radiation} \\ -1 & \text{cosmological constant} \end{cases} \tag{1.11}$$

From equations (1.8) and (1.9) we can express the density ρ in term of $a(t)$ and w:

$$\rho_{0,w} \propto a^{-3(1+w)}. \tag{1.12}$$

1.4 Cosmological Distances

In the contest of General Relativity, where the metric contains a dependece on time, distance is an ambiguous concept. There are many definitions of distance, depending on the way it is measured. Here we list the main ones.

Proper distance: iti s given taking $\mathrm{d}t^2 = 0$ e aligning θ and ϕ along the observed direction, thus $\mathrm{d}\theta = \mathrm{d}\phi = 0$

$$d_P = \int \mathrm{d}s = \int_0^r \frac{a\mathrm{d}r'}{\sqrt{1 - Kr^2}} = a(t)f(r) \qquad \text{with} \qquad f(r) = \begin{cases} \arcsin r & K = 1 \\ r & K = 0 \\ \operatorname{arcsinh} r & K = -1 \end{cases}$$

Comoving Distance

It is defined as the proper distance computed today, at time $t = t_0$:

$$d_C = d_P(t = t_0) = a_0 f(r) = \frac{a_0}{a(t)} d_P.$$

The relation between the proper distance at time t_0 and at an arbitrary t implies a time variation of d_P, so we can derive it and get the recession velocity of objects from the observer:

$$v_R = \frac{\mathrm{d}}{\mathrm{d}t} d_P = f(r) \frac{\mathrm{d}a(t)}{\mathrm{d}t} = f(r)\dot{a} = \frac{\dot{a}(t)}{a(t)} d_P = (1+z) d_P.$$

This relation is known as the *Hubble law*: objects move away from the observer with a velocity which is proportional to the proper distance and it is normalized with the quantity

$$H(t) \equiv \frac{\dot{a}(t)}{a(t)}, \tag{1.13}$$

called *Hubble constant*. Since measurements of $H(t_0) \equiv H_0$ have still large uncertainty, the parameter h is used instead of H_0, such that

$$H_0 = 100 \times h \quad \mathrm{Km/s/Mpc},$$

so h lie in the range $\sim [0.5 - 1]$. Recent observations state[1] that $H_0 \approx 70$ km/s/Mpc, so $h \approx 0.7$. Another important parameter for the Universe dynamic is the so-called *deceleration parameter*, defined as

$$q = -\frac{\ddot{a}a}{\dot{a}^2},$$

which express the amount of deceleration of the Universe at a given z.

Luminosity Distance

The flux we get from a distant source decreases with the distance following the law $F = \dfrac{L}{4\pi d^2}$, where L is the absolute luminosity. Through this relation, astrophysicians get the distance d of standard candles, that is objects with known absolute luminosity. In dealing with cosmological distances, one must cosider the effects of the Universe expansion and the time dilation, both predicted by the General Relativity, which together give a contribute $(a(t)/a_0)^2$, so we the relation between flux and distance is rescaled in the following way:

$$F = L \left(\frac{\mathrm{d}t'}{t_0} \frac{a(t')}{a_0} \frac{1}{4\pi a_0^2 r^2} \right) = \frac{L}{4\pi a_0^2 r^2} \frac{1}{(1+z)^2} \equiv \frac{L}{4\pi d_L}. \tag{1.14}$$

The luminosity distance is defined as $d_L(z) \equiv a_0 r(1+z)$, and it satisfy the relation (1.14).

[1] A large amount of method to estimate h_0 exist; the most established one is based on the derivation of the luminosity distance of objects with known average absolute magnitude and spectroscopic redshift, knwon as *distance indicators* (some examples are Cepheids variable stars, supernovae, HII regions, globular clusters and very luminous galaxy clusters). More recent methods make use of the *Sunyaev-Zel'dovich effect*, that is the inverse Compton interaction between CMB photons and very energetic particles which form the hot gas halo in galaxy clusters. The variation of the CMB flux in such regions, together with the X flux from the hot gas, allows the estimation of the cluster distance, that is a function of h_0. An even more recent method goes through the gravitational lensing effect, but it is still very rough.

Angular Diameter Distance

The intrinsic and apparent sizes of objects are linked each other by the object distance. We define the apparent size as the angle covered in the sky by the object $\delta\theta$ and the proper size as D_{PR}, the angular diameter distance is

$$d_A = \frac{D_{PR}}{\delta\theta}. \tag{1.15}$$

An expression for D_{PR} is given by the Robertson-Walker metric just fixing $\mathrm{d}t = \mathrm{d}\phi = 0$,

$$D_{PR}^2 = \mathrm{d}s^2 = a^2(t) r^2 \mathrm{d}\theta^2 \rightarrow D_{PR} = ar\delta\theta,$$

thus the equation (1.15) becomes

$$d_A = a(t)r = \frac{d_L}{(1+z)^2}. \tag{1.16}$$

The equation (1.16) tells that $d_L \neq d_A$, as they are two operative distance definitions that can be used if there are standard candles available or if the proper size of the object are known.

1.5 The Friedmann Models

We use equation (1.13) to expand the second Friedmann equation (1.7):

$$H^2 = \frac{8\pi G}{3}\rho - \frac{Kc^2}{a^2} \quad \rightarrow t = t_0 \rightarrow \quad H_0^2 = \frac{8\pi G}{3}\rho_0 - \frac{Kc^2}{a_0^2}. \tag{1.17}$$

From the equation above we derive an expression for the curvature parameter $K = \frac{1}{c^2}\left[H_0^2 - \frac{8\pi G}{3}\rho_0\right]$ and define the *critical density*, that is the average density for the Universe to be flat, in other words the density in order to get $K = 0$:

$$\rho_{0,cr} \equiv \frac{3H_0^2}{8\pi G} = 2.775 \times 10^{11} h^2 \; M_\odot / Mpc^3. \tag{1.18}$$

Measuring the density of the Universe in terms of $\rho_{0,cr}$, we define the *density parameter* $\Omega \equiv \rho_0/\rho_{0,cr}$ and relate it with the curvature parameter, so that the geometry of the Universe is given by its the matter content:

$$\begin{cases} K = 0 \quad \rightarrow \quad \rho_0 = \rho_{0,cr} \quad \rightarrow \quad \Omega_0 = 1 \quad \text{piatta} \\ K = 1 \quad \rightarrow \quad \rho_0 > \rho_{0,cr} \quad \rightarrow \quad \Omega_0 > 1 \quad \text{sferica} \\ K = -1 \quad \rightarrow \quad \rho_0 < \rho_{0,cr} \quad \rightarrow \quad \Omega_0 < 1 \quad \text{iperbolica} \end{cases} \tag{1.19}$$

Thus, it is clear how much important is the precise measurement of the parameter Ω_0. To date, the best estimate of Ω_0 is given by CMB Planck observations by the Planck mission (Planck Collaboration et al. 2011), and it is very close to 1. If we put the exact value of w in equation (1.12), we obtain the density trend for every component:

- if $w = 0 \quad \rightarrow \quad \rho_M \propto a^{-3}$, matter density is inversely proportional to the volume, as expected;

- if $w = 1/3 \quad \rightarrow \quad \rho_R \propto a^{-4}$, the radiation density is diluted in space, as matter, so we find a factor a^{-3}, but another factor a^{-1} accounts for the effect of redshift on the wavelenght;

- if $w = -1 \quad \rightarrow \quad \rho_\Lambda \propto a^0 = const$, Λ gives a constant energetic contribute[2].

Altought every component has always existed, those different dependences on time imply that at different ages of the Universe only one component (with the largest energetic contribute) dominated. We write the equation that regulates the dynamics of the Universe combining the second Friedmann equation (1.7), equation (1.12) and the definitions of Hubble constant and density parameter

$$H(t)^2 = H_0^2 \left(\frac{a_0}{a}\right)^2 \left[\left(1 - \sum_i \Omega_{0,w_i}\right) + \sum_i \Omega_{0,w_i} \left(\frac{a_0}{a}\right)^{1+3w_i}\right]. \tag{1.20}$$

The first term we find inside the square brackets is the so-called *curvature density parameter*, as the difference among $\sum_i \Omega_{0,w_i}$ and 1 returns the cosmic geometry, while the second one is the sum of contributes from all components. From the Hubble law it is clear that today $\dot{a}_0 > 0$, thus now the Universe is expanding. In order to test if $\dot{a}(t) > 0$ for every t, we study $\ddot{a}$ by combining the equation (1.9) to the first Friedmann equation (1.6), and obtaining:

$$\ddot{a} = -\frac{4\pi G}{3} \rho \, (1 + 3w) \, a. \tag{1.21}$$

The sign of $\ddot{a}$ is given only by the term inside the brackets:

- if $1 + 3w < 0 \rightarrow w < -1/3$ then $\ddot{a} > 0$, the expansion is accelerated;

- if $1 + 3w > 0 \rightarrow w > -1/3$ then $\ddot{a} < 0$, the expansion is decelerated.

The only component who could satisfy the condition of accelerated expansion is Λ. Hence a is a monotonically increasing function of time with the concavity downward, so walking back the timeline we will necessarily find the point when $t \equiv 0$ and $a = 0$, that is the Big Bang, which is predicted by all Friedmann models. We still have not the instruments to study this particular moment yet, when $\rho, T, E \rightarrow \infty$, but theorists are working to develop a quantistic gravitation theory which described the big unification that occurred close to the Big Bang. The only two ways we have to reject the Big Bang theory are

1. violating one of hypotesis of the Friedmann models;

2. presuming that near to the Big Bang Λ was the dominant component.

Let's neglect Λ for a while and continue with the analysis of Friedmann models.

[2]Cosmological models with the Dark Energy parameter of state $w = w(z)$ have been recently developed, and they are known as *quintessence* models.

Analytical Solutions In A Flat Universe: The Einstein-de Sitter Model

We consider a flat Universe, so $\Omega_0 = 1$, and we solve the equation (1.20), which becomes:

$$\left(\frac{\dot{a}}{a_0}\right)^2 = H_0^2 \left(\frac{a_0}{a}\right)^{1+3w}.$$

The integration leads to

$$a(t) = a_0 \left(\frac{t}{t_0}\right)^{\frac{2}{3(1+w)}} = \begin{cases} t^{2/3} & \text{matter} \\ t^{1/2} & \text{radiation} \end{cases} \tag{1.22}$$

The expansion is slower when radiation dominates, even if the radiation pressure is larger, because from the first Friedmann equation (1.6) $\ddot{a} = -\frac{4\pi G}{3}(\rho + 3P/c^2)a$ we see that the larger P, the smaller $\ddot{a}$, so the pression brakes the expansion. This models is called *Einstein-de Sitter model*, hereafter Eds. In a Eds model the deceleration parameter is given by the following

$$q = \frac{4\pi G}{3H^2}\rho_M = \frac{1}{2}\Omega_M, \tag{1.23}$$

and we note that in such an Universe it is not possible to have an accelerated expansion, as $q > 0$ always.

Solutions In Curve Universes

The first thing we wonder is in which moment in the history of the Universe the curvature became non-negligible. Equation (1.20) presents two contributes, one for curvature and the other one for density, so one may dominate the other one, depending on time. Comparing those two factors, we find z_* so that for every $z > z_*$ we neglect the curvature, and $z_* \approx 1/\Omega_0$. Since from observations we know that Ω_0 is surely greater than 0.1, the curvature factor becomes important only at low redshifts. Hence, almost all the history of the Universe can be studied with the Eds model equation.

What happens when $z < z_*$? If we assume an open Universe, so $\Omega_{0,w} < 1$, and a negligible density factor with respect to the curvature term, equation (1.20) becomes:

$$\left(\frac{\dot{a}}{a_0}\right)^2 = H_0^2(1 - \Omega_{0,w})$$

that is constant in time. Therefore, the integration returns

$$a = a_0 H_0 \sqrt{1 - \Omega_{0,w}}\ t. \tag{1.24}$$

The expansion is free and linear with time, and since $\dot{a} = costante$, $\ddot{a} = 0$, it is neither decelerated nor accelerated.

Assuming a closed Universe, so $\Omega_{0,w} > 1$, the curvature factor of equation (1.20) is negative, so for a given value of a we have $\dot{a} = 0$, which corresponds to the moment when $\Omega_{0,w}\left(\frac{a_0}{a}\right)^{1+3w} = \Omega_{0,w} - 1$. When the scale factor reaches that given value, the Universe reaches the maximum expansion (and the minimum density at the same time) and later it starts to collapse until it returns to the singolar point when $a = 0$. As

equation (1.20) is a quadratic, the decreasing solution is equal to the increasing one, hence the collapse is equal and opposite to the expansion. This scenario is called *Big Crunch* (Figure 1.1).

Therefore, we learnt that the curvature is not relevant for the past history, while it is fundamental to know the future.

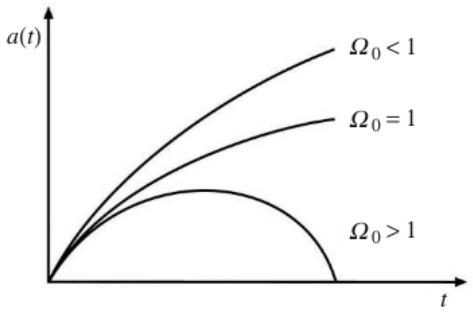

Figure 1.1: Density parameter as a function of time for the three geometries (Coles P. & Lucchin F., "Cosmology").

Density Parameter Evolution With Time

Starting from the definition of density parameter $\Omega_w \equiv \rho_w/\rho_{cr}$, we can write it using equation (1.12) and expanding the expression of the critical density ρ_{cr}:

$$\Omega_w^{-1}(z) - 1 = \frac{\Omega_{0,w^{-1}-1}}{(1+z)^{1+3w}}. \tag{1.25}$$

Note that $1 + 3w$ is always positive for radiation and matter. Moreover, if $z \to +\infty$ then $\Omega_w(z) \to 1$, in other words the very young Universe is flat in every case. When z$\to$ 0, the sign of Ω_w is uniquely given by the numerator in the right-hand term, and in particular by the value of Ω_0, which does not depend on w. This means that:

- if $\Omega_0 > 1$ then $\Omega(z)^{-1} - 1 < 0 \to \Omega(z) > 1$ always;
- if $\Omega_0 = 1$ then $\Omega(z)^{-1} - 1 = 0 \to \Omega(z) = 1$ always;
- if $\Omega_0 < 1$ then $\Omega(z)^{-1} - 1 > 0 \to \Omega(z) < 1$ always;

so the dynamical evolution of the Universe does not influence the geometry, whatever component is considered.

1.6 Cosmological Horizons

Horizon Radius

The horizon radius R_{hor} is defined as the radius of the region in causal connection with the observer. Its value is finite because the speed of light is finite, and intuitively one could state that $R_{hor} = tc$, but light travels on proper distances, so it becomes

$$R_{hor} = a(t) \int_0^{a(t)} \frac{c\, da'}{a(t)\dot{a}(t)},$$

but if $t \to 0$, then $a(t) \to 0$ and $R_{hor} \to \infty$. Using the second Friedmann equation (1.7) close to Big Bang (when the curvature is negligible) and the equation of an EdS Universe, we obtain the following:

$$R_{hor} = \frac{3(1+w)}{1+3w}ct = \begin{cases} 3ct & \text{matter} \\ 2ct & \text{radiation} \end{cases} \tag{1.26}$$

The horizon radius is a linear function of time and it is finite for any curvature. Ordinary physics is valid only inside R_{hor} and the thermical equilibrium is not possible between two regions that are not causally connected.

Hubble Sphere Radius

It is the distance of an object that travels with speed c in a reference system integral with the expansion of the Universe, so

$$R_h = \frac{c}{H} = \frac{3(1+w)}{2}ct.$$

The dependences are the same of R_{hor}, but the physical meaning is quite different: R_h is an istantaneous measurement, while R_{hor} includes information about the past, so if two regions are causally connected, they will be forever. If something happened in the history of the Universe that inverted the trend of $\dot{a}$, R_{hor} would conserve that information of the maximum value reached by the scale factor, whereas R_h would not.

1.7 Models With Cosmological Constant

We now insert Λ in the Fredmann equations and, at the same time, we ignore $\Omega_{0,R}$, as the radiation dominates only in the very early history of the Universe, therefore the density of the Universe assumes the form $\tilde{\rho} = \rho + \Lambda c^2/(8\pi G)$ and, consequently, the pression becomes $\tilde{P} = P - \Lambda c^4/(8\pi G)$. We can write the first Friedmann equation as:

$$\ddot{a} = -\frac{4\pi G}{3}a\rho_M + \frac{\Lambda c^2}{3}a, \tag{1.27}$$

and the second one

$$\dot{a}^2 + Kc^2 = -\frac{4\pi G}{3}\left(\tilde{\rho} + \frac{3\tilde{P}}{c^2}\right)a = \left[\frac{8\pi G}{3}\rho_M + \frac{\Lambda c^2}{3}\right]a^2. \tag{1.28}$$

From the equation (1.27) we note that for some values of Λ we could have $\ddot{a} > 0$, and from the equation (1.28) it is clear that the term $\frac{\Lambda c^2}{3}a^2$ enhances the expansion velocity. If we define $\Omega_{0,\Lambda} \equiv \rho_{0,\Lambda}/\rho_{0,cr}$ and we rewrite the equation (1.28), we obtain a relation similar to equation (1.17), which is useful to determine how Λ influences the curvature of the Universe:

$$H_0^2(1 - \Omega_{0,M} - \Omega_{0,\Lambda}) = -\frac{Kc^2}{a_0^2}. \tag{1.29}$$

Thus Λ plays a crucial role in determining the curvature, so $K = 0$ does not mean $\Omega_{0,M} = 1$ anymore, but $\Omega_{0,M} + \Omega_{0,\Lambda} = 1$. Therefore, it is possible to have a flat

Universe with $\Omega_{0,M} < 1$ and $\Omega_{0,\Lambda}$ which balances the value. From equations (1.27) and (1.28) we can define the deceleration parameter with Λ as

$$q = \frac{4\pi G}{3H^2}\rho_M - \frac{\Lambda c^2}{3H^2} = \frac{1}{2}\Omega_M - \Omega_\Lambda. \tag{1.30}$$

The equation (1.30) demonstrates that Λ is necessary to have an accelerated expansion of the Universe, and that the condition for this acceleration is $\Omega_\Lambda > \frac{1}{2}\Omega_M$. By means of measurements of SNIa, q_0 has been estimated as -0.6, in fact SNIa are standard candles since they have the same absolute magnitude M at the moment of the explosion and from the distance module, defined as

$$m - M = 25 + 5\log(cz) - 5\log H_0 + 1.086z(1 - q_0),$$

knowing the redshift z and measuring the apparent magnitude m, we can estimate q_0.

1.8 Energetic Balance Of The universe

We now draw a picture of what we know about the energetic contribute of the various components of the Universe.

- $\Omega_{0,R} \approx 10^{-5}$ is the contribute we know best, estimated from observation of the Cosmic Microwave Background radiation (CMB), which is an almost perfect black body with temperature equal to 2.726 K;
- $\Omega_{0,M} \approx 0.3$, which includes baryonic matter and dark matter, estimated by means of dynamical events or gravitational lensing. The constribute of the baryonic matter alone is $\Omega_{0,b} \approx 0.04$, given by the acoustic peak analysis of the CMB;
- $\Omega_{TOT} = \Omega_{0,R} + \Omega_{0,M} + \Omega_{0,\Lambda} \approx 1$ estimated by observations of the CMB radiation, in particular by the position of the first acoustic peak of the angulat spectrum of the CMB;
- $\Omega_{0,\Lambda} \approx 0.7$ derived by subtraction from the value of Ω_0 or by the equation (1.30).

We conclude that we live in a flat Universe and that the radiative contribute is nowadays negligible, but it was not in the first epoch of the history of the Universe. Moreover, we are in a trantitional phase, from the matter domain to the dark energy domain, as the respective contributes state. Thus, the Universe is in a inflection point where the function $a(t)$ passes from $\ddot{a} < 0$ to $\ddot{a} > 0$, hence to an accelerated expansion. If we set $q(z) = \dfrac{\Omega_M(z_{infl})}{2} - \Omega_\Lambda(z_{infl}) = 0$, this is the condition to find the precise moment of the change of curvature and it is satisfied for $z_{flesso} \approx 0.8$. The fact that the inflection is so close to z_0 seems a too big coincidence to many; in fact, this is known as the *coincidence problem* of the big Bang theory.

1.9 Relevant Moments Of The Thermical History Of The Universe

So far we treated the Universe as an adiabatic system, and we made use of the adiabatic condition. An adiabatic expanding system inevitably cools, so the history of the

Universe, from the Big Bang to now, is basically the history of a cooling. From the Big Bang, when ideally $T, \rho \to \infty$ and $R_{hor} \to 0$, the expansion process have enhanced R_{hor}, so the Universe content dilutes, and T and ρ have decreased.

We define the *Planck epoch* as the time range after the Big Bang in which we must consider quantum mechanics. The Planck time comes from the Uncertainty Principle $\Delta E \Delta t \approx \hbar$, with thecrelativistic energy $\Delta E = m_p c^2$ and $\Delta t = t_p$, where t_p is the time scale of perturbations $l_p = t_p c$, which have mass $m_p = \rho_p l_p^3$ with $\rho_p = 1/\sqrt{G t_p^2}$, so that

$$t_p = \sqrt{\frac{\hbar G}{c^5}} \approx 10^{-43} s.$$

From now to t_p after the Big Bang the relativistic theory is valid, while for $t < t_p$ a quantum thoery of gravitation is needed. Since no quantum theory of gravitation has been confirmed so far, we usually let start the Universe history from t_p.

Let's see, very briefly, the most important moments in the history of this cooling process, neglecting for the moment Λ and focussing on the relation between matter and radiation. Baryonic matter and radiation can be either coupled or decoupled, depending on whether they are in thermal equilibrium, that means $T_R = T_{M,b}$, which is satisfied if the time scale of collions among matter and radiative particles $\tau_{coll} = m_p/(c\sigma\rho_M)$ is shorter than the time scale of the expansion of the Universe $\tau_h = 1/H$. Nowadays baryons and radiation are decoupled, because $\tau_{coll} \gg \tau_h$ and the relative temperatures have different trends with time, which can be recovered from the adiabaticity condition:

$$\begin{cases} T_R \propto a^{-1} \\ T_{M,b} \propto a^{-2} \end{cases} .$$

From the definitions of temporal scales τ_{coll} and τ_h, it is clear that they have different dependences on time. This means that a *time of decoupling* z_{dec} between matter and radiation exists, at which $\tau_{coll} = \tau_h$ was satisfied, and for $z > z_{dec} \to \tau_{coll} < \tau_h$ matter and radiation were decoupled. From the equivalence $\tau_{coll} = \tau_h$, using the EdS equations, we obtain that $z_{dec} \approx 10^3$. Hence, for $z > z_{dec}$ baryons and radiation interact with an enough high rate to be considered as one component with temperature $T_{R+M,b}$, as it is shown in Figure 1.2.

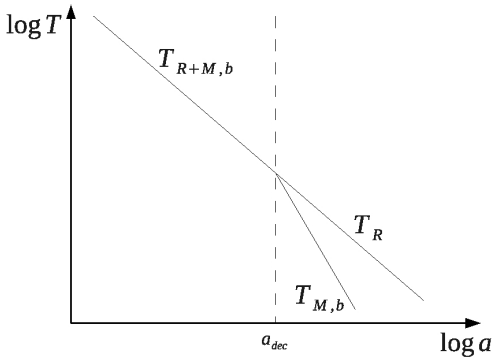

Figure 1.2: Temperature trends with the expansion parameter before and after the decoupling between matter and radiation.

Another important moment is the *equivalence time*, that is the transition between the radiative domination and matter domination, happened at z_{eq} satisfying $\rho_M(z_{eq}) = \rho_R(z_{eq})$. Assuming, for example, $\Omega_{0,M} = 0.25$ and $h = 0.7$, we obtain $z_{eq} \approx 5 \times 10^3$. Hence, we have to consider both components only close to z_{eq}, while for $z > z_{eq} \to w = 1/3$ and $z < z_{eq} \to w = 0$.

As the temperature decreses with time from the Big Bang, at a given time T drops the hydrogen ionization temperature $T \approx 4 - 5 \times 10^3$ K, so athoms start to combine.

This time is called *recombination time*,about at $z_{rec} \approx 1500$, and after the Universe becomes neutral.

The application of the EdS equations, without considering Λ, is consistent because the curvature becomes relevant only at $z \approx 10-20$ and the contribute of Λ is significant only at $z \approx 1$. We can conclude that in the first moments of its history, the Universe is fille with ionized plasma composed by matter and radiation in thermal equilibrium (see Figure 1.3). At $z_{eq} \approx 5000$ matter starts to dominate. As the temperature decreases, at $z_{rec} \approx 1500$ protons and electrons in the plasma begin to combine. Due to the

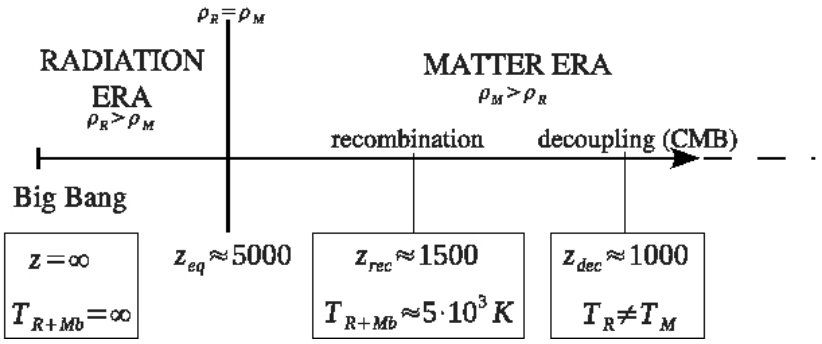

Figure 1.3: Schematic portrayal of the important moment in the history of the Universe, from the Big Bang to the decoupling.

recombination of athoms, radiation and matter interact less and less, until the moment of decoupling, at $z_{dec} \approx 1000$, is reached. From the Big Bang to this moment, photons have been continuously deflected by interactions with protons and electrons, so they lost the memory of the information they brought; from the decoupling, photons have been free to travel through space-time without being scattered by interactions with matter, so they could bring us the first signal we can see of the Universe, the CMB radiation. This sequence of events, and the difference between z_{eq} and z_{dec}, is very important to understand the hierarchical model, on which the dynamics of the structure formation is based.

1.10 Problems Of The Big Bang Theory And The Inflationary Model

The main successes of the Big Bang theory are: I principali successi del modello del Big Bang sono:

1. the primordial nucleusynthesis, largely explained by the model;
2. the origin of cosmic structure from the growth of mall matter density fluctuations for gravity;
3. the expansion of the Universe.

On the other hand, if we assume the "new physics"[3], the Big Bang theory takes various problems:

[3]The "new physics" is the totality of the force unification theories: the QED (Quantum Electro-Dynamics) and the GUT (Great Unification Theory).

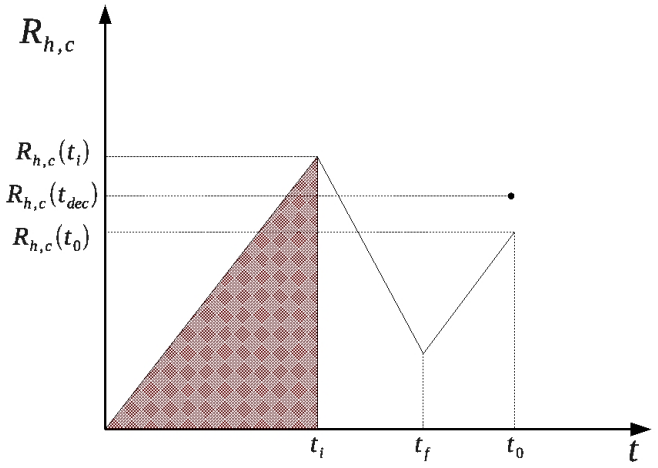

Figure 1.4: Schamatic visualisation of the inflationary period: t_i marks the beginning of the inflation period, t_f the end and t_0 today; $R_{h,c}$ is the comoving horizon radius, so $R_{h,c}(t_{dec})$ is the comoving horizon radius at the time of decoupling. The shaded region represents the scale causally connected at time t_i. Scales among $R_{h,c}(t_0)$ and $R_{h,c}(t_i)$, although in causally equilibrium, are larger than the horizon radius today.

Di contro, se si assume come buona la "new physics"[4], il Big Bang porta con sè i seguenti diversi problemi:

1. the origin of the Universe at $t = 0$;

2. the flatness problem: from equation 1.25 comes that a very small variation of $\Omega(t_p)$ determines a huge difference in the value of Ω_0. Hence, a *fine tuning* problem arises, in other words only with a very precise regolation of parameters we can obtain $\Omega_0 \approx 1$, as recents measurements confirm;

3. the horizon problem: the radius that encloses the CMB radiation, event though the latter is in thermal equilibrium, is larger than the cosmological horizon at that epoch;

4. what happens close to the Big Bang, at high energies, namely $T > 10^{19}$ GeV: with the new physics we can explain the phenomenons occurred at that temperatures;

5. the homogeneous and isotropic distribution on large scale;

6. the prediction of the existence of magnetic monopoles, but never detected.

The cosmic inflation solves the problems 3, 5 and 6, but it introduces Λ, so the open problems to date are the cosmic origin at $t = 0$ and the cosmological constant Λ.

Cosmic Inflation

The cosmic inflation model considers a period in the history of the Universe throughout which $\ddot{a}$, from being negative, becomes positive, with a consequent change of the sign of $\dot{R}_{hor,c}$, where c means comoving. As Figure 1.4 shows, this is the only way to observe today two regions in thermal equilibrium though lieing outside the cosmic horizon. In order to have the results we can observe, the inflation must last a precise time, expressed by the e-folding number $N_{eF} \equiv \ln \frac{a_f}{a_i} \gg 60$, where a_i and a_f are the scale factors at the beginning and at the end of the inflation period, respectively. The particle that mediates the scalar field which caused the pricordial acceleration is known with the general name of *inflaton*, and it is characterised by an enough high energy to allow a large e-folding number. Energies which satisfy this request are possible only in the radiation dominated era, and people uses to place the inflation period during the GUT phase transition.

Lots of inflation models exists, but here none of those will be studied in details, since this work does not concern that issue. Anyway, all inflation models end with an equation of state relative to matter, but we said that inflation must be placed during the radiation era, because only in that period a so high energy particle can exist. Moreover, it is necessary that some process removed all inflation and filled the Universe of ordinary matter. This double result is given by the inflaton decay, a process that heats up the Universe until it reaches temperatures close to the GUT transition temperature. Quickly all inflations decay in scalar particles which fill the Universe. In this moment density perturbations, the seeds of cosmic structure formation, originate.

[4] La "new physics" è l'insieme delle teorie di unificazione delle forze: la QED (Quantum Electro-Dynamics) e la GUT (Great Unification Theory).

Chapter 2

Structure Formation

The inflationary period produces the density fluctuations which, from a certain moment, will grow for gravity leading to the formation of cosmic objects. To date, the most accredited cosmological model identifies Dark Matter (DM) and baryons as the two components of matter, which have very different behaviours and roles in the structure formation process. DM interacts only throught gravity, while baryons also through electromagnetism, so the growth of matter perturbations will follows different paths depending on the considered matter component. Very briefly, we have the following events:

- at $z \sim \infty$, at the end of inflationary period, matter perturbations originate;
- until $z > z_{eq} \approx 5 \times 10^3$ radiation dominates and its pressure inhibits the growth of perturbations (relatively to DM, this phenomenon is called *stagnation*, which will be illustred below);
- at $z_{dec} < z < z_{eq}$ the domination of matter starts, DM perturbations are free to grow, while baryons are still coupled with photons through electromagnetic interactions;
- at $z \approx z_{dec}$ baryonic matter and radiation decouple: photons of the CMB radiation take information about this moment. The CMB radiation shows the structure of the *last scattering surface* and it traces the small baryonic matter density fluctuations which are free to grow from this moment.

In this model, Dark Energy (DE) does not collapse and is considered as a background component to better define the mean density the expansion rate of the Universe. We defined $z_{rec} \approx 1500$ as the beginning of recombination of protons and electrons to form hydrogen atoms. Until this moment, electrons and photons contiuously interacts and makes the Universe opaque to any observation. From $z = z_{rec}$, the number of scatters among electrons and photons decreases until the moment of decoupling, at $z_{dec} \sim 1000$. From the probability density function of the last scattering we found that it reaches the maximum at $z \approx 1100 \equiv z_{ls}$, where ls stays for last scatterins.

Assuming adiabatic perturbations (hence $\rho_M \propto a^{-3}$) the fluctuations of temperature and matter density are related in this way

$$\delta \equiv \frac{\delta T}{T} \propto \frac{1}{3}\frac{\delta \rho}{\rho}(z_{ls}) \approx 10^{-5},$$

so at the beginning the growth of structure can be considered as linear. However, the observed cosmic objects are characterised by a density contrast $\delta \approx 10^2$, in highly non-linear regime, which can be faced onyl through numerical techniques.

2.1 The Linear Theory

In order to deal with the intial linear growth of structure, when $\delta \ll 1$, we must define some spatial and temporal fundamental scales.

The Jeans Scale

Let's conside the Universe as a static fluid embedded in a gravitational field, thus we can consider the fluid dynamics equations

$$\begin{cases} \dfrac{\partial \rho}{\partial t} + \vec{\nabla}(\rho \vec{v}) = 0 & \text{continuity} \\ \dfrac{\partial \vec{v}}{\partial t} + (\vec{v} \times \vec{\nabla})\vec{v} = -\dfrac{1}{\rho}\vec{\nabla}P - \vec{\nabla}\Phi & \text{Euler} \\ \nabla^2 \Phi = 4\pi G \rho & \text{Poisson} \end{cases} \tag{2.1}$$

and we can insert on them a solution perturbed by small and adiabatic fluctuations ($dS/dT = 0$, where S is entropy, thus the equation of state has the form $P = P(\rho)$)

$$\begin{cases} \rho = \rho_b = \text{const} & \to \rho = \rho_b + \delta\rho \\ P = P_b = \text{const} & \to P = P_b + \delta P \\ \vec{v} = 0 & \vec{v} = \delta\vec{v} \\ \Phi = \Phi_b = \text{const} & \to \Phi = \Phi_b + \delta\Phi \end{cases} \tag{2.2}$$

where the subscript b means *background*, and $\delta\rho$, $\delta\vec{v}$, and $\delta\Phi$ are the density, velocity and potential perturbations, respectively. We assume that the perturbation is a solution of the system and we linearize it, coming to the fliud dynamic equations for perturbations in a static Universe:

$$\begin{cases} \dfrac{\partial \delta\rho}{\partial t} + \rho_b \vec{\nabla}\delta\vec{v} = 0 \\ \dfrac{\partial \delta\vec{v}}{\partial t} = -\dfrac{v_s^2}{\rho_b}\vec{\nabla}\delta\rho - \vec{\nabla}\delta\Phi \\ \nabla^2\delta\Phi = 4\pi G \delta\rho\rho_b \end{cases} \tag{2.3}$$

where v_s, which satisfies $\delta P = v_s^2 \delta\rho$ is the sound velocity under adiabatic condition. Since differential operators are much easier to deal with in the Fourier space, we assume that solutions are plane waves and we move to the Fourier space. Thus, perturbations become

$$\begin{cases} \delta\rho(\vec{r}, t) = \delta\rho_k \exp(i\vec{k} \times \vec{r} + i\vec{\omega}t) \\ \delta\vec{v}(\vec{r}, t) = \delta v_k \exp(i\vec{k} \times \vec{r} + i\vec{\omega}t) \\ \delta\Phi(\vec{r}, t) = \delta\Phi_k \exp(i\vec{k} \times \vec{r} + i\vec{\omega}t) \end{cases} \tag{2.4}$$

with $\vec{\omega}$ being the wave pulsation and $\vec{k} = 2\pi/\vec{\lambda}$ is the inverse of the lenght scale. Equations (2.3) therefore become $\left(\frac{\delta\rho_k}{\rho_b} \equiv \delta_k\right)$

$$\begin{cases} \vec{\omega}\delta_k + \vec{k}\delta\vec{v}_k = 0 \\ \vec{\omega}\delta\vec{v}_k = -\vec{k}(v_s^2\delta_k - \delta\Phi_k). \\ \delta\Phi_k = -\dfrac{4\pi G\rho_b}{k^2}\delta_k \end{cases} \tag{2.5}$$

We finally have a system of three linear equations with three variables, which can be solved using the role of the determinant, through which we obtain the *dispersion relation*:

$$\omega^2 = v_s^2k^2 - 4\pi G\rho_b \tag{2.6}$$

which relates the fundamental quantities $\vec{\omega}$, $\vec{k}$, $\vec{v}_s$ and ρ_b.

The pulsation $\vec{\omega}$ governs the waves dependence on time, as expresses by equations (2.4); from equation (2.6) we note that ω^2 can by positive or negative, so $\vec{\omega}$ may be either imaginary or real, if $\omega^2 < 0$ or $\omega^2 > 0$, respectively. In the first case, the dependence on time is real, so the amplitude changes with time and there is not free propagation. In the second case, the dependence on time is imaginary, thus the wave propagates with constatn amplitude. These two regimes are divided by the condition $\omega^2 = 0$ and, from equation (2.6) and from the definition of $\vec{k}$, we obtain a lenght scale known as the *Jeans scale*:

$$\lambda_J = v_s\sqrt{\frac{\pi}{G\rho_b}} \tag{2.7}$$

which marks the limit over which a wave changes its amplitude with time; to the Jeans lenght, the *Jeans mass* is connected:

$$M_J = \frac{4}{3}\pi\rho_b\lambda_J^3. \tag{2.8}$$

Let's see the two cases in detail:

1. $\lambda < \lambda_J$: small waves w.r.t. the Jeans scale, $\omega^2 > 0$ thus the pulsation is real and solutions are formed by a couple of sonic waves with amplitude $\delta\rho_k$, which propagates in time with constant phase velocity;

2. $\lambda > \lambda_J$: waves with amplitude greater than the Jeans scale, $\omega^2 < 0$ thush the pulsation is imaginaru and solutions are given by $\delta\rho(\vec{r}, t) = \delta\rho_k \exp(\pm\omega t)\exp(i\vec{k}\times\vec{r})$, one increasing (the one we are interested in) and the other one decreasing.

Horizon Scale

Another important scale is the horizon radius R_{hor}, already defined in 1.6, which divides the region causally connected, so where micrphysics is relevant, from the region where only gravity interactions are relevant. As outside the horizon radius there is not radiative pressure which balance the gravitational pull, perturbations on scales $R > R_{hor}(t)$ always grow, following the law

$$\delta(t) = \frac{3c^2}{8\pi Ga^2\rho_b}, \tag{2.9}$$

obtained considering the fluctuation as a closed Universe embedded in a background EdS Universe and using Friedmann equations. The dependence of $\delta(t)$ on ρ_b tells that

the temporal trend depends on the dominant componente (see equation 1.12), so we can divide the two hypotesis:

- if $t < t_{eq} \rightarrow \rho_b \propto a^{-4}$ thus $\delta_R \propto a^2$;
- if $t > t_{eq} \rightarrow \rho_b \propto a^{-3}$ thus $\delta_M \propto a$.

The other components follow the same dependences of the dominant one, since outside the horizon all of them interact only through gravity.

Evolution Of Perturbations In A Flat Expanding Universe

We analyse now the case of scales smaller than the horizon, recovering the solutions with an approach analogous to that one we used in the previous section for a static Universe.

We perturbate the fluid statics equations considering the expansion by means of the Hubble law, which defins the background velocity $\vec{u}$:

$$\begin{cases} \rho = \rho_b & \rightarrow \rho = \rho_b + \delta\rho \\ P = P_b & \rightarrow P = P_b + \delta P \\ \vec{u} = H\vec{r} & \rightarrow \vec{u} = H\vec{r} + \vec{v}. \\ \Phi = \Phi_b & \rightarrow \Phi = \Phi_b + \delta\Phi \end{cases} \tag{2.10}$$

In an flat radiation dominated Universe, thus for times $t < t_{eq}$, the perturbed and linearized system leads to the following equation which regulates the evolutions of fluctuations:

$$\ddot{\delta}_k + 2\frac{\dot{a}}{a}\dot{\delta}_k + \left(k^2 v_s^2 - \frac{32}{3}\pi G\rho_b\right)\delta_k = 0 \tag{2.11}$$

where the term $2\dfrac{\dot{a}}{a} = 2H$ is called *Hubble friction*, that slows down the growth of perturbations. By means of the dispersion relation we find that before the equivalence

$$\lambda_J(t) > R_{hor}(t),$$

that it inside the horizon there is no gravitational instability, since the sound velocity is very close to c and the pressure is strong enough to erase the matter density fluctuations.

After the equivalence, so when $t > t_{eq}$, the equation that regulates the evolution of perturbations in a matter dominated Universe is almost equivalent to equation (2.11):

$$\ddot{\delta}_k + 2\frac{\dot{a}}{a}\dot{\delta}_k + \left(K^2 v_s^2 - 4\pi G\rho_b\right)\delta_k = 0, \tag{2.12}$$

there is only a different numerical factor because of the negligible contribute of matter pressure to gravity w.r.t. the radiative pressure. The Jeans scale we obtain in this case, solving equation (2.12) is

$$\lambda_J = \frac{v_s}{5}\sqrt{\frac{6}{\pi G\rho_b}}, \tag{2.13}$$

that, like in the static case, separates the lenght scale into two regimes, so that perturbation on scales $\lambda < \lambda_J$ propagates as acoustic waves with constant amplitude, while for perturbations on scales $\lambda > \lambda_J$ two solutions exist, one increasing and the other one decreasing. The scale λ_J is valid for both baryons and DM. The term v_s, which presumes the existence of a fluid, is nonsense when dealing with DM, as it is non-collisional, but the velocity dispersion of particles is used instead, which has the same meaning of the sound velocity in a collisional fluid.

Evolution Of Perturbations In A Matter Warped Universe

Let's see now how matter perturbation evolve at times $t < t_{eq}$, on scales $\lambda_J < \lambda < R_{hor}$. We use the similarity between equation (2.12) with the equation that describes the evolution of the hubble parameter H in case of negligible pressure:

$$\ddot{H} + 2H\dot{H} - 4\pi G\rho_b = 0, \tag{2.14}$$

which means that the two equations have the same solutions. In Friedmann models, $H(t)$ is an increasing monotonic function, thus relates to the decreasing solution $\delta_-(t)$. In order to obtain $\delta_+(z)$, we use the relation between increasing and decreasing solutions defined by the wronskian $W = \delta_-\dot{\delta_+} - \delta_+\dot{\delta_-}$, and we can recover

$$\delta_+(z) = H(z)\int \mathrm{d}z \frac{\mathrm{d}t}{(\mathrm{d}z)}\frac{1}{(aH)^2}. \tag{2.15}$$

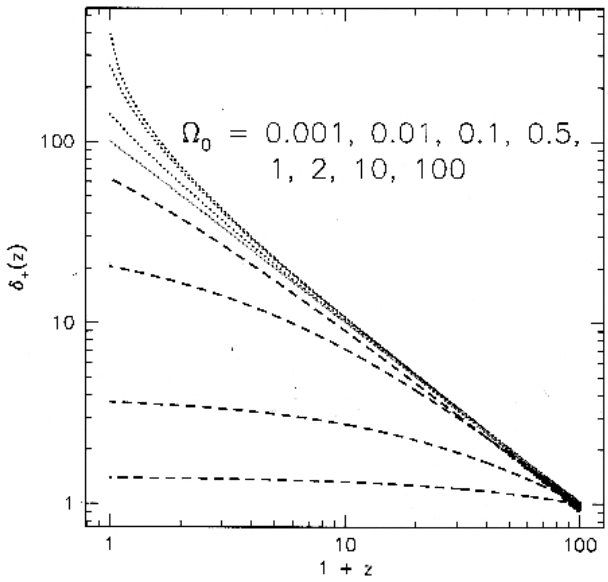

Figure 2.1: The growth of perturbations in function of redshift. Solid, dashed and dottet lines depict flat, open and close Universes, respectively. The relative values of Ω_0 are labeled on the plot.

The dependence on $H(z)$ makes the growth factor very sensitive to the cosmic geometry and to the expansion rate. In open Universes perturbations grow less, since the Hubble friction is stronger, while in closed Universe the expansion rate is less important, hence the growth is much more significative.

Dissipation Scales

Since the fluid we are considering is not perfect, some dissipative phenomenons may occur on small scales. From the time of decoupling from the plasma of baryons and photons, the fluctuations of DM freely propagate following geodetics fixed by the global, not local, gravitational field of perturbation, so they fill the underdense regions and flatten the overdense ones. This phenomenon is called *free streaming*, and it is associated

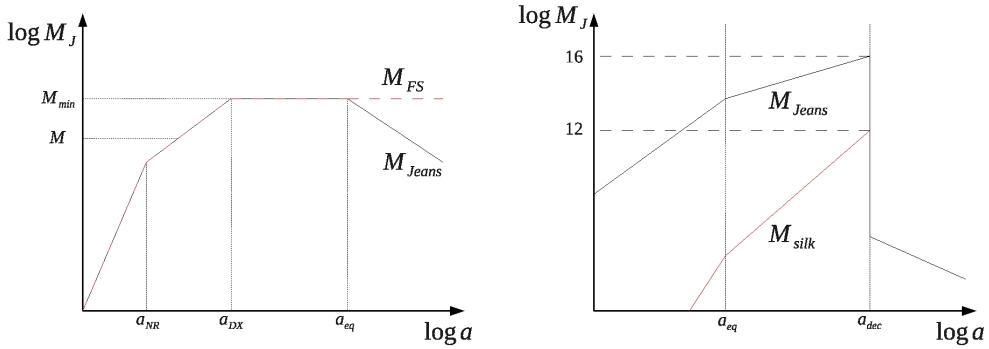

Figure 2.2: *Left panel*: Jeans and free streaming masses (in black and dashed red, respectively) trends with time for Cold Dark Matter (CDM); NR and DX stands for "de-relativization" and "decoupling" of particle X, DM candidate. In Section 2.2 those two moments will be described in details. *Right panel*: Jeans ans Silk masses (black and red line, respectively) trends with time for baryonic matter.

with the free streaming mass, which defines the dissipation scale. Free streaming mass and Jeans mass have the same trend (Figure 2.2, left-panel), because they are based on the same physics: the Jeans mass is the scale under which the pressure inhibits the collapse, while the free streaming mass represents the scale of the oscillating phenomenons that soften it. In Figure 2.2, M_{min} is the minimum mass of a perturbation that grows without undergoing free streaming; we will see in Section 2.2 that its value depends on the characteristics of the candidate DM particles. Perturbations less massive than M_{min} are deleted.

Baryonic matter undergo a dissipative phenomenon, actually very similar to the free streaming: photons and baryons are coupled by continuous Thomson collisions, nonetheless photons have a mean free path with respect to baryons, which tends to flatten existing perturbations. Although the mean free path of photons is short, on average there is a significative effect. The scale under which photons delete the baryonic perturbations is called *Silk scale*, which is associated with the Silk mass. Contrary to DM, the Silk mass has not the same trend of the Jeans mass (Figure 2.2, right-hand panel), but at fixed a it is lower, thus some perturbations oscillate until z_{dec}, when they start again to collapse. Baryonic perturbations with $M > 10^{16} h^{-1} M_\odot$ always grow, while those ones with $10^{12} < M < 10^{16} h^{-1} M_\odot$ collapse as long as $M > M_J$, then they oscillate until they restart to grow at a_{dec}. Perturbations with $M < 10^{12} h^{-1} M_\odot$ grow, then oscillate when $M < M_J$, and finally, when the Silk scale exceeds their scale, are erased.

Summary Of Solutions

- $t < t_{eq}$
  - perturbations of scale $\lambda > R_{hor}$ always grow, radiation fixes the grow rate for all other components $\delta_R \propto \delta_{bar} \propto \delta_{DM} \propto a^2$;
  - perturbations of scale $\lambda < R_{hor}$ do not grow, since $\lambda_J > R_{hor}$, hence also baryonic perturbations do not grow, because they are coupled with radiation.

DM is not coupled, so DM fluctuations can grow, but they undergo stagnation: Hubble friction inhibits the perturbation collapse, so $\frac{\delta_{DM}(t_{eq})}{\delta_{DM}(t_{hor})} \leq \frac{5}{2}$ if the entrance of the perturbation is at $a_{hor} = 0$[1].

- $t_{eq} < t < t_{dec}$
  - at scales $\lambda > R_{hor}$ the rate of growth of perturbations is determined by matter, which dominate, depending also on the geometry of the Universe;
  - at scales $\lambda_J < \lambda < R_{hor}$ DM perturbations grow, while baryonic fluctuations oscillate, as they are still coupled with radiation;
  - at scales $\lambda < \lambda_J$ DM perturbations are erased by free streaming; baryonic fluctuations that are smaller than the Silk lenght are deleted, while those one with size included in the range between the Silk scale and the Jeans lenght, oscillate;
- $t > t_{dec}$
  - at scales $\lambda > R_{hor}$ same as $t_{eq} < t < t_{dec}$;
  - at scales $\lambda_J < \lambda < R_{hor}$ DM fluctuations grow and perturbations of baryonic matter start to collapse. It is possible to express the baryonic perturbation growth in relation with the DM perturbation growth in this way $\delta_{bar}(a) = \delta_{DM}(1 - a_{dec}/a)$, for $a \gg a_{dec}$ we have $\delta_{bar} \propto \delta_{DM}$, so baryonic matter perturbations, once baryons and photons are decoupled, quickly grow in the potential wells created by the earlier DM collapse, reaching the same growth rate. This phenomenon is called *baryon catch up* and it explains the existence of collapsed strucutre[2]. Radiative perturbations oscillate.
  - at scales $\lambda < \lambda_J$ DM and baryonic perturbation oscilalte; the Jeans scale for baryons falls down after the decoupling, since radiative pressure does not give anymore its contribute to contrast the gravitational push.

2.2 Values Of The Jeans Scale

We saw that the Jeans lenght discriminates growing fluctuations from those one that propagate with constant amplitude. Consequently, we defined the Jeans mass as the mass of earlier collapsed objects, described by equation (2.8). The dependence of the Jeans mass on the sound velocity, through λ_J, plays a fundamental role on the determination of the values of the Jeans masses for the matter components. It is defined a_{nr} as the "de-relativization time"[3] relatively to one component, and it is placed at the equilibrium between thermial energy and mass-energy at rest, thus when $KT = m_X c^2$, with

[1] We define The time of entrance of a fluctuation in the horizon scale t_{hor}. Since the horizon scale increases with time, then also the scales of perturbations inside the horizon are increasing functions of time.

[2] From the CMB radiation we measure $\frac{\delta T}{T} = \frac{\delta \rho}{\rho} \approx 10^{-5}$ so, for a flat Universe at $z = 0$ we should have a mean perturbation contrast $\frac{\delta \rho}{\rho} = 10^{-5}(1 + z_{dec}) \approx 10^{-2}$, a too small value to explain the collapsed structures, highly non-linear which can be observed today.

[3] The time needed by a particle to cool until non-relativistic velocities.

K being the Boltzmann constant and m_X the rest mass of particle x. Two situations, which define the two kinds of DM, are distinguished:

1. $a_{nr} < a_{dec}$: at the decoupling time the DM particle is already non-relativistic → Cold Dark Matter (CDM);

2. $a_{nr} < a_{dec}$: at the decoupling time the DM particle is still relativistic → Hot Dark Matter (HDM);

The Jeams mass trends with time for HDM and CDM are strictly related to the value of the velocity dispersion, which is $c/\sqrt{3}$ for $a < a_{nr}$. Since the HDM becomes non-relativistic later than CDM, the maximum value of M_J at the equivalence is larger, on the order of $10^{15} - 10^{16} M_\odot$, while for CDM we have $10^5 - 10^6 M_\odot$. All values given here are computed assuming an EdS Universe. On the other hand, M_J for baryons reaches the maximum at the decoupling, namely $3 \times 10^{16} M_\odot$.

If the DM that triggered the structure formation were HDM, the first collapsed structures would be the largest ones, that is galaxy clusters, and smaller ones would be formed by fragmentation, in the so-called *top-down* scenario. If it were CDM instead, the oldes structure should be massive as a big globular cluster, and the larger structures sould have formed by merging of small ones. The latter is called *bottom-up* scenario, and it is the favourite, since oldest observed structures are the smalles ones, while more massive objects, like galaxy clusters, seems to have recently formed, some do not even appear virilized.

The scenario depicted by the baryonic behaviour is similar to the top-down scenario, and it is confirmed by observations, which show that more massive galaxies are the oldest ones. This is explaind assuming that the formation of baryonic structures follows a different physics w.r.t. Dark Matter.

2.3 Statistical Aspects Of Structure Formation

We consider the density perturbations $\delta \equiv \delta\rho/\rho$, stochastically generated at the end of the inflationary epoch. We try to describe in a statistical way this stochastic field, which can be defined in every point of the Universe $\vec{x}$, so $\delta = \delta(\vec{x})$. Which is the probability $p(\delta)$ that, in a point $\vec{x}$, δ assumes a given value? The ergodic principle says that the mean of different realisations of a stochastic field can be substituted by local means. This principle helps to study the statistical properties of the Universe, since have only one realization; furthermore, the principle becomes a theorem (known as the *fair sample theorem*) when the probability $p(\delta)$ is described by a Gaussian. The distribution of perturbations predicted by inflation is extremely close to a Gaussian, thus we expect that the perturbation field can be described by mean (that is 0) and variance.

During linear and non-linear regimes of density fluctuation growth, the distribution of perturbations changes in different ways: the linear evolution depends on time but doe not depende on the spatial scale, so $\delta_{fin} = \delta_{ini}\delta_+(t)$, with $\delta_+(t)$ known as *growth factor*, therefore the distribution remains Gaussian even if it changes shape; on the other hand, during the non-linear phase the field is deeply altered, becoming non Gaussian.

2.3.1 Power Spectrum And Variance

The *correlation function* is defined as

$$\xi(\vec{r}) \equiv < \delta(\vec{x})\delta(\vec{x}+\vec{r}) >, \tag{2.16}$$

and indicates how much the value of the density fluctuation δ in the point $\vec{x}$ is correlated with the value of the fluctuations $\vec{x}+\vec{r}$. Passing in the Fourier space through the Wiener-Khintchine theorem, the definition (2.16) becomes

$$\xi(\vec{r}) = \frac{1}{(2\pi)^6}\int d^3k \int d^3k' < \hat{\delta}(k)\hat{\delta}(k') > \exp(i\vec{k}\times(\vec{x}+\vec{r}))\exp(i\vec{k}'\vec{x}) = \frac{1}{(2\pi)^3}\int d^3k P(\vec{k})\exp(i\vec{k}\vec{r}) \tag{2.17}$$

where $P(\vec{k})$ is the *power spectrum*, which satisfies

$$< \hat{\delta}(k)\hat{\delta}(k') >= (2\pi)^3 P(\vec{k})\delta_D(\vec{k}+\vec{k}'). \tag{2.18}$$

The correlation function and the power spectrum represent the same concept, the former in the real space, while the latter in the space of configurations. The meaning of $P(k)$ is better understood if we consider the case $k' = -k$, since we have

$$P(k) \propto < \hat{\delta}(k)\hat{\delta}^*(k') > \propto < |\delta_k^2| >, \tag{2.19}$$

where a properties of Fourier trasfmors has been used, namely if δ is real, then $\hat{\delta}^*(k) = \hat{\delta}(-k)$. Therefore, the power spectrum is related to the mean quadratic amplitude of the perturbation in the space k, that is it indicates how much is relevant the contribute of fluctuations in scale k on the whole spectrum.

The intial power spectrum predicted by inflation is a Zel'dovich spectrum, that is $P_i(k) \propto k$. If we consider a perturbation of scale $k \gg k_{hor}$, where k_{hor} is the horizon scale at the equivalence, when the perturbation enters the horizon we have that $P_{enter}(k) \propto k^{-4}P_i(k) \propto k^{-3}$, due to stagnation; a perturbation with size $k \ll k_{hor}$ does not undergo stagnation, so its spectrum remains unchanged $P(k \ll k_{hor}) \propto k$. Therefore, the slope of the power spectrum invert at large value of k and the peak corresponds to the horizon scale at the moment of equivalence.

The power spectrum is also related to the variance σ^2 (cosmologists use σ), the fundamental parameter to characterise the Gaussian field δ. Using the *Perceval theorem* and applying isotropy, we derive the following definition of punctual variance:

$$\sigma^2 = \frac{1}{2\pi^2}\int P(k)k^2 dk, \tag{2.20}$$

which is useless from a practical point of view, thus the *mass variance* is introduced:

$$\sigma_M^2 \equiv < \left(\frac{\delta M}{\bar{M}}\right)^2 >=< \delta_M^2 > \tag{2.21}$$

where

$$\delta_M(\vec{x}) \equiv \delta(\vec{x}) * W(R),$$

that is a smoothed version of the field δ by means of the filter function W with size R, usually a Gaussian or a top-hat function; M is the mass included inside the filter of radius R. The convolution of the punctual field $\delta(\vec{x})$ with the filter $W(R)$ is still a Gaussian, since δ_M is a mean among volumes (see equation (2.21)). In the Fourier space, using the *convolution theorem*, the following expression for the mass variance is obtained:

$$\sigma_M^2 = \frac{1}{(2\pi)^3}\int d^3k P(k)\hat{W}^2(k,R). \tag{2.22}$$

2.4 Non-Linear Regime

The non-linear regime starts when $\delta \sim 1$ and it is reached firstly by small density perturbations of DM, as the hierarchical model states. The only efficient way to face the non-linear regime is by means of numerical simulations, which are illustrated in Section 3, but a solution for the case of spherical collapse exists, in which the perturbation is considered as a closed Universe embedded in a flat background Universe.

2.4.1 Mass Function From The Spherical Collapse Model

Considering the background Universe as an EdS Universe, the overdense region initially expands with rate minor than the expansion rate of the Universe, until it stops and it begin to collapse, followed by violent relaxation process that leads the overdensity to the virialization. During the collapse the density of the perturbation is about 180 times greater than the background density; baryons inside the perturbation lose energy, due to the dissipative processes, and they fall in the DM potential well. When the structure reaches the equilibrium, it will have a virial radius R_{vir}, which will enclose a region where the density is about $\delta\rho/\rho \approx 400$ times larger than the background density, independently on the considered scale.

The predicted value of $\delta\rho/\rho$ the final overdensity by the linear theory is 1.676. This number is related to the statistics of collapsed objects, since it tells us which is the value of a collapsed perturbation in the linear regime. Therefore, if we let evolve a matter distribution in linear regime, we can individiate a collapsed structure in every perturbation that reaches the critical value $\delta_c \equiv (\delta\rho/\rho)\,|_{lin} = 1.676$. Eke et al. (1996) computed virial overdensities of virialized haloes in flat ΛCDM Universes, with Ω_m spanning from 0 to 1, and found that, at the present time, the contrast of density of virialized object is $\rho_{vir}/\bar{\rho} = 324$ for $\Omega_m = 0.3$.

The mass function is a theoretical quantity that tells how many objects with mass M are inside a give cosmic volume V. There are two main approaches to recover it, the first one is through the analysis of the distribution of perturbations δ_M, while the second one is based on the Brownian analysis of trajectories in the ($s = \sigma_M^2$,δ) plane, following the so-called excursion set approach.

Considering the Gaussian distribution of δ_M, the probability that the latter had a given value can be expressed in the following way:

$$P(\delta_M)d\delta_M = \frac{1}{\sqrt{2\pi\sigma_M^2}} \exp\left(\frac{-\delta_M^2}{2\sigma_M^2}\right) d\delta_M, \tag{2.23}$$

but collapsing objects lie in the high density tail of the distribution of δ, and precisely they have $\delta > \delta_c$, where $\delta_c \equiv (\delta\rho/\rho)\,|_{lin} = 1.676$, as obtained by the linear theory of spherical collapse. Moreover, the field is filtered with radius R, which is related to the mass M, therefore the probability that $\delta > \delta_c$ is given by

$$P(\delta_M > \delta_c, R \to M) = \int_{\delta_c}^{\infty} P(\delta_M)d\delta_M = \frac{1}{2}\left[1 - erf\left(\frac{\delta_c}{\sqrt{2\sigma_M}}\right)\right] \tag{2.24}$$

with $erf(x) = \frac{2}{\sqrt{\pi}} \int_0^x e^{-t^2} \mathrm{d}t$ known as *error function*. Cosmology is crucial for the mass function, as it enters in σ_M, that depends on $\Omega_{0,M}$, $\Omega_{0,\Lambda}$, z, $P(k)$. The number of

collapsed objects can be recovered from

$$n(M)MdM = 2[P_{>\delta_c}(M) - P_{>\delta_c}(M + \Delta M)]\bar{\rho}_M = 2\bar{\rho}\left|\frac{\mathrm{d}}{d\sigma_M}P_{>\delta_c}\right|\left|\frac{d\sigma_M}{dM}\right|dM.$$

From the above expression, Press and Schechter found the following general way, good for any assumed power spectrum, to express the mass function:

$$n(M,z) = \sqrt{\frac{2}{\pi}}\frac{\delta_c}{\sigma_M(M,z)}\frac{\rho_M(z)}{M^2}\left|\frac{d\ln\sigma_M}{d\ln M}\right|\exp\left[-\frac{\delta_c^2}{2\sigma_M^2(M,z)}\right],$$

in which the cosmology enters through $\bar{\rho}_M = \Omega_M\rho_{crit}$ and σ_M^2. Assuming a power-law power spectrum, $P(k) \propto k^n$, we obtain the following form for the mass function

$$n(M) = \frac{2}{\pi}\frac{\rho_M \times \alpha}{M_*^2}\left(\frac{M}{M_*}\right)^{\alpha-2}\exp\left[-\left(\frac{M}{M_*}\right)^{2\alpha}\right], \tag{2.25}$$

with $\alpha = (n+3)/6$.

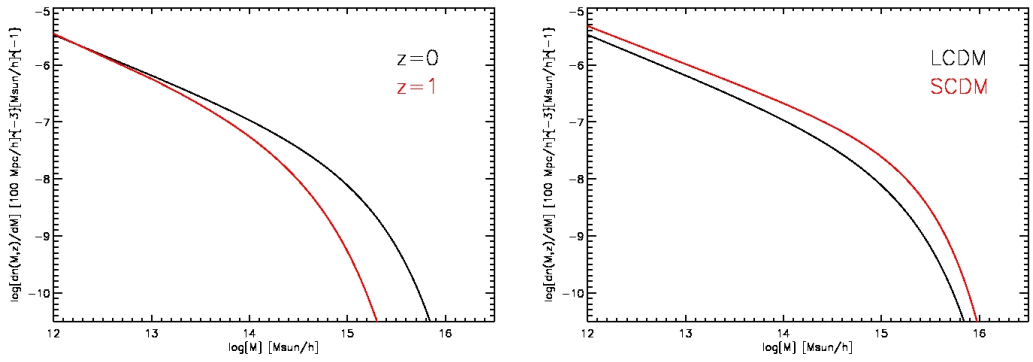

Figure 2.3: *Left-panel*: effect of redshift on the Press-Schechter mass function, for a ΛCDM cosmology ($\Omega_{0,M} = 0.3$, $\Omega_{\Lambda,0} = 0.7$); at higher z the cut-off shifts towards lower masses. *Right-panel*: effect of cosmology, fixed $z = 0$; red line traces the mass function for a SCDM model ($\Omega_{0,M} = 1$, $\Omega_{\Lambda,0} = 0$), while black line traces the ΛCDM. In both models $h_0 = 0.7$, $\sigma_8 = 0.9$ are taken and the considered volume is 100 $(\mathrm{Mpc/h})^{-3}$.

From equation (2.25) is clear that there are two different regimes of the mass function, divided by M_*: for $M \ll M_*$ the factor $M^{\alpha-2}$ domnates, while for $M \gg M_*$ the exponential cut-off dominates. As we can see in Figure 2.3, the position of the cut-off depends on z, since typical collapsed objects are more massive at low z, and on the cosmological model: fixed z, perturbations grow faster in an EdS Universe rather than in a ΛCDM model, thus the amplitude of the mass function in EdS model is larger than in ΛCDM model.

The mass function is not so sensitive to the shape of power spectrum, since $P(k) = Ak^nT^2(k)$ (with k^n defined by inflation, $T^2(k)$ by microphysics, A amplitude), and in the integral in equation (2.20) details of parameters dependent on k are lost. What is really relevant is the amplitude A, which get off the integral, but it is totally free in inflation models and it is not directly related to $P(k)$. For this reason we use

$$\sigma_R^2 = \frac{1}{2\pi^2}\int k^2Ak^nT^2(k)W^2(kR)dk \tag{2.26}$$

which, contrary to A, is an adimensional constant. Historically, σ_8 is used, that is $\sqrt{\sigma_R^2}$ with $R = 8$ h^{-1} Mpc .

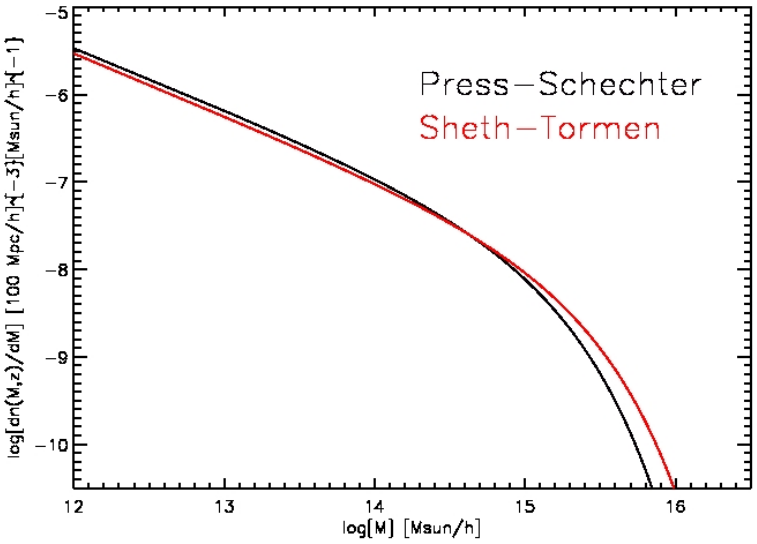

Figure 2.4: Comparison among Press-SChechter mass function (in black) and the Sheth-Tormen mass function (in red), at $z = 0$ in the ΛCDM model. The other parameters are defined as in Figure 2.3.

From the analysis of `GIF` N-body simulations in different cosmological models, Sheth & Tormen (1999) recovered a mass function which represents data better than the Press-Schetcher mass function. The main difference in the approach they adopted was to consider the ellipsoidal collapse of DM haloes rather than spherical. We will not enter in details of the ellipsoidal collapse, but we just show it since the Sheth-Tormen mass function has been used in this work. In Figure 2.4 both mass functions are shown, the Press-Schechter in black, the Sheth-Tormen in red. The difference between the two power-law regimes is negligible, but it becomes relevant at high masses: the number of collapsed objects with $M \gg M_*$ is greater than the number predicted by the Press-Schechter function, so it gives a better description of the population of galaxy clusters.

Excursion Set Approach

As we said, the fraction of smoothed density perturbations bigger than $\delta_c = \delta_c(z)$, on a scale R and at redshift z, gives the mass function of virialized haloes. This kind of approach proposes to re-formulate the Press & Schechter (1974) model using Brownian walks in the plane (s, δ) (Bond et al. 1991): trajectories that, starting from the origin, up-cross for the first time $\delta_c(z)$, at the abscissa s, correspond to virialized DM haloes of mass M. The mass fraction in virialized haloes will thus be defined by the trajectories that cross for the first time the critical overdensity $\delta_c(z)$, for fixed z (Bond et al. 1991).

The Brownian motion of a trajectory is mathematically described by the following diffusion equation:

$$\frac{\partial Q(s,\delta)}{\partial s} = \frac{1}{2}\frac{\partial^2 Q(s,\delta)}{\partial \delta^2} \tag{2.27}$$

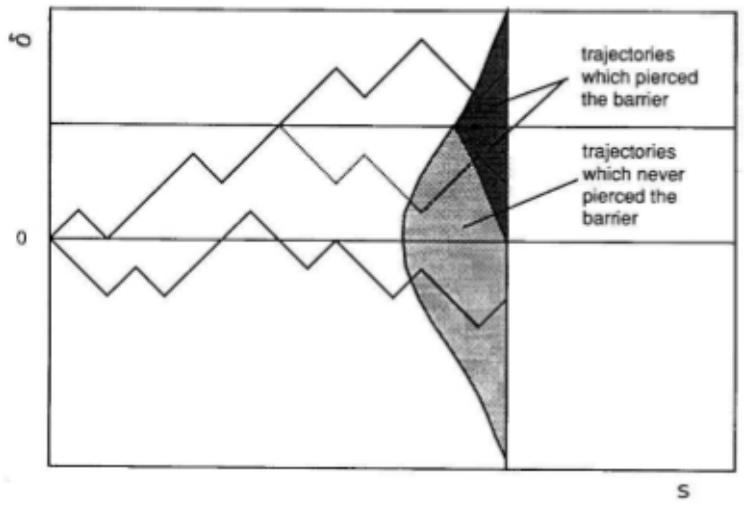

Figure 2.5: Random walks associated with the three probability (a), (b) and (c). See the main text for more details.

where $Q(s, \delta)$ represents the probability distribution that a trajectory in s has value δ. For Brownian walks, the solution of the diffusion equation, and so the distribution in S for walks that have $\delta = \delta_c$, is a Gaussian function, which has the form:

$$Q(s, \delta_c) = \frac{1}{\sqrt{2\pi s}} \exp\left(-\frac{\delta_c^2}{2s}\right). \tag{2.28}$$

Computing the mass function means counting, at a fixed redshift z, the fraction of trajectories that went over δ_c. It is necessary to remember that given the power spectrum, s does not correspond only to a mass M, but also to a scale k. Fixing the redshift z, in a given $\tilde{s}$ we could have three different kinds of trajectories:

- (a) those that have crossed δ_c and that are still over the barrier;
- (b) those that are under δ_c but have crossed the barrier at $s < \tilde{s}$;
- (c) those that have been always under the barrier.

As first step, let compute the fraction of trajectories that are still under the barrier, case (c): to all trajectories that are under the barrier we must subtract the (b)-kind ones. Considering that for a given (b)-kind walk there is another virtual trajectory that starting from $(0,\ 2\delta_c)$ intersects the barrier at the same point (see Figure 2.5, for a schematic representation of the three kinds of barriers), always satisfying the equation (2.27), the probability associated with (b)-kind walks is:

$$Q_b(\delta, s, \delta_c)\mathrm{d}\delta = \frac{1}{\sqrt{2\pi s}} \exp\left[-\frac{(\delta - 2\delta_c)^2}{2s}\right] \mathrm{d}\delta. \tag{2.29}$$

Hence, the probability for (c)-kind walks will be:

$$Q_c(\delta, s, \delta_c)\mathrm{d}\delta = \frac{1}{\sqrt{2\pi s}} \left\{\exp\left(\frac{\delta^2}{2s^2}\right) - \exp\left[\frac{(\delta - 2\delta_c)^2}{2s}\right]\right\} \mathrm{d}\delta.f \tag{2.30}$$

From equation (2.30) we can write the cumulative fraction of trajectories that never crossed the barrier δ_c as:

$$P_c(s, \delta_c) = \int_{-\infty}^{\delta_c} Q_c(\delta, s, \delta_c) \mathrm{d}\delta. \tag{2.31}$$

The complementary of this will represent the walks that intersected the barrier (that cosmologically represents the fraction of elements in collapsed objects with mass variance minor than s), that is

$$P_{a,b}(\delta, s) = 1 - P_c(s, \delta_c) = P(< s), \tag{2.32}$$

and the relative differential distribution:

$$p(s, \delta_c) = \frac{\partial P(< s)}{\partial s} = -\frac{\partial}{\partial s} \int_{-\infty}^{\delta_c} Q_c(\delta, s, \delta_c) \mathrm{d}\delta, \tag{2.33}$$

that, considering the diffusion equation (2.27) for (c)-kind trajectories, becomes

$$p(s, \delta_c) = -\frac{1}{2} \frac{\partial Q_c}{\partial \delta}\bigg|_{-\infty}^{\delta_c} = -\frac{\delta_c}{\sqrt{2\pi} s^{3/2}} \exp\left(-\frac{\delta_c^2}{2s}\right). \tag{2.34}$$

Using the rescaled variable $\nu = \delta_c^2/s$, equation (2.34) can be rewritten in the following way:

$$\nu f(\nu) = \sqrt{\frac{\nu}{2\pi}} \exp\left(-\frac{\nu}{2}\right) \tag{2.35}$$

that is the same equation recovered by Press & Schechter (1974) studying the formation of "self gravitating" masses and their evolution during the cosmic time in order to form galaxies and clusters of galaxies at the present time. The mass function can also be written in terms of m:

$$m^2 \frac{n(m, z)}{\bar{\rho}} = \nu f(\nu) \frac{\mathrm{d} \ln(\nu)}{\mathrm{d} \ln(m)}. \tag{2.36}$$

2.5 Galaxy Clusters

Galaxy clusters are the largest collapsed objects in the Universe, thus, following the hierarchical model, they are also the youngest. On average, the size of galaxy clusters is on the scale of Mpc, they contains from 100 to 1000 galaxies with average velocity $v_{gal} \sim 10^3$ km s^{-1}, and they have a virial mass of $M_{vir} = 10^{14} - 10^{15}$ $M_\odot$, assuming the virial equilibrium, which is composed of DM ($85 - 90\%$) and baryons ($10 - 15\%$), one third in form of galaxies and two thirds as hot intracluster gas. Gravitational tidal interaction between DM and baryons influences the spherical collapse of DM haloes, leading to triaxial virialized structures (Sheth & Tormen 1999).

The DM component formed through hierarchical aggregation of small haloes in more massive haloes. Baryons in haloes are compressed by shocks occurred during the formation process, thus they heat and completely ionize, forming a cloud of hot low-density intracluster gas (about $T = 10^7$ K and $n \approx 10^{-3}$ atoms cm^{-3}), trappend in the total potential well. This hot gas emits in X-ray for bremmstrahlung with luminosities reaching $L_X \approx 10^{45}$ erg s^{-1}, that makes galaxy clusters some of the most luminous X-ray sources in the Universe. The brayon fraction of the cluster mass remains in cold phase

in stellar systems, mostly old and red elliptical galaxies, therefore colour is one of the best instrument to recognize cluster galaxies. Usually, one or two giant galaxies occupy the central position, with masses about $10^{12} - 10^{13}\ M_{\odot}$, known as Central Dominant (CD) galaxies or Bright Central Galaxy (BCG). The most likely formation mechanism of those galaxues is galactic cannibalism: orbiting galaxies fall towards the central one due to dynamical friction.

The formation process of DM halo and CD galaxy suggest that galaxy clusters are plenty of substructures, which undergo an intense dynamical activity, as confirmed by numerical simulations; hence, observations of galaxy clusters are very useful to understand the interactions between DM and baryons. Substructures are the marks of the evolotions of DM haloes, as they are the nuclei of progenitor haloes, which formed the galaxy cluster by merging events.

The Navarro, Frenk & White Profile

The Navarro, Frenk & White (NFW) profile, recovered by N-body simulation analysis, reproduces the distribution of collapsed DM in haloes in virial equilibrium. The profile of haloes with mass in the range $[10^{11} - 10^{15}]\ M_{\odot}$is well described by the following law:

$$\rho(r) = \frac{4\rho_s}{\left(\frac{r}{r_s}\right)\left(1 + \frac{r}{r_s}\right)^2} \tag{2.37}$$

where r_s and ρ_s are the radius and density scales: if $r \gg r_s$ then $\rho(r) \propto 1/r^{-3}$, otherwise if $r \ll r_s$ then $\rho \propto 1/r$. Thanks to the normalisation scales, the profile expressed by the relation (2.37) is good for any DM halo, independently on mass, on the spectrum of intial fluctuations and on cosmological parameters. It differs from the isothermal sphere profile, namely $\rho(r) \propto 1/r^2$, for the fact that the NFW profile is steeper in outer regions and shallower in inner ones.

An useful parameter introduced by the NFW profile is the *concentration*, defined as $c \equiv r/r_s$ and linked to the halo mass, independently on cosmology. Since the time of collapse depends on the halo mass and, thus, small systems form earlier than massive ones (Sheth & Tormen 2004; Giocoli et al. 2007), the concentration parameter is related to the halo mass: at fixed z, small haloes have higher values of c with respect to massive haloes. Hence, the goemetry of the Universe plays an important role, as in open Universes the structure formation occurs more slowly than in closed ones, due to the Hubble friction; so, if we fix the formation redshift of an object, at a given z in an open Universe the concentration is smaller than what we would have in a closed Universe; vice-versa, fixed c, the formation time of a halo occurs early in an open Universe, since the collapse time si longer. Generally, for a given cosmology, haloes which formed at higher redshifts are more concentrated and contain less substructures than early formed haloes, because the assembly time is related to the concentration and the evolution time is related to the abundance of substructures. Thus, cosmology determines the trend of the mass-concentration relation with time for galaxy clusters; the relation we will use in this work has been recovered by Zhao et al. (2003) through N-body simulations analysis.

Chapter 3

N-Body Simulations

The non-linear evolution of structure is too much complex to be investigated by analytical approaches. The best way to do it is by means of cosmological N-body simulations. In numerical simulations, the mass distribution of the Universe is sampled by virtual particles which fill a cube of arbitrary comoving volume. The initially homogeneous distribution of particles is then perturbed and left evolve under the interaction with the Newtonian gravitational field in an expanding metric. Time in simulations flows in a non-continuous way and the history of cosmic structure is made up of a series of "photographs" of the simulated volume, called *snapshots*, for each of which the position and velocity of all particles are recorded.

In this chapter we will briefly describe the methods to perform Dark Matter N-body simulations, so we will ignore the methods used to simulate any interaction but the gravitational, and finally we will introduce the two numerical simulations we used and we will present the adopted post-processing method.

3.1 N-Body Methods

In few words, the idea behind Dark Matter numerical simulations is to compute the force that acts on each particle due to the presence of all the other ones, and, consequently, integrate the equations of motion to get the new position and velocity of particle. The time step is therefore updated. This simple idea hides a problem: the larger is the number of particles, the longer is the computational time to complete the process. Therefore, the main challenge of N-body methods is to reduce the computational time without losing information of particles. We will present the most common methods, each of them finding a compromise between precision and computational time.

PP: Particle-Particle

The Particle-Particle method is the simplest and the more precise method to perform numerical simulations. The force acting on the particle i is given by the sum of forces due to every particle j:

$$\vec{F}_i = \sum_{j \neq i}^{N} \frac{m_i m_j G}{(r_{ij} + \epsilon)^2} \vec{u}_{ij} \tag{3.1}$$

where r_{ij} is the distance between the two particles and ϵ is the *gravitational softening*, the minimum distance particles can get close, which avoid a diverging force when

distance between particles is close to zero. Subsequently, the motion equation are integrated to update positions and velocities for the next time step.

This method is the more precise but also the more demanding, as the required computational time is of the order of $O(N(N-1))$.

PM: Particle-Mesh

The idea of this method stays in approximating the particle distribution with a mass density grid (with arbitrary size) which is then used to compute the force field. Inside the cosmic volume, a mesh with M knots is defined. At every snapshot, to every grid point $x_{i,j,k}$ is then related the mass density $\rho(x_{i,j,k})$ given by the following:

$$\rho(x_{i,j,k}) = m_p M^3 \sum_{l}^{N} \Pi(\delta\vec{x}_l), \tag{3.2}$$

where $\delta\vec{x}_l$ is the distance of the particle l from the grid point $x_{i,j,k}$ and Π is an interpolation function. Therefore, from the Poissonian equation, the force is computed in every grid point and then in every particle by interpolation. Finally, positions and velocities are computed by integration of the equations of motion.

This method is very fast, as it presents a computational time of the order of $O(N + N_g \log(N_g))$ where N_g is the number of grid points. However, the resolution of the field undergoes a significant worsening, so this method is not suitable to study close encounters or highly non-uniform mass distributions. An usually adopted solution for the latter is the use of adaptive grids, in order to improve the resolution only in high density regions.

P3M: Particle-Particle/Particle-Mesh

This method joins the advantages of the two previously described methods: the force due to far particles is computed with the PM method, while the force due to close particles is computed by direct sum of PP method. In this way, the total force is divided into two parts: the slowly-varying long-range part and the rapidly-varying short-range part, the former at high and the latter at low resolutions. The threshold lenght among the two regimes is about 3 times the grid spacing.

If the separation among the two regimes is easy or there is no need of an optimal force resolution, the method is appropriate and the order of magnitude of computational time scales with $N+N_g$. The main disadvantage is that this method could be dominated by the direct summation part, especially in high density regions. Again, one possible solution is the use of spatially adaptive mesh.

TC: Tree-Code

The cosmic volume is divided in smaller and smaller cubes until in every cube is present at most one particle. In this way, a sort of tree, a hierarchical structure with the nodes being the cubes, is built. Starting from the largest cubes, the force is computed by walking the tree and summing up the contributes from tree nodes. If the cube is far enough (also depending on the force precision one wants to get) from the position where the force must be computed, the walk along that branch is termined. Thus, the force exerted by distant groups is approximated by their lowest multipole moments, while

name	box [Mpc h^{-1}]	z_i	$m_p[M_\odot h^{-1}]$	soft [kpc h^{-1}]	$N_{h>1000}$ $(z=0)$
GIF2	110	49	1.73×10^9	7	14928
Ada	62.5	124	1.94×10^7	1.5	36561
Bice	125	99	1.55×10^8	3	44883
Cloe	250	99	1.24×10^9	6	54467
Dora	500	99	9.92×10^9	12	58237
Emma	1000	99	7.94×10^{10}	24	38632
Flora	2000	99	6.35×10^{11}	48	5298

Table 3.1: Mean features of the simulations we consider. The last column is the number of haloes with more than 1000 particles identified at $z = 0$ by means of spherical overdensity criterion.

the force contribution of close particles is computed directly. This procedure is justified by the barycenter theorem: a system of distant particles can be considered as a single particle at the barycenter position, whose mass is the sum of all the particle masses.

The computational time of this method scales with $N \log N$. If the multipole expansion is carried out to higher orders (i.e. the trees are walked deeper), the force computation becomes more accurate.

3.2 Numerical simulations

In this section we describe the two cosmological numerical simulations (actually the second one is a set of 6 simulations) we analysed in this work. Both simulations follow only Dark Matter particles and are based on ΛCDM cosmological models. The main features of simulations are summarized in the Table 3.1.

3.2.1 GIF2

The GIF2 simulation (Gao et al. 2004) adopts a ΛCDM cosmology with the following parameters $\Omega_m = 0.3$, $\Omega_\Lambda = 0.7$, $\sigma_8 = 0.9$ and $h_0 = 0.7$. A periodic cube of side 110 Mpc h^{-1} is filled with 400^3 Dark Matter particles with individual mass $m_p = 1.73 \times 10^9\ M_\odot h^{-1}$. Initial conditions were produced by perturbing an initially uniform configuration represented by a glass distribution of particles. Based on the Zel'dovich approximation (Zel'Dovich 1970), a Gaussian random field is set up by perturbing the positions of particles and assigning velocities according to the growing model solution of linear theory. The critical value of the linear theory overdensity that is required for spherical collapse at the present time is $\delta_c = 1.676$. In order to reduce the computational time, the simulation was performed in two steps: until $z = 2.2$ with the parallel SHMEM version of HYDRA (Couchman et al. 1995) and then it has been completed with GADGET (Springel et al. 2001a), which has better performance on the heavily clustered regime (for more details on GIF2 simulation, see Gao et al. 2004).

3.2.2 LE SBARBINE

LE SBARBINE is a set of 6 cosmological simulations which were run in the Physics and Astrophysics department of the University of Padova in 2013-2014 (Despali et al. 2016), embedded in a ΛCDM cosmology with parameters $\Omega_m = 0.30711$, $\Omega_\Lambda = 0.69289$,

$\sigma_8 = 0.8288$ and $h_0 = 0.6777$, consistently with the recent results from Planck (Planck Collaboration et al. 2014).

All cubes were filled with 1028^3 particles and the boxes have increasing sizes, following the alphabetical order of names: from `Ada` to `Flora`, the box size doubles in every simulation, starting from 62.5 Mpc h^{-1} and reaching 2000 Mpch^{-1}. Since the number of particles remains always the same, increasing the box size makes the mass of particles increase from $1.94 \times 10^7\ M_\odot h^{-1}$ to $6.35 \times 10^{11}\ M_\odot h^{-1}$. In Table 3.1 the main characteristics of all simulations are listed. The whole new set includes about 250000 haloes identified at z_0 with more than 1000 particles; this number increases to about 22 millions if the mass threshold decreases to 10 particles.

The large range of mass covered by `LE SBARBINE` guarantees that haloes of all masses are formed by many particles, reducing the prolems due to resolution effects; moreover, since each mass range partially overlaps the two closest ones, one can isolate and check resolution effects.

3.3 Halo Finder Technique

Haloes in simulations are identified in every snapshot through the *spherical overdensity* (SO) criterion, applied by a code developed by Giuseppe Tormen. A local density $\rho_i \propto d_{i,10}^3$ is assigned to each particle i by calculating the distance to the tenth closest neighbour particles. Local densities are then sorted in deacreasing order and the position relative to the first one is taken as the center of the first halo. Then, a sphere around this point is grown until the mean density within it falls below the virial value appropriate for the cosmological model at that redshift. The radius of the resulting sphere is the virial radius R_{vir} of the halo. For the definition of virial density, the model of Eke et al. (1996) is taken. All particles inside the sphere are assigned to the halo and they are removed from the whole list. The center of the next halo is taken as the position of the particle relative to the following density in the sorted list and the process is repeated until all particles are scanned.

The minum number of particles a group must have inside the virial radius in order to be identified as a halo is 10. Particles that do not belong to any halo are identified as *field* particles.

3.4 Merger Trees

Before we start to describe our work, we introduce the elements that we are going to talk about. As we already said, cosmic structures come from mergers of Dark Matter haloes in a hierarchical way. If we take a halo, called the *host halo*, which has been identified at, let's say, $z = 0$ and we know the particles that are in it, we can trace back particles to the previous snapshot identifying all haloes which particles come from. We call *progenitors* all those haloes which contribute with at least 50% of their particles to the initial system. Tracing backwards the particles of all progenitors again and again until no more haloes are find, we finally get the *merger tree* relative to the intial halo identified at $z = 0$.

Among all progenitors, at each redshift we define the *main progenitor* (MP) as the halo that provides the largest mass contribute to the initially identified halo at z_0. Every progenitor which at any redshift directly merges with the MP, that is gives at

least 50% of its mass at the moment of merging, is called *satellite*. Linking all the MPs and satellites of a given halo means to follow the *main branch* of the halo.

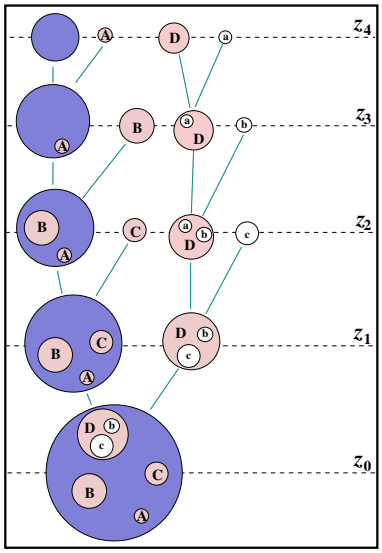

Figure 3.1: Schematic partial visualisation of a merger tree (taken from Giocoli et al. 2008).

In Fig. 3.1 a schematic view of a merger tree is shown. Blue haloes represent the main progenitors, which form the main branch, while the pink ones are satellites. In our investigation, we will not consider secondary branches, i.e. branches obtained following the merger history of a satellite. In Fig. 3.1, the branch identified by linking the main progenitors of satellite **D** represents a secondary branch of the merger tree of the blue halo. Moreover, satellites of satellites (haloes **a**, **b** and **c** in Fig. 3.1) are not considered.

When referring to satellites, all features taken at the redshift of merging will be meant as taken at the last snapshot in which the satellite is identified as a single halo. Hence, for example, the redshift of merging of satellites **A**, **B**, **C** and **D** are z_4, z_3, z_2 and z_1, respectively.

Chapter 4

Statistical Properties Of Dark Matter Haloes From N-Body Simulations LE SBARBINE

The clumpy nature of Dark Matter (DM) structure in the Universe is a well-established fact. Primordial fluctuations originated after the inflationary period in the DM mass distribution grow for the interaction with the general gravitational field. The collapse of such fluctuations into haloes has been investigated by several previous works. The gravitational field modifies consistently with the formation of haloes, thus they form bigger haloes by merging together, following a hierarchical way. We saw in the previous chapter that we can visualize this process as a merger tree. On average, a DM halo lives as an isolated halo until it falls inside a host and starts to orbit around its center of mass, as a satellite. This moment represents a crucial change in the evolution of the halo. While orbiting around the host center of mass, several dynamical effects may literally consume the halo even until its total destruction:

- tidal stripping: the tidal attraction of massive satellites can strip particles away;
- gravitational evaporation: close encounters may heat particles that form the satellite and give them kinetic energy. Particles which get enough kinetic energy can escape from the satellite potential well;
- dinamical friction: while orbiting into the dense host environment, the satellite catches a tail of particles from the host halo that acts as a brake for the satellite motion, so it loses angular momentum and falls towards the center of the host halo.

Two kinds of mass functions relative to subhaloes have been developed by studying numerical simulations, and they reflect these different evolutions they undergo as isolated haloes and as satellites. The first one, called *unevolved subhalo mass function*, models the number of satellites of given mass that entered in any host halo at any redshift. In other words, it expresses the average merger rate of haloes with satellites of given mass. The second one describes the number of satellites of given mass that are orbiting inside host haloes *at a given* z_0. This is called *evolved subhalo mass function*, since it is an istantaneous recording satellites which, orbiting inside host haloes, underwent

particular evolutions given by the above described dynamical events (van den Bosch et al. 2005; Giocoli et al. 2008, 2010).

Hereafter we will refer to the subhalo features with lowercase letters and to host halo features with uppercase letters. The pedices m and 0 we will indicate that feature at the redshift of merging z_m and at the observation redshift z_0, respectively. So M_0 is the host halo mass at z_0, while m_m is the satellite mass at z_m.

Our intent here is to derive an average relation between the mass a satellite has at a given moment inside the host halo and the mass it had when it fell in the host, namely between m_0 and m_m. In order to avoid dipendences on the host mass, we will consider the satellite masses *per unit host halo mass*, the latter *at* z_0, thus we will use $x_0 \equiv m_0/M_0$ and $x_m \equiv m_m/M_0$, rather than m_0 and m_m.

In Section 4.1 we will describe and test the pipeline we adopt to collect data from simulations; in Section 4.2 we the obtained subhalo mass functions in LE SBARBINE simulations are illustred; in 4.3.3 we show the relation between x_0 and x_m, while in 4.3.4 we will discuss the relation we found in relation of major mergers; finally in Section 4.4 we will draw some conclusions.

4.1 Data Analysis

We analize the merger trees of haloes identified at 4 different values of z_0, namely $z_0 = 0$, 0.5, 1 and 2 which are more massive than 1000 particles. Since we are interested in average features of merger trees, we avoid those host haloes which accreted more than 10% of their final mass during the merger history, i.e. those host haloes which had, at any redshift, M_m larger of 10% than M_0. The occurance of those kind of peculiar events is larger for low mass haloes identified at low redshift: the maximum abundance is 22% in Ada among haloes identified at $z_0 = 0$, while it decreases to 13% among haloes identified at $z_0 = 2$; in Flora they represent the 2% of haloes identified at $z_0 = 0$. Since it is not part of this work, we will simply ignore those haloes, but these numbers indicate that in certain samples of haloes these events may be significant, thus we stress the importance of further investigation in that direction.

We underline that, as we can see from Table 3.1, Emma and Flora simulations are not suitable for our aims, as they do not provide for a complete sample of neither host haloes and satellites. Therefore, we avoid Emma and Flora simulation from our work, and we focus only on Ada, Bice, Cloe and Dora.

The pipeline we wrote to analyse data follows the above steps:

1. all satellites of all identified haloes are collected. We remind that a satellite, in order to be considered a satellite, is supposed to cede at least 50% of its mass to the MP at the redshift of merging z_m and to contribute with at least 50% of its mass to the initial system at z_0, independently on whether the satellite is still a bound structure at z_0.

2. In order to avoid double counts, caused by, for example, satellites that entered in the MP then exit and then enter again at a further time, or by satellites that enter in a MP and they exit and enter inside a different host, everytime we identify a satellite we check if at least 30% of its particles have already been considered during the whole analysis. If it is true, we neglect that satellite. The 30% threshold is justified by the possible exchange of particles among satellites due to close encounters.

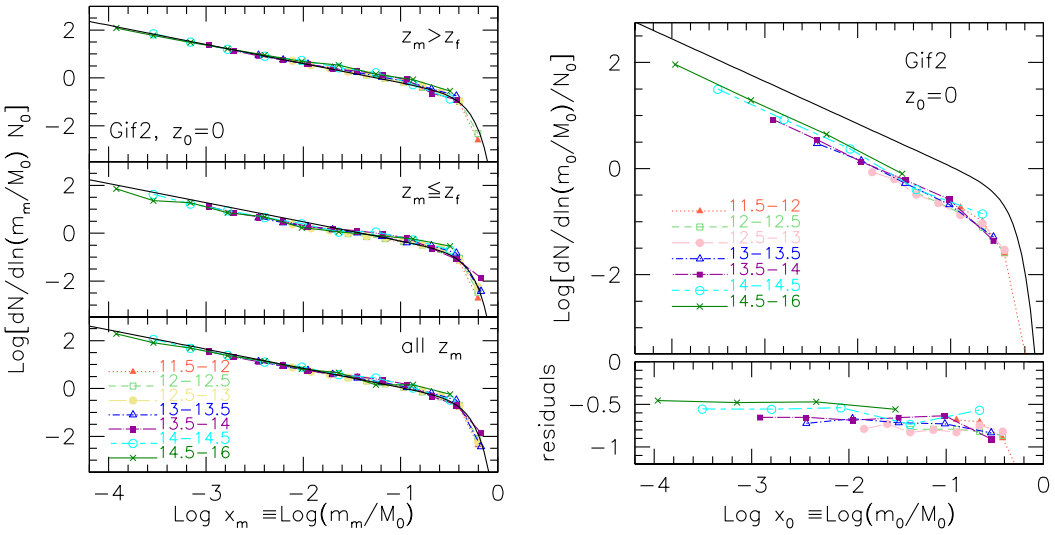

Figure 4.1: *Top*: unevolved subhalo mass functions in simulation `GIF2` of satellites accreted at higher and lower redshift than the host halo formation redshift z_f (top and middle panels, respectively), and at any redshift, in the bottom panel. *Bottom*: evolved subhalo mass functions in simulation `GIF2`. Both unevolved and evolved mass functions are recovered using the new pipeline adopted for this work. Line and point styles refer to $\log M_0/h$ bins, as labeled on the plots, where M_0 is in unit of solar masses. Data are recovered using the new pipeline developed for this work, while black solid lines represent the best fit models for the unevolved mass functions as found by Giocoli et al. (2008).

3. Once we have the catalog of all satellites, we collect those which survived by calculating the binding energy of particles at z_0. Given a satellite, we cycle all its particles and compute their potential energy and kinetic energy with respect to the center of mass. At the end of each cycle, particles with positive net energy are neglected and the new position of the center of mass is derived with the remained particles. The process is repeated until no particles are neglected, so we have a survived satellite, or until the mass falls below 10 particles, thus the satellite is classified as destructed.

4. It is possible that a satellite completely loses its angular momentum while orbiting around the host center of mass and goes to increment the host nucleus. In this case, the satellite would result bound only because it is part of the bound nucleus, but it is no more a particular clump in the host structure. We therefore avoid those survived satellites that are closer to the host center of mass less than 5% of the host virial radius.

Our code is based on the procedure illustrated above, and it allows to derive the unevolved and the evovled subhalo mass functions in a given numerical simulation. In order to test the consistency of our pipeline with results from previous works, we run it on `GIF2` simulations and we compare them with results by Giocoli et al. (2008). The unevolved and the evolved subhalo mass functions are shown for $z_0 = 0$, in left and right panels of Figure 4.1, respectively. In both panels the mass functions are shown for different bins of M_0, the host halo mass at z_0, as labeled in the graphics. The black

name	$N_{sat}(z_0 = 0)$	$N_{sat}(z_0 = 0.5)$	$N_{sat}(z_0 = 1)$	$N_{sat}(z_0 = 2)$
GIF2	122148 (23%)	112311 (25%)	92958 (26%)	56976 (30%)
Ada	1249317 (28%)	1208021 (28%)	1101518 (30%)	811495 (35%)
Bice	1275783 (30%)	1172337 (31%)	995836 (34%)	603371 (40%)
Cloe	1204735 (35%)	1013700 (37%)	758531 (40%)	318148 (47%)
Dora	963082 (41%)	669002 (42%)	375164 (46%)	66184 (52%)

Table 4.1: Total number of satellites found following the main branch of haloes identified at $z_0 = 0$, 0.5, 1 and 2, in the first, second, third and fourth comlumn, respectively. Percentages inside brackets refer to the amount of survived satellites at the four considered z_0.

solid lines represent the analytical form of the unevolved subhalo mass function, as found by Giocoli et al. (2008). The unevolved subhalo mass functions has been derived for satellites accreted at any redshift (bottom panel), at redshift lower and higher than the host formation redshift (middle and top panel, respectively).

The agreement with Giocoli et al. (2008) is excellent. The unevolved subhalo mass function is independent on the host halo mass and on the considered redshift of merging, while the evolved shows a dependence on the host halo mass. We will describe in details the mass functions right above, as we found in LE SBARBINE. Nevertheless, we will refer to those results from GIF2 to do some comparisons.

4.2 Subhalo Mass Functions

The total numbers of satellites accreted at any redshift by all haloes more massive than 1000 particles identified in the 4 considered z_0, are shown in Table 4.1 for all the considered simulations. Percentages inside the brackets indicate the amount of survived satellites at the four observational redshifts. In the following paragraphs we will describe and comment the subhalo mass functions we found in LE SBARBINE simulations.

4.2.1 Unevolved Subhalo Mass Function

Recent works studied the unevolved subhalo mass function of haloes identified at redshift $z_0 = 0$ from GIF2 simulations and found that it is well described by the following power-law:

$$\frac{\mathrm{d}N}{\mathrm{d}\ln(m_m/M_0)} = N_0 x^{-\alpha} \mathrm{e}^{-6.283x^3}, \; x \equiv \frac{m_m}{\alpha M_0}. \tag{4.1}$$

with $\alpha = 0.8$ and $N_0 = 0.21$ for $z_0 = 0$, independently on the value of M_0 (van den Bosch et al. 2005; Giocoli et al. 2008).

In Figure 4.2 unevolved subhalo mass functions found in LE SBARBINE are shown for haloes identified at 4 different observational redshift z_0: 0, 0.5, 1 and 2. Line and point styles in each plot refer to the same mass bin of the host halo mass M_0, as labeled in the upper-left panel, in units of $\log M/M_\odot$. As previously found, we confirm that there is no significant dependence on the host halo mass M_0, so the assembly history of dark matter haloes is scale invariant, independently on z_0. Black solid lines depict the best fitting functions given by equation 4.1 with best fit parameters $\alpha = 0.8$ and $N_0 = 0.19$, in good agreement with previous results, not depending on z_0. We ascribe the small difference obtained in the value of the normalization N_0 to the different values

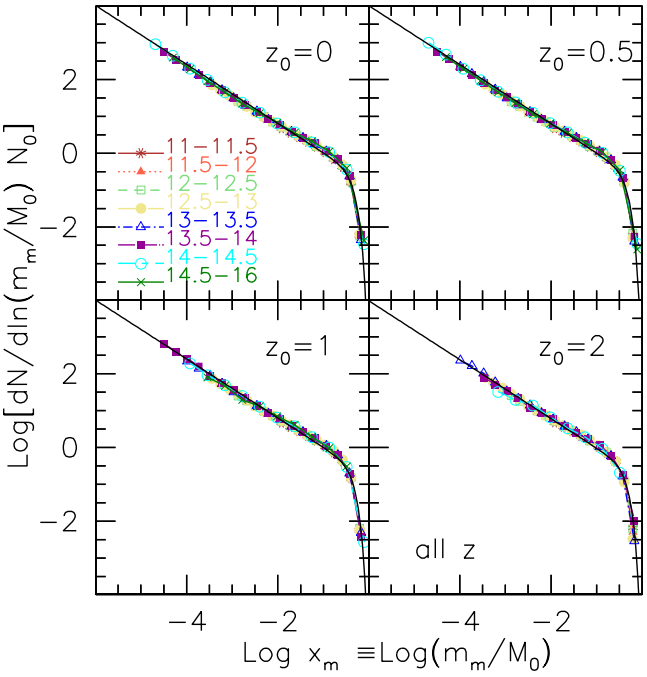

Figure 4.2: Unevolved subhalo mass functions in `LE SBARBINE`, for 4 different values of z_0, as labeled on the plots. Line and point styles refer to $\log M_0/h$ bins, as labeled on the top-left panel, where M_0 is in unit of solar masses. Black solid lines represent the best fit models (see text for more details).

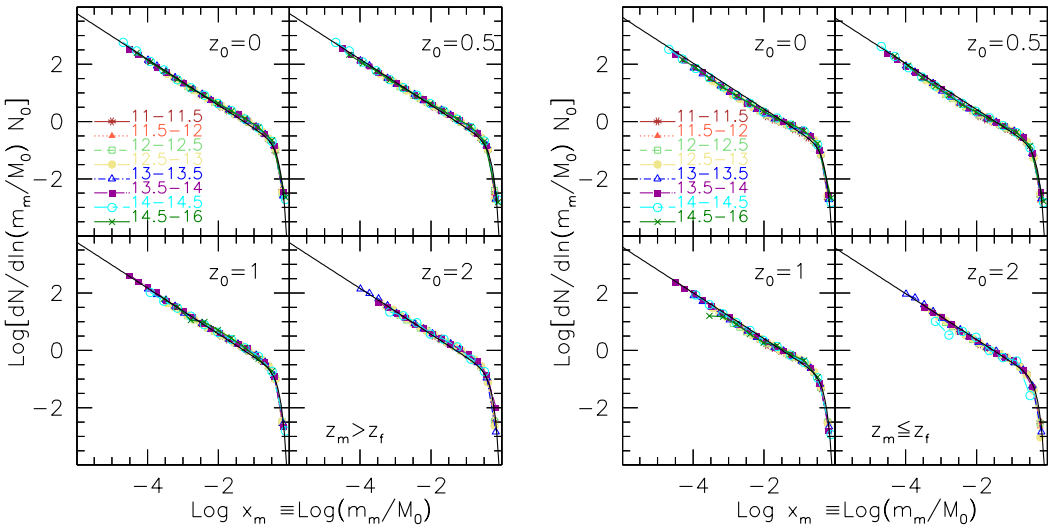

Figure 4.3: Unevolved subhalo mass functions in `LE SBARBINE`, for 4 values of z_0. Line and point styles are the same of Figure 4.2. On the left-hand panel: unevolved mass functions of subhaloes accreted at redshift higher than the host formation redshift. On the right-hand panel: unevolved mass functions of subhaloes accreted at lower redshift.

of cosmological parameters in `GIF2`, in particular to the higher value of σ_8, namely 0.9 rather than 0.8288 as in `LE SBARBINE`.

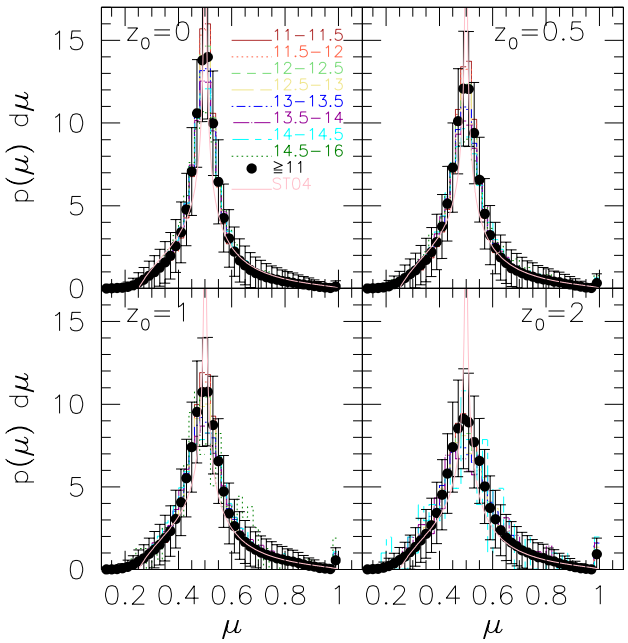

Figure 4.4: Distributions of the mass ratio $\mu \equiv M(z_f)/M_0$ measured in LE SBARBINE simulations. Various line type histogram refer to different final host halo mass bins. We also plot all halo more massive than 10^{11} $M_\odot h^{-1}$, assuming poissonian errors. For $\mu \leq 1/2$ we take the distribution of μ just before the formation redshift. Pink lines describe the theoretical form as found by Sheth & Tormen (2004).

In left and right-hand panels of Figure 4.3 we show the mass functions relative to satellites accreted at redshifts larger and smaller than the formation redshift z_f, respectively, where z_f is defined as the highest redshift at which the MP mass exceeds the half mass of the inital halo, $M(z) > M_0/2$. Although the slope of the fitting functions remains unmodified, the normalizations of the unevolved subhalo mass functions for satellites accreted before and after the formation redshift, namely $N_{0,b}$ and $N_{0,a}$, respectively, are different. Of course we have that $N_{0,a} + N_{0,b} = N_0$, but $N_{0,a} \neq N_{0,b} \neq N_0/2$, since in numerical simulations time is descretized in snapshots. The values of $N_{0,a}$ and $N_{0,b}$ are linked to the value of N_0 through the parameter $\mu \equiv M(z_f)/M_0$, such that

$$N_{0,b} = \bar{\mu} N_0 \quad \text{and} \quad N_{0,a} = (1 - \bar{\mu}) N_0, \tag{4.2}$$

where $\bar{\mu}$ is the mean mass ratio among all haloes in the sample. From the analysis of the large sample of haloes provided in the set LE SBARBINE, we found the distribution of μ showed in Figure 4.4, for all considered z_0. We found the following values of $\bar{\mu}$: $\bar{\mu}_0 = 0.58 \pm 0.09$, $\bar{\mu}_{0.5} = 0.59 \pm 0.09$, $\bar{\mu}_1 = 0.59 \pm 0.1$ and $\bar{\mu}_2 = 0.6 \pm 0.1$, where the subscript indicates the relative z_0. We use these numbers and the relations (4.2) to fix the normalizations of fitting functions in Figure 4.3.

4.2.2 Evolved Subhalo Mass Function

Once satellites enter in the host halo, they start to orbit around the host center of mass. From this moment they may undergo to some dynamical phenomenons which cause the

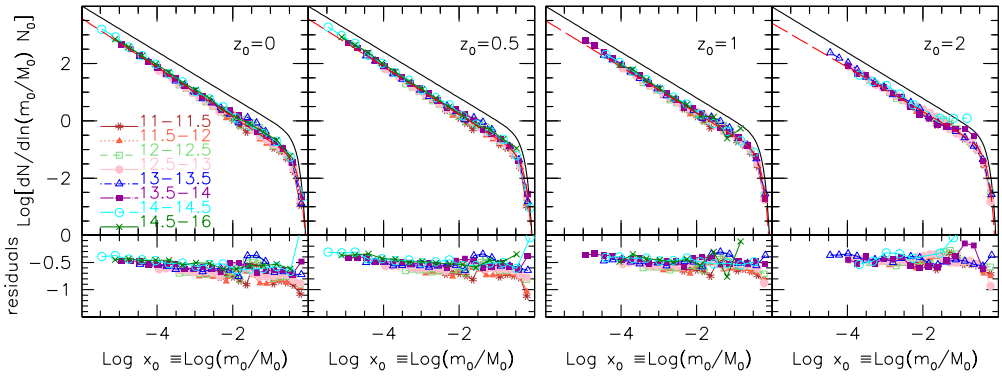

Figure 4.5: Evolved subhalo mass functions as found in simulations `LE SBARBINE` at $z_0 = 0$, 0.5, 1 and 2, from left to right. Point and line style refer to different $M0$ bins, as in previous figures. Residuals with the unevolved mass function (shown with black lines) are shown in bottom panels. Dashed red lines are the best fit functions, which have power-law form as eq. 4.1 with parameters $\alpha = 0.86$, 0.84, 0.81, 0.79 and $N_0 = 0.03$, 0.04, 0.05, 0.07 for $z_0 = 0$, 0.5, 1 and 2, respectively.

partial consuming or even the total destruction of their structure, depending on several factors like satellite orbital parameters and both host and satellite structures. If we take a picture of every host haloes at z_0 and we count all hosted satellites with given mass ratio $x_0 \equiv m_0/M_0$, we are dealing with the so-called *evolved subhalo mass function*.

In Figure 4.5 evolved subhalo mass functions, as found in `LE SBARBINE` simulations, are shown. From left to right, we show results for $z_0 = 0$, 0.5, 1 and 2. Again, the whole sample is divided in 8 subsamples depending on the value of M_0, as labeled on the left-hand panel. On bottom frames we show residuals from the unevolved mass function, which is traced with black solid lines. With dashed red lines lines we fit all points of evolved mass functions using equation (4.1) to have an idea of the average behaviour in function of redshift. We find the slopes $\alpha_0 = 0.86$, $\alpha_{0.5} = 0.84$, $\alpha_1 = 0.81$ and $\alpha_2 = 0.79$, while we find the following normalizations: $N_{0,0} = 0.03$, $N_{0,0.5} = 0.04$, $N_{0,1} = 0.05$ and $N_{0,2} = 0.07$.

We do two main considerations: firstly, we note that the normalization and the slope change with the redshift: as the redshift decreases, the average slope of evolved mass functions differ from the slope of the unevolved, so proportions among small and massive haloes change. This can be explained by a slight dependence of the comsumption process on the satellite mass. If satellites would undergo the same average evolution once they enter inside the host halo, we should expect that the average number of satellites in the hosts decreases independent on satellite masses, and therefore we should expect no significant variation in the slope of evolved mass functions.

Secondly, as already found in previous works, while the unevolved mass function does not depend on M_0, evolved subhalo mass functions do: at every considered redshift, in low mass haloes the average satellite consumption seems to be more advanced with respect to more massive hosts. This is due to the anticipated formation of less massive haloes, so satellites spend more time inside those haloes than inside massive ones and, thus, they get more consumed. In the next paragraph we will use data from `LE SBARBINE` to test those hypotesis.

4.3 Statistics Of The Satellite Mass Evolution

As we already told, satellites orbiting inside the host haloes undergo some dynamical events that result in satellite mass loss. The individual histories of satellite accretion and, consequently, their fate may be very different, but the *average* mass loss of the satellite population has been studied by previous works (e.g. Gao et al. 2004; van den Bosch et al. 2005; Giocoli et al. 2008). We will focus on how the masses of satellites m_0 and m_m, namely being the masses at z_0 and z_m respectively, can be inferred the former from the latter and vice-versa (paragraphs 4.3.2 and 4.3.3, respectively). We remind that we will consider the masses in units of the host halo mass at z_0, that is M_0, so we will deal with $x_0 \equiv m_0/M_0$ and $x_m \equiv m_m/M_0$.

4.3.1 The Role Of Merging Time

In our attempt to analyse the average mass loss of satellites, it is fundamental to discuss the role of the time spent by satellites orbiting inside the host halo. Whichever orbital parameters regulate the satellite trajectory and whichever structural properties the host may have, it is evident that, on average, the longer the time spent inside the host halo, the bigger the satellite mass loss.

In the left-hand panel of Figure 4.6 we show the distribution of mass loss, i.e. the ratio m_0/m_m, for three subsamples of satellites taken from LE SBARBINE simulations, depending on their time spent in the host, namely t_{in}, expressed in Giga years: distributions for satellites identified at $z_0 = 0$, that spent less than 3, from 3 to 8 and over 8 Gyr are shown with solid, dashed and dotted lines, respectively. In terms of redshift, the three distributions refer to satellites accreted at $z_m < 0.3$, $0.3 \geq z_m < 1$ and $z \geq 1$. Percentages inside brackets refer to the size of the three subsamples w.r.t. the whole sample. As expected, the amount of mass loss is directly related to the time spent inside the host. On the right-hand panel we show distributions of the mass loss of satellites inside hosts with three different masses at z_0, namely $\log M_0 = 11 \pm 0.25$, 13 ± 0.25 and 15 ± 0.25 $\mathrm{h^{-1}M_\odot}$. On average, satellites inside low-mass hosts undergo a deeper consumption than satellites accreted by massive hosts. This is directly connected to the model of hierarchical formation of structures, as low-mass haloes formed earlier than massive one, therefore accrete satellites earlier, so at a given z_0 they contain more consumed satellite populations w.r.t. massive haloes. The bottom panel of Figure 4.6, where cumulative distribution of z_m for the same three sub-samples of host haloes examined in right-hand panel are shown, proves this last claim: the median accretion redshift $\tilde{z}_m$ of satellites is higher for low-mass haloes. In particular, we find $\tilde{z}_m \approx 0.8 \pm -0.6$, $0.5^{+0.5}_{-0.3}$ and $0.2^{+0.3}_{-0.1}$ for hosts with logarithmic mass in the bins 11 ± 0.25, 13 ± 0.25 and 15 ± 0.25 $\mathrm{h^{-1}M_\odot}$, respectively. Errors are given by interquartile ranges.

Hence, here we demonstrated the statements we did in the end of the previous paragraph, where we discussed the reasons of the dependence of the evolved subhalo mass functions on the host halo mass.

4.3.2 Average Satellite Mass At z_0

Let's say that we know the redshift of merging z_m and the mass of a subhalo entering in a host, namely $m_m \equiv m(z_m)$. Is there a way to estimate the average mass the satellite will have at a given z_0, namely $m_0 \equiv m(z_0)$? van den Bosch et al. (2005) answered this

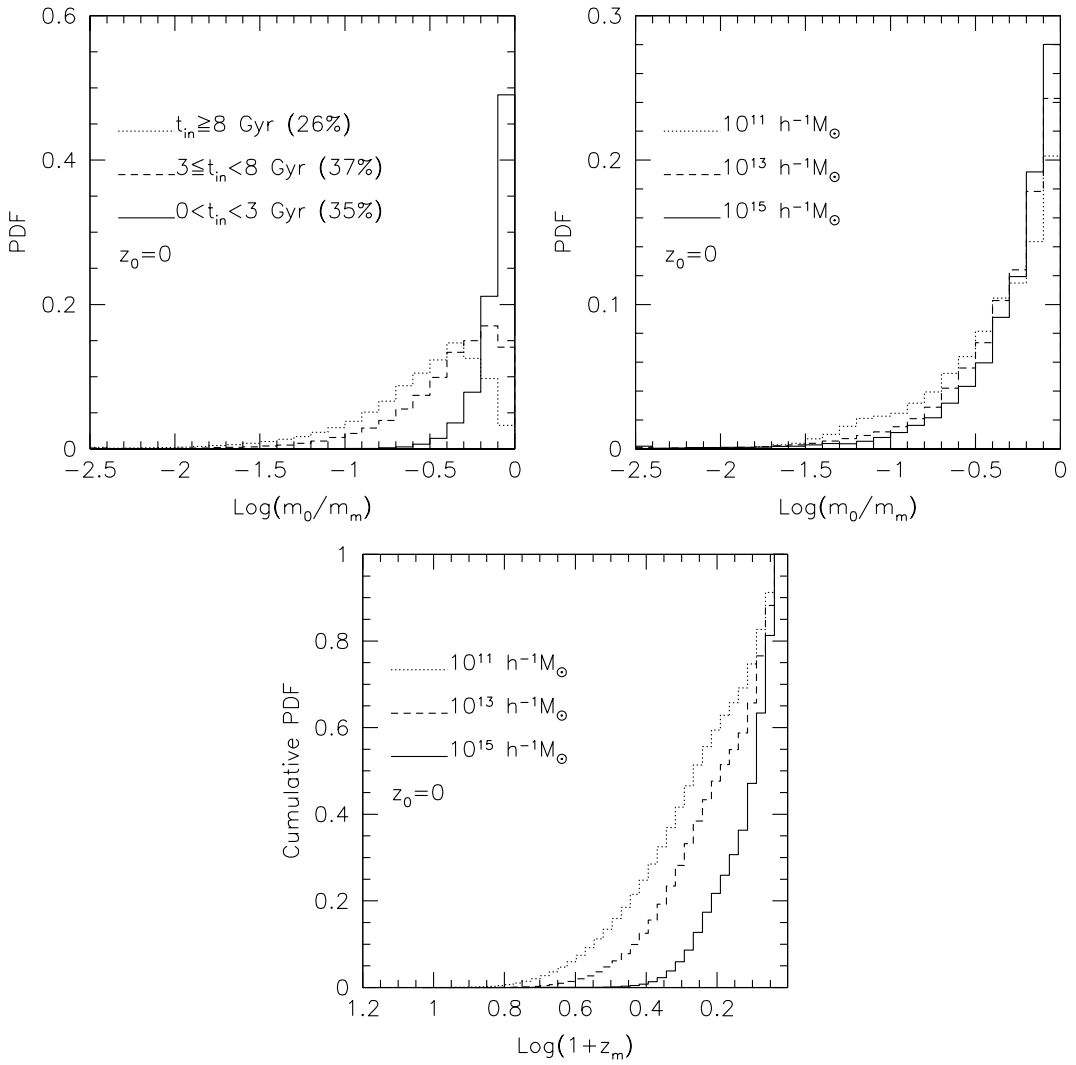

Figure 4.6: *Left-hand panel*: distribution of mass loss experienced by satellites spending a given amount of time inside the hosts: less than 3 Gyr (solid histogram), from 3 to 8 Gyr (dashed histogram) and over 8 Gyr (dotted histogram). *Right-hand panel*: distribution of mass loss experienced by satellites accreted by haloes with the following logarithmic masses at z_0: 11 ± 0.25, 13 ± 0.25 and 15 ± 0.25 $\mathrm{h}^{-1}\mathrm{M}_\odot$, depicted with dotted, dashed and solid histograms, respectively. *Bottom panel*: cumulative distribution of the redshift of merging z_m of satellites accreted by the host sub-sample examined in the right-hand panel.

question proposing the following equation for the mass loss:

$$m_0 = m_m \exp\left[\frac{t_0 - t(z_m)}{\tau(z_m)}\right], \tag{4.3}$$

where times are cosmic times expressed in Gyr and masses in $\mathrm{h}^{-1}\mathrm{Mpc}_\odot$. The quantity $\tau(z_m)$ is the characteristic time scale of the mass-loss rate and it quantify the time dependence we qualitatively illustred in the previous paragraph. Very briefly, they assume that τ is proportional to the dynamical time $t_{dyn} \propto \rho_V^{-1/2}(z)$, where ρ_V is the

average density within the virial radius and, accordingly to the spherical collapse model, is not dependent on the halo mass at fixed redshift. The expression for $\tau(z)$, developed by van den Bosch et al. (2005), is the following:

$$\tau(z) = \tau_0 \left[\frac{\Delta_V(z)}{\Delta_0}\right]^{-1/2} \left[\frac{H(z)}{H_0}\right]^{-1} \tag{4.4}$$

where $\Delta_V(z) \equiv \bar{\rho}(z)/\rho_{crit}(z)$ is the contrast of the average density of a virialized halo with respect to the critical density of the Universe, at a given redshift z, and τ_0 is a free parameter that expresses the characteristic time-scale for subhalo mass-loss at $z = 0$.

Giocoli et al. (2008) derived the following easy expression for $\tau(z)$ from the the analysis of the satellite mass-loss rate in GIF2 simulations:

$$\tau(z) = \exp[-4\log(1+z)+1]. \tag{4.5}$$

We made use of the relation 4.3, along with the approximation for $\tau(z)$ given by the relation (4.5), to evolved the unevolved subhalo catalog we obtained from LE SBARBINE simulations. In Figure 4.7 we show the evolved subhalo mass functions, expressed in terms of satellite masses m_0, derived from the four considered values of z_0, i.e. 0, 0.5, 1 and 2. With solid lines we indicate the direct results from simulations, while with dotted histogram we depict the evolved subhalo mass functions obtained by evolving

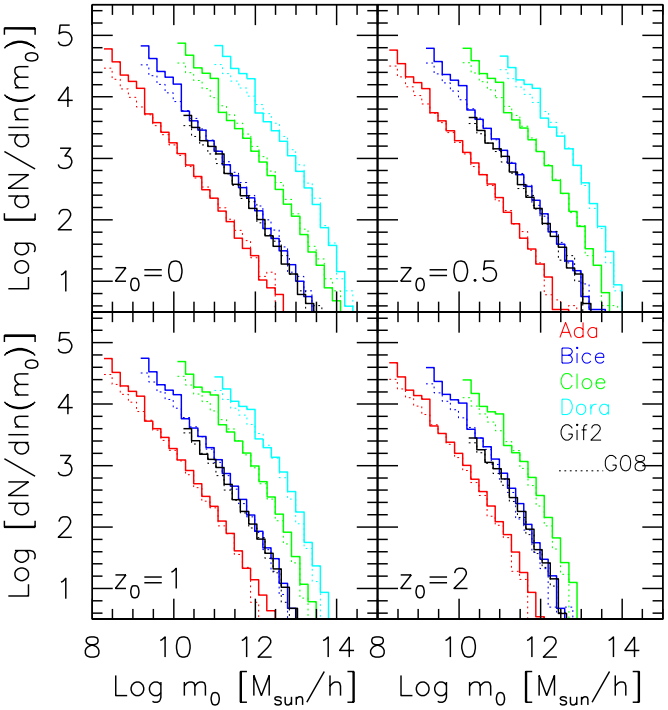

Figure 4.7: Evolved subhalo mass functions in terms of the satellite mass at z_0, instead of the mass ratio $x_0 \equiv m_0/M_0$, as we showed in Figure 4.5, for the 4 considered z_0. Data from Ada, Bice, Cloe, Dora and GIF2 are shown with red, blue, green, cyan and black histograms, respectively. For $z_0 = 2$, Dora does not provide enough data. Dotted histograms indicate the evolved mass functions as resulted by evolving the relative unevolved mass functions by means of the law (4.3).

the unevolved subhalo catalog using equation (4.3). The same color refers to the same simulation: red for `Ada`, blue for `Bice`, green for `Cloe`, cyan for `Dora` and black for `GIF2`. The results from `GIF2` simulations are shown to certify the consistency of our results with previous works. As we can see, the evolution expressed by the power-law (4.3), combined with the approximation for $\tau(z)$ given by equation (4.5), is in excellent agreement with data results from `LE SBARBINE` simulations.

4.3.3 Average Satellite Mass At z_m

In this section we try to answer the following simple question: if we know the mass ratio $x_0 \equiv m_0/M_0$ of a satellite at a given observation redshift z_0, can we infer the mass ratio at the redshift of merging z_m, namely $x_m \equiv m_m/M_0$?

In order to answer this question, we examinate how data from `LE SBARBINE` simulations populate the $\log x_0$-$\log x_m$ plane. In Figure 4.8 we show the plane for every considered simulation (for $z_0 = 2$ we do not use data from `DORA`, because of lack of data) and observational redshift. Colours depict which simulation data come from, while for clarity we mark the bisectors with black solid lines. Of course data occupy only the half-plane above the bisector, since haloes inside hosts can only lose mass. Given a value of x_m, the more distant from the bisector is the relative value of x_0, the more the satellite has lost mass. We immediately note an overpopulated region in the plan, corresponding to $\log x_m$ approximately larger than -2.5, where satellites seem to have undergone a more heavier consumption. We will discuss later this population of satellites.

For every simulation, we divide the $\log x_0$ range $[-5.5, -1]$ in 9 bins with width $\Delta \log x_0 = 0.5$ and find the median $\tilde{x}_m$ inside each bin, which is marked with different point styles and colours relatively to the different simulations. Error bars refer to interquartile ranges. We see that medians from different simulations perfectly overlap, so we fit them with the line $\log \tilde{x}_m = A \log x_0 + B$ and we find that $A \sim 1 \pm 0.01$, so we fix $A = 1$ and minimimize the last squares adjusting only the value of B. Hence, we find that the relation between x_0 and $\tilde{x}_m$ have the following easy form:

$$\log \tilde{x}_m = \log x_0 + B \tag{4.6}$$

with $B = 0.249 \pm 0.021$, 0.245 ± 0.017, 0.243 ± 0.013 and 0.239 ± 0.014 for $z_0 = 0$, 0.5, 1 and 2, respectively.

Equation (4.6) gives the average mass ratio at z_m of a satellite with given mass ratio at z_0 and it seems to be independent on the value of x_0 and very slightly dependent on the observational redshift, so that satellites observed at low z_0 generally undewent a slightly heavier mass loss. However, we can state that satellites were on average 1.75 times (precisely from 1.77 for $z_0 = 0$ to 1.73 for $z_0 = 2$) more massive when they entered inside the host halo.

We then study residuals around the median value $\tilde{x}_m$ averaging the residuals around the relative median value found in every x_0 bin. We precise that we consider residuals around $\log \tilde{x}_m + 1$ instead of $\log \tilde{x}_m$ to better perform the fit. In Figure 4.9 probability density functions for satellites to have a given residual from the median best fit expressed by of equation (4.6) are shown for the 4 considered z_0. Squares indicate the mean abundances of data around the median values among the nine considered x_0 bins and error bars are the standard deviations. Red curves depict the lognormal best fits, for which we leave free only the parameter σ, since the resulting best fit values of the mean

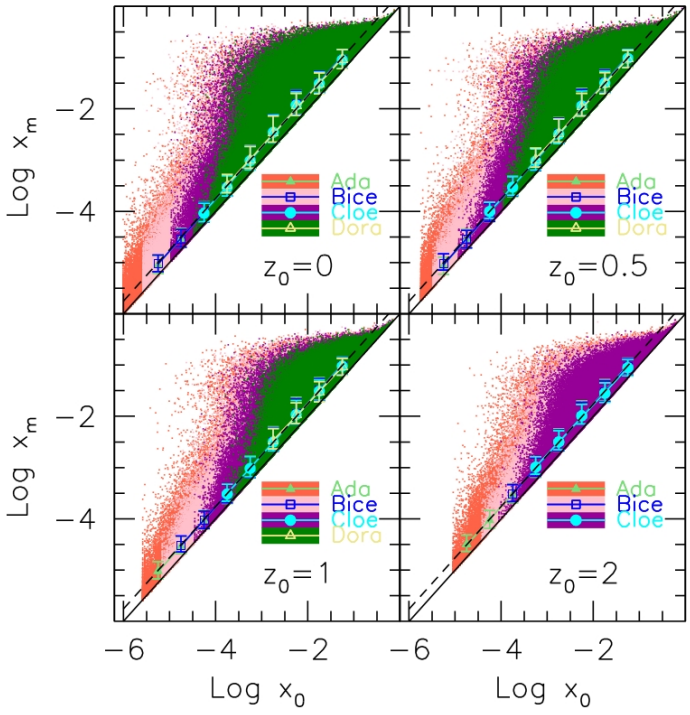

Figure 4.8: Median $\log x_m$ for different bins of $\log x_0$ in LE SBARBINE simulations and for $z_0 = 0, 0.5, 1$ and 2. Coloured regions show the data in every simulation. We show with black dashed lines the best fit of the median points for every z_0. For semplification, we keep the angular coefficient fixed to 1 and adjust only the value of the zero point with the last squares technique.

μ deviate from zero only for some thousandths. Thus, fixing $\mu = 0$, lognormal fits have the form:

$$P(y)\mathrm{d}y = C\frac{1}{\sqrt{2\pi}}\frac{e^{-\left(\frac{\ln^2 y}{2\sigma^2}\right)}}{\sigma y}\mathrm{d}y, \tag{4.7}$$

where we remind that

$$y \equiv 1 + \log x_m - \log \tilde{x}_m = 1 + \log \frac{x_m}{\tilde{x}_m} \tag{4.8}$$

and that C is the normalization constant, so that the whole integral of equation (4.7) is equal to unity. Best fit parameters are $C = 4.34 \times 10^{-3}$, independently on the value of z_0, and $\sigma = 0.131$, 0.127, 0.122 and 0.118 for $z_0 = 0$, 0.5, 1 and 2, respectively.

We underline that equation (4.7), which represents the best fit for residuals around the median expected $\tilde{x}_m$, has no specific physical meaning, but it just gives a qualitative description of how data are, on average, spread around the median value, given by equation (4.6).

4.3.4 The Heavily-Consumed Satellite Population

In this section we examine the $\log x_0$-$\log x_m$ plane at various values of redshift of merging z_m, considering different values of the host mass M_0. We consider six minimum values

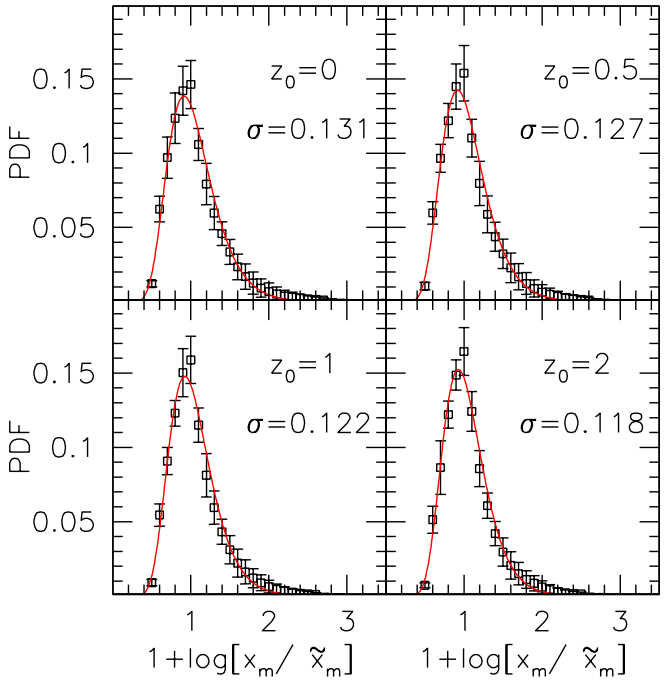

Figure 4.9: Residuals around the median value $\tilde{x}_m$ for the four considered z_0. In order to perform the lognormal fit, we shift the curve around 1 instead of 0.

of z_m, namely 0, 0.5, 1, 2, 3 and 5, and four inferior limits of $\log M_0$: 10.5, 11.5, 12.5 and 13.5, and we populate the plane with satellites which have survived until z_0 and were accreted at redshift higher or equal than z_m by hosts more or equally massive than M_0. In Figure 4.10 we show the results. In each line the minimum mass is kept fixed (we indicate it on the plot, where $M_0 \equiv \log[M_0/M_\odot]$), while each column is characterized by the same value of z_0. In each panel we use different colors to identify the various minimum merging redshift we consider, as labeled, and we also draw the normalized projected histograms along the two axis. Data from `Ada`, `Bice`, `Cloe` and `Dora` simulations are used. The whole set of data is shown in the top-left panel and moving downward host haloes with M_0 lower than the relative mass limits are removed, whereas moving rightward z_0 enhances.

As we expect from the above considerations about the subhalo mass functions, the shape of distributions of x_0 and x_m do not show significant dependences on the observational redshift or on the host halo mass at z_0 (excluding statistically poor bins). Scanning the panels from the top to the bottom, that is excluding less massive host haloes, the shape of the data cloud remains the same but the number of satellites accreted at high redshift reduces. This is due the higher merger rate of massive haloes with respect to less massive. The higher number of dynamical events during their longer assembly history is responsible of the stronger satellite consumtion, therefore it is more likely that satellites accreted in past epochs by massive hosts undergo to a complete destruction.

It is useful to comment the evolution of satellites accreted at different epochs, that is done by scanning panels from the right to the left for a fixed threshold of M_0. The number of early accreted satellites decreases beacuse they have been totally demolished

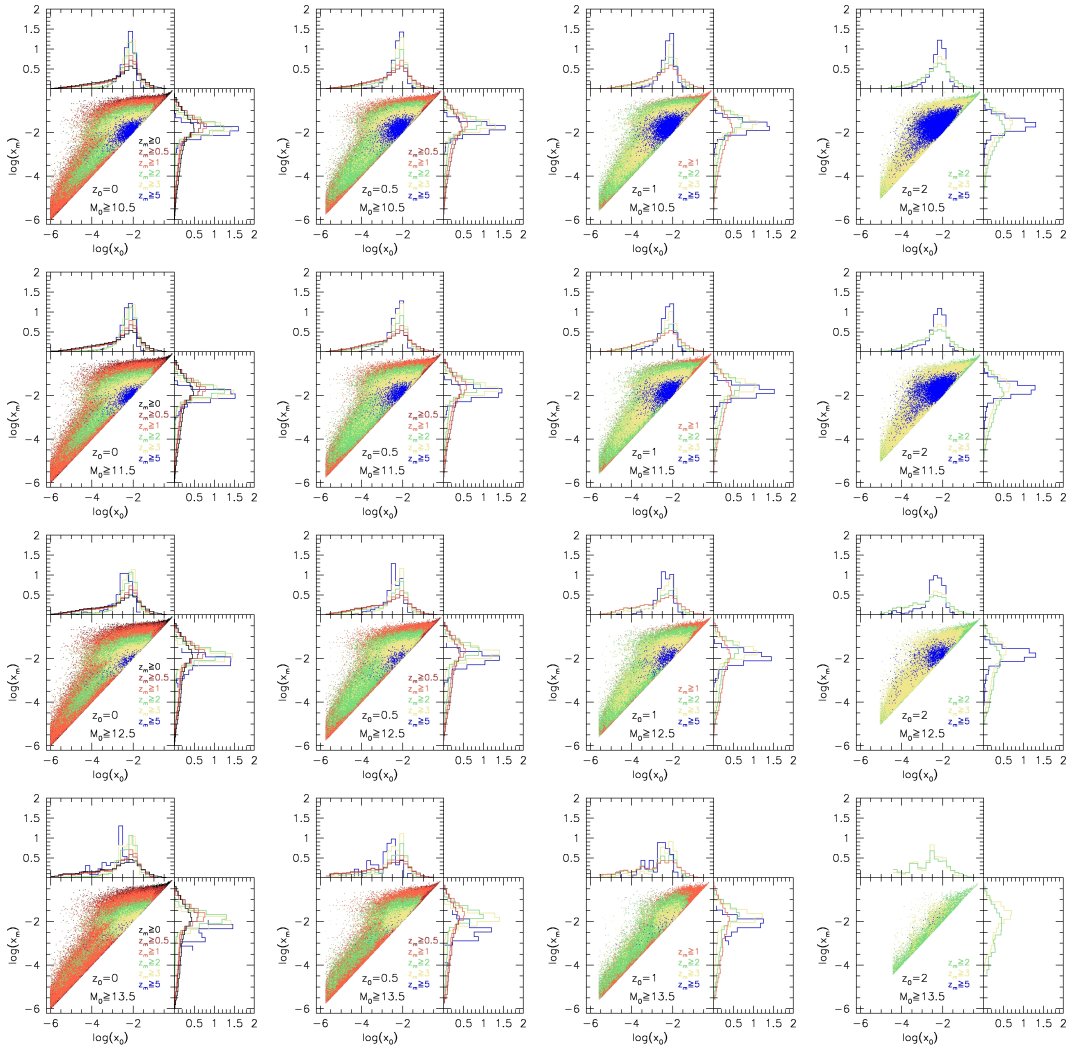

Figure 4.10: The $\log x_0$-$\log x_m$ planes including data from host haloes with mass larger than $M_0 = 10.5$, 11.5, 12.5 and 13.5, from the top to the bottom rows, respectively, at all considered simulations at the four observational redshift $z_0 = 0$, 0.5, 1 and 2, respectively, from left to right columns. Satellites accreted at $z_m \geq 0$, 1, 2, 3 and 5 are depicted by different colours: black, red, orange, green, yellow and blue, respectively. On the small panel we show the projected histograms on the two axis.

or simply their mass fell below the simulation resolution. We remind that all the half plane above the bisector could potentially be populated. From a quite well defined distribution at high z_0, we see that the evolution to recent epochs brings to a bimodal situation at low observational redshifts. There is a region on the top of the planes, corresponding to values of $\log x_m$ approximately larger than -2.5, which seems to be more dispersed along the values of $\log x_0$, like if satellites in this region were on average more consumed. Moreover, the shape of this region suggests that the evolution of some satellites is different from what we found above. We will refer to this kind of satellites, which represent about 10% of the total population, as the Heavily-Consumed (hereafter HC) satellites.

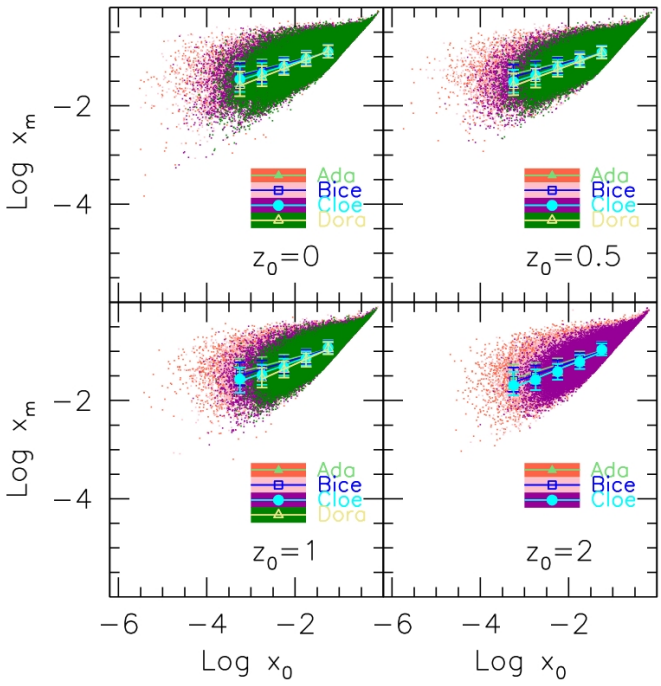

Figure 4.11: Median $\log x_m$ for different bins of $\log x_0$ in `LE SBARBINE` simulations and for $z_0 = 0, 0.5, 1$ and 2. Here only the major mergers population has been considered. Colours are the same of Figure 4.8.

For a first characterization of the HC satellites, we wonder in which case a satellite undergoes more disruptive events, and the simplest answer is during a major merger. With major merger we mean the assembly of a satellite with mass ratio $x_{m,m} \equiv \frac{m_m}{M_m}$ greater or equal than 1/10. We underline that in this case both masses of satellites and hosts are measured at the time of merging, as the pedices m indicate. Thus, the parameter $x_{m,m}$ should discriminate two populations and two different evolution paths for subhaloes: the first one, the most common, for satellites relatively small (less than one tenth) with respect to the host at the moment of merging, so they undergo the standard consumption process we described in above sections; the second one, for satellites with $x_{m,m} \geq 0.1$, which provide a more rapid mass loss.

In Figure 4.11 we propose again the same plots of Figure 4.8 including only major mergers. We fit again the clouds just to have an estimate of the law relating x_0 and x_m in such kind of mergers. The resulting laws, averaged over the simulations, have the following form, good for $-4 < \log x_0 < 0$:

$$\log \tilde{x}_{m,maj} = A_{maj} \log x_0 + B_{maj} \tag{4.9}$$

where $A_{maj} = 0.28 \pm 0.02$, 0.27 ± 0.02, 0.29 ± 0.03 and 0.32 ± 0.02, and $B_{maj} = -0.56 \pm 0.04$, -0.58 ± 0.05, -0.61 ± 0.06 and 0.59 ± 0.06, for $z_0 = 0$, 0.5, 1 and 2, respectively.

In top-left panel of Figure 4.12 we show again the $\log x_0$-$\log x_m$ plane for $z_0 = 0$ and all considered simulations, where we trace in black the region that encloses data that satisfy the condition $\log x_{m,m} \geq -1$, while in red those data that do not. Curves enclose the 99, 68.7 and 50% of data, from the thinnest to the thickest, respectively.

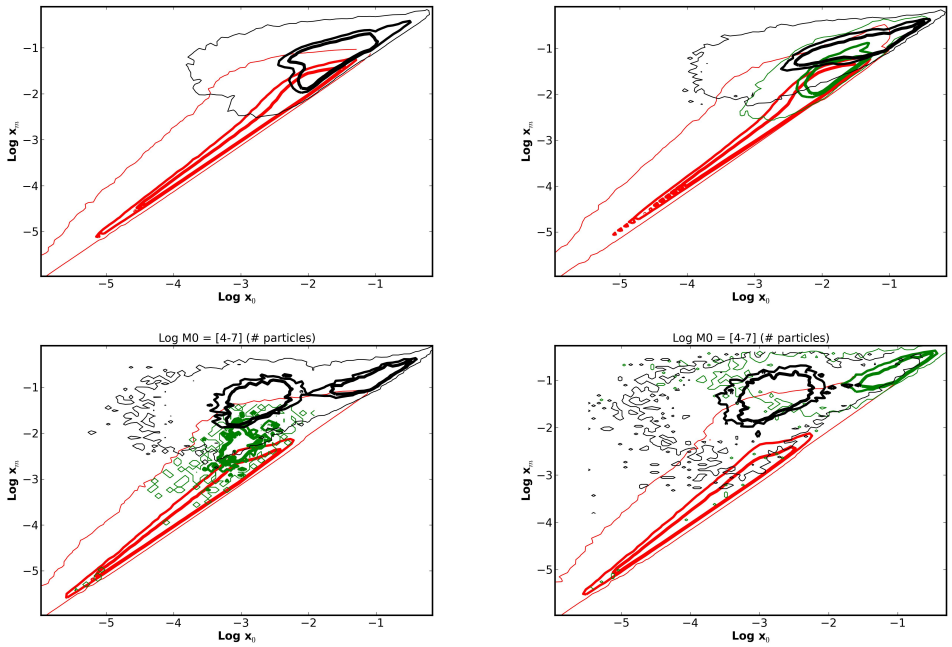

Figure 4.12: *Top-left*: regions containing major and minor mergers, in black and red, respectively, for $z_0 = 0$ and all considered simulations. *Top-right*: same as the left-hand panel, but we add the condition $M_m \geq 500$ particles for major mergers in black, while in green we show major mergers for which $M_m < 500$ and in red all data which are not enclosed in the black region. *Bottom-left*: same of top-right panel but in a sub-sample of massive host haloes, namely more massive than 10^4 particles. *Bottom-right*: black lines enclose major mergers occurred more than 5 Gyr before z_0, green lines enclose major mergers occurred at any time, while red lines enclose all minor mergers. Again, only host haloes more massive than 10^4 particles were considered. In each plot, lines of the same colour enclose the 99, 68.3 and 50% of data, from the thinnest to the thickest, respectively.

We see that the black region still shows bimodality, as if the mass ratio $x_{m,m}$ were not the only condition that characterize HC satellites. After some experimenting, we find that the best discrimination parameter of those two populations that form the whole set of major mergers is the mass of the host halo at the time of merging M_m.

Nevertheless, the amount of survived satellites (self-bound structures more massive than 10 particles at z_0) is larger among major mergers than among minor mergers: if we consider all the simulations we have, for example at $z_0 = 0$, the 62% of major mergers we finf a survived satellite, against the 33% among minor mergers. The possible explanation is that major mergers are more likely to occur at high redshift, thus among early formed haloes, which we remind to have, on average, larger concentration, so they get hardly destructed.

We note from the top-left panel of Figure 4.12 that the shape the region containing the HC population (black lines) suggests the overlapping of two further populations. In top-right panel of Figure 4.12 we isolate with green line the major mergers with hosts having maximum mass at merging M_m equal to 500 particles (for $z_0 = 0$) from major mergers with hosts more massive than 500 particles (included in black contours). The

less massive major mergers seem to follow the same evolution of minor mergers, since the shape of the green cloud does not match the trend of the massive major mergers. Nevertheless, we must consider the influence of resolution: the green cloud contains data relative to satellites which have, at z_m, a mass $50 \leq m_m < 500$ particles, as we defined major mergers when $\log x_{m,m} \geq -1$, thus, those satellites are already small when they fall inside the host and their mass easily falls below the 10 particles resolution limit. In this perspective, if we ideally had not resolution problems, we should see the green cloud extented leftward, in other words toward low values of $\log x_0$. But if that were not a resolution problem, in the ideal simulation we would expect to find the green cloud placed exactly where it is on the top-right panel of Figure 4.12.

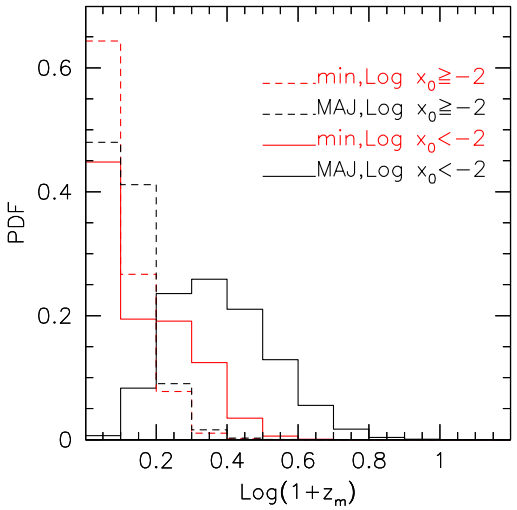

Figure 4.13: Probability density functions to have a minor (major) merger in $\mathrm{d}\log(1+z_m)$, traced by red (black) lines, at $z_0 = 0$. With dashed (solid) lines we show distributions relative to satellites which have $\log x_0 \geq -2$ ($\log x_0 < -2$). Distributions refer to the sub-sample of host haloes more massive than 10^4 particles.

A straightforward way to simulate an ideal simulation is to consider a sub-sample of very massive host haloes at z_0, so a larger portion of the $\log x_0 - \log x_m$ plane can be populated, especially along the $\log x_0$ axis. In bottom-left panel of Figure 4.12 we show the same plot of top-right panel for a sub-sample of host haloes with $M_0 \geq 10^4$ particles. Again, black contours enclose data from major mergers, that is $\log x_{m,m} \geq -1$ where we remind that $x_{m,m} \equiv \frac{m_m}{M_m}$ is the mass ratio at the redshift of merging, with host haloes with mass $M_m \geq 500$ particles, while green contours refer to major mergers with hosts having mass at merging $M_m < 500$ particles. Red lines enclose all data which are not contained in the black cloud. Lines of the same colour enclose the 99, 68.3 and 50% of data, from the thinnest to the thickest, respectively. We see that the green cloud occupies a more central position with respect to the above case, so we can conclude that if the resolution ideally were deeper of two or three orders of magnitude, we would probably see this kind of configuration being the average. Another relevant notation is the presence of two distinct peaks in the distribution of massive major mergers, completely invisible in the top-right panel, thus there is a further discriminating factor which regulates the shape of the HC population. We identify this further discriminating factor with a critical value of the redshift of merging, that we call $z_{m,cr}$, which depends on z_0. The left-hand peak of the black cloud in bottom left panel of Figure 4.12 refers to satellites accreted at $z_m < z_{m,cr}$, while the right-hand peak refers to satellites accreted at $z_m \geq z_{m,cr}$. After some experiments, we find that for satellites identified at $z_0 = 0$, 0.5, 1 and 2, $z_{m,cr} \approx 0.5$, 1, 1.8 and 3, respectively, which correspond to the following times spent inside the host halo (in Gyr): 5, 3, 2 and 1, respectively.

In Figure 4.13 we show the distributions of the redshift of merging in the sub-sample of hosts more massive than 10^4 particles at $z_0 = 0$. Solid lines refer to satellites charac-

terized by low values of x_0, namely lower than -2, while dashed lines refer to satellites with $x_0 \geq -2$. Red and black lines depict minor and major mergers, respectively. Focusing on red lines, i.e. minor mergers, we do not see a significant difference between high and low values of $\log x_0$, except for the more extended tail for low mass-ratio minor mergers, due to the higher abundance of small haloes in early epochs. On the other hand, the behaviour of major mergers in the two cases appears very different: satellites with low and high mass-ratio have very different distributions of z_m. We can roughly say that the low mass-ratio major mergers are, on average, accreted at $z_m < 0.5$ while the high mass-ratio major mergers at $z_m > 0.5$ This is confirmed from the bottom-right panel of Figure 4.12, where we show the bidimensional distributions for the following three populations: major mergers (either massive or not) occurred at $z_m > z_{m,cr}$ with black lines, major mergers at $z_m < z_{m,cr}$ with green lines and any mergers which is not included in the black cloud, with red lines. The green and the black populations form two well separate bulks in the total sample of major mergers. The cases of $z_0 = 0.5$, 1 and 2 give the same results.

4.4 Conclusions

We analysed merger trees from the new set of Dark Matter simulations run in the University of Padova called `LE SBARBINE` (Despali et al. 2016). The whole set is composed by six different realizations of cosmic cubes with the following comoving edges, in units of Mpc/h: 62.5 (`Ada`), 125 (`Bice`), 250 (`Cloe`), 500 (`Dora`), 1000 (`Emma`) and 2000 (`Flora`), each filled by 1024^3 Dark Matter particles, hence having incresing mass resolution from `Flora` to `Ada`. Our aim is to study the relations between the mass a satellite has just before merging with the host halo, i.e. at the redshift of merging z_m, and the mass it has once inside the host, at a given z_0. We consider 4 values for z_0, namely 0, 0.5, 1 and 2. Since the two largest simulations (`Emma` and `Flora`) have too low mass resolutions, we focus only on the first four simulations.

In order to deal only with direct interactions, without including oblique mergers, we only consider subhaloes that give to the host halo at least 50% of their mass at z_m. Furthermore, we check if at least a half of the particles of the initial subhaloes is still inside the host halo at z_0.

We derive the unevolved and evolved subhalo mass functions and we confirm previous results from early works: the unevolved subhalo mass function is not dependent on either the host halo mass at z_0 or the merging redshift z_m. On the other hand, we find the evolved subhalo mass function being dependent on the host halo mass: satellite populations in less massive haloes seem to have undergone a deeper mass-loss. The average characteristics of evolved populations, such as slope and normalisation, are in agreement with previous findings. We also show evidences from data that the time spent in the host halo is determinant for the mass-loss of satellites: low-mass hosts haloes accrete satellites earlier, so those spend a longer time orbiting around the host center of mass and get more consumed.

Using our data from the new set of simulations `LE SBARBINE`, we test the law developed by van den Bosch et al. (2005) and Giocoli et al. (2008) for the satellite mass-loss, expressed by equations (4.3) and (4.5). We find an excellent agreement between the theoretical law and data from `LE SBARBINE`. Thus, the theoretical law gives a way to predict which is the mass of a satellite at z_0, being accreted at redshift z_m and having mass m_m at that moment.

We then give a form to recover the average mass-ratio (where with mass ratio we mean) one satellite had at the moment of merging, given its mass at z_0. We define the quantities $x_0 \equiv m_0/M_0$ and $x_m \equiv m_m/M_0$ as the satellite masses at redshift z_0 and at the redshift of merging z_m, respectively, in units of the host halo mass at z_0. In this way, we avoid possible dependences on the host halo mass. We analyze the $\log x_0 - \log x_m$ plane and find that the average x_m, that we call $\tilde{x}_m$ is related to x_0 through a simple linear equation, namely $\log \tilde{x}_m = \log x_0 + B$, where the parameter B is slightly dependent on z_0. In particular we find $B = 0.249 \pm 0.021$, 0.245 ± 0.017, 0.243 ± 0.013 and 0.239 ± 0.014 for $z_0 = 0$, 0.5, 1 and 2, respectively, that means an average mass at merging greater a factor ~ 1.75 than the mass at z_0. We then derive a form for the residuals around $1 + \tilde{x}_m$, having a lognormal distribution with mean $\mu = 0$ and the variance slightly dependent on z_0, that is $\sigma = 0.131$, 0.127, 0.122 and 0.118 for $z_0 = 0$, 0.5, 1 and 2, respectively. We stress that the lognormal expression for residuals around $\tilde{x}_m$ has not a physical meaning, it just gives a good average description of data. Hence, we found a form for the average satellite mass at the accretion time, without knowing the redshift of merging, in terms of its mass and the mass of the host at z_0.

The analysis of the $\log x_0 - \log x_m$ plane allows a further comment about a subpopulation of satellites whose evolution presents a peculiar behaviour. Besides the majority of data, which place into a cloud roughly parallel to the bisector, we also see a secondary cloud (including about 10% of the total data) placed about at $\log x_m > -2.5$ with different average slope, and it is more evident at low values of z_0, as the evolution occurred for longer time. Because of the elongated tail of this cloud toward low values of $\log x_0$, we call this population as the Heavily-Consumed (HC) population. We identify the HC satellite population as the results of early major mergers, where with major mergers we mean $\log x_{m,m} \equiv m_m/M_m < -1$. We found that the the shape of the HC populations appears to be defined by some features. Firstly, we find a slight difference in position and shape between major mergers with massive and low-mass hosts, where the mass threshold is given by 500 particles at $z_0 = 0$, as if the low-mass major mergers followed the law described by minor mergers. However, we tested by checking a subsample of very massive hosts at $z_0 = 0$ (so we should avoid resolution problems), that this difference is due only by lack of resolution, since for the very massive host subsample the low-mass major mergers appear to follow the behaviour of the whole sample of major mergers. Secondly, we found that, for every considered z_0, a critical value for z_m ($z_{m,cr}$), which discriminates two separate populations of major mergers, can be identified. For $z_0 = 0$, 0.5, 1 and 2 we find that major mergers occurred at redshift lower than 0.5, 1, 1.8 and 3, provide higher mass ratios x_0 at z_0, accordingly to the fact that satellites that spent longer time in hosts get more consumed, but in major mergers this phenomenon appears to have a bimodal behaviour.

Chapter 5

Gravitational Lensing

Gravitational lensing is one of the most spectacular events observed in the Universe. Althought the physical phenomenon is always the same, its display is different depensing on the considered scale:

- on the stellar scale, it expresses as variations on the stellar light curve[1], more precisely as temporary enhancements of the stellar flux. This regime is known as *microlensing*.
- on the scale of galaxies and clusters of galaxies it is possible to observe, in the inner region of an object, *multiple images* or very deformed images coming from another galaxy, sometimes assuming the form of an arc and, therefore, called *gravitational arcs* (see Fig. 5.1). This regime, characterized by strong distorsion and multiple images is called *strong gravitational lensing* (hereafter SL), and we define as *strong lensing clusters* every cluster of galaxy that produce SL effects;
- in the outer regions of cluster of galaxies or very massive galaxies, background galaxies appear very slightly deformed in the tangential direction w.r.t. the distance with the lensing object, in the regime known as *weak lensing* (hereafter WL).

The common explanation for these events lies on the General Relativity: from Einstein field equation we know that the gravitational field preoduced by an arbitrary mass-energy distribution deforms the space-time around, with the consequent deformation of the near geodetic paths (see Fig. 5.2). Thus, the light emitted by a far source and passing through a perturbed region, follows a deformed null geodetic and, therefore, changes direction. This event may lead to three consequences:

1. since more than one null geodetic may exist, different paths are possible around a mass distribution, so from a single source could generate multiple images;
2. considering extended sources, since the number of photons and the surface brightness are conserved, the deformation of the image carries a change in the source flux, being magnified or de-magnified;
3. different paths are covered in different times, so it is possible to observe a time delay among the multiple images of a source.

[1] Flux diagram in function of time.

Figure 5.1: Galaxy cluster Abell 1689, one of the most magnificent examples of strong lensing cluster, observed by HST. Gravitational arcs are clear.

Because of the similarity with optics, every object that acts in this way is called gravitational *lens*.

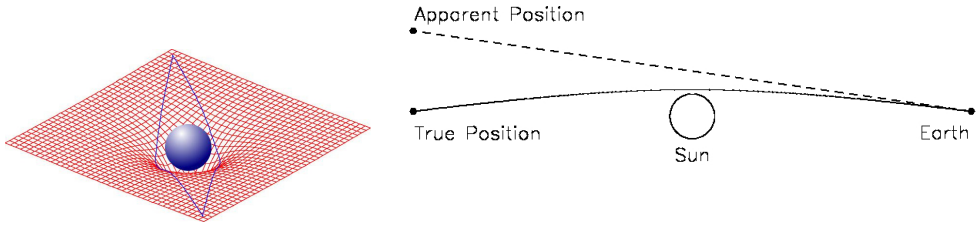

Figure 5.2: *Right-hand panel*: a very simple visualisation of the space-time deformation due to the presence of a mass. *Left-hand panel*: a scheme with the deflection of a light ray due to the sun (Narayan & Bartelmann 1996).

A photon of arbitrary frequency chooses the shortest path to travel from one point to one another, as stated by the *Fermat principle*. Just applying this principle, one can derive a relation between the deflection angle $\vec{\alpha}$ and lens gravitational potential ϕ making two assumptions:

1. the gravitational field is weak, that is $\phi/c^2 \ll 1$, which is true in every astrophysical situation (for a cluster of galaxies $|\phi| < 10^{-4}c^2$);

2. as a consequence of the previous assumption, the deflection angle is small, so we can apply the *Born approximation* (visualised in left panel of Figure 5.3), in other words we can think of the deflection as it were istantaneous in the plane that contains the lens.

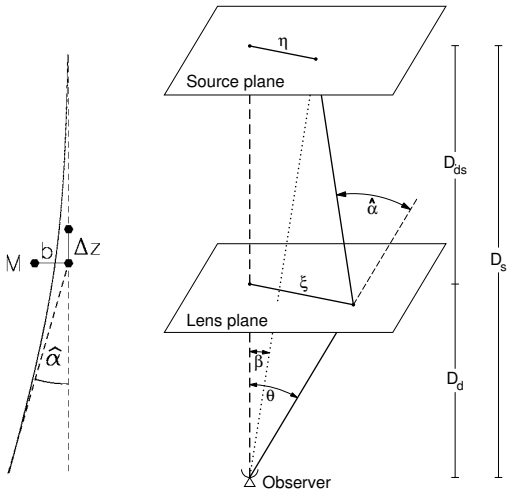

Figure 5.3: *Left panel*: Born approximation (Narayan & Bartelmann 1996). *Right panel*: A schematic view of a lensing system (Bartelmann & Schneider 2001).

Having define with b the impact parameter (the minimum distance between the light path and the lens), the relation between $\vec{\alpha}$ and ϕ is expresses by the following:

$$\vec{\alpha}(b) = \frac{2}{c^2}\int_{-\infty}^{+\infty} \nabla_\perp \phi \mathrm{d}z, \tag{5.1}$$

good for any considered potential. Generally, the *thin screen approximation* is applied: in any case, the size of a lens is always infinitesimal compared to the whole lensing system (source-lens-observer), even if the lens is a cluster of galaxies. Therefore, every lens can be thought as a bidimensional matter distribution that occupies the *lens plane*; the same for sources, which lie on the *source plane*.

Point lens

We consider a point source with mass M, so $\phi = -\dfrac{GM}{r}$, with $r = \sqrt{x^2+y^2+z^2} = \sqrt{b^2+z^2}$. Inside the integral of equation (5.1) we then find $\nabla_\perp \phi = \dfrac{GM}{r^3}\begin{vmatrix} x \\ y \end{vmatrix} = \dfrac{GM}{r^3} b \begin{vmatrix} \cos\phi \\ \sin\phi \end{vmatrix}$. Therefore, the deflection angle for a point source is

$$\vec{\alpha} = \frac{4GM}{c^2 b}\begin{vmatrix} \cos\phi \\ \sin\phi \end{vmatrix},$$

which is

$$|\vec{\alpha}| = \frac{4GM}{c^2 b}. \tag{5.2}$$

Continuous Distribution

The equation (5.2) tells that $|\vec{\alpha}|$ is linear function of mass, then the deflection angle of a planar distribution of N point sources with positions $\vec{\xi}_i$ and masses M_i ($1 \leq i \leq N$) is

$$\vec{\alpha}(\vec{\xi}) = \sum_i \vec{\alpha}_i(\vec{\xi} - \vec{\xi}_i) = \frac{4G}{c^2}\sum_i M_i \frac{\vec{\xi} - \vec{\xi}_i}{|\vec{\xi} - \vec{\xi}_i|^2}. \tag{5.3}$$

Considering a tridimensional distribution and applying the thin screen approximation, the lens mass density $\rho(\vec{\xi}, z)$ is projected on the lens plane to obtain the lens bidimensional mass distribution $\Sigma(\vec{\xi}) = \int \rho(\vec{\xi}, z)\mathrm{d}z$. The deflection angle is given summing the constributes from all elements with mass $\Sigma(\vec{\xi})\mathrm{d}^2\vec{\xi} = \mathrm{d}M$,

$$\vec{\alpha}(\vec{\xi}) = \frac{4G}{c^2}\int \frac{(\vec{\xi} - \vec{\xi}')\Sigma(\vec{\xi}')}{|\vec{\xi} - \vec{\xi}'|^2}\mathrm{d}^2\vec{\xi}, \tag{5.4}$$

where $\vec{\xi}'$ is the position of the element of mass and $\vec{\xi}$ is the position of the light beam.

5.1 The Lens Equation

Every lensing system is characterized by a simply relation that connects the real position of a source to the apparent one and to the deflection angle. We call β the angle which subtends the source real position, θ the angle which subtends the image, and D_S, D_L and D_{LS} the angual diameter distances of the source plane, the lens plane and between lens and source planes (see right-hand panel of Figure 5.3). As we are considering small angles, the virtual position of the source is given by the real one plus the distance caused by the deflection:

$$\hat{\vec{\beta}}D_S + \hat{\vec{\alpha}}D_{LS} = \hat{\vec{\theta}}D_S,$$

which can be written as

$$\hat{\vec{\beta}} = \hat{\vec{\theta}} - \hat{\vec{\alpha}}(\hat{\vec{\theta}}), \tag{5.5}$$

where $\hat{\vec{\alpha}}(\hat{\vec{\theta}}) \equiv \hat{\vec{\alpha}}\dfrac{D_{LS}}{D_S}$ is the *reduced deflection angle*.

It is worth to define an adimensional form of the lens equation mutiplying both members per D_L and multiplying and dividing the first member per D_S. We obtain the following:

$$\vec{\eta}\frac{D_L}{D_S} = \vec{\xi} - \hat{\vec{\alpha}}(\hat{\vec{\theta}})D_L, \tag{5.6}$$

where $\vec{\eta} = \hat{\vec{\beta}}D_S$ and $\vec{\xi} = \hat{\vec{\theta}}D_L$. We also rescale all lenghts with a reference one on the lens plane, namely $\vec{\xi}_0 \equiv \vec{\eta}_0\dfrac{D_L}{D_S}$, and we obtain

$$\vec{y} = \vec{x} - \vec{\alpha}(\vec{x}), \tag{5.7}$$

where $\vec{y} = \dfrac{\vec{\eta}}{\vec{\eta}_0}$, $\vec{x} = \dfrac{\vec{\xi}}{\vec{\xi}_0}$ and $\vec{\alpha}(\vec{x}) = \vec{\alpha}(\vec{\xi})\dfrac{D_L}{\vec{\xi}_0}$.

5.2 Convergence And Lensing Potential

In this thesis we will deal with SL effects by galaxy clusters, in particular gravitational arcs, therefore we now illustrate which are the conditions for these special features to form. We need to define some important properties of the lens that determine its efficiency in producing strong lensing effects.

We start with the *convergence*, defined as the adimensional projected mass density $\kappa(\vec{x}) \equiv \dfrac{\Sigma(\vec{x})}{\Sigma_{crit}}$, where the quantity $\Sigma_{crit} \equiv \dfrac{c^2}{4\pi G}\dfrac{D_S}{D_L D_{LS}}$ separate weak from strong lensing regime. A lens with projected mass distribution Σ so that in some point of the lens plane $\Sigma > \Sigma_{crit}$, thus $\kappa > 1$, is said to have a *supercritical* behaviour.

The *lensing potential* is defined as the projected gravitational potential of the lens on the lens plane. Given the projection of the potential along the z axis $\phi(D_L\vec{\theta}, z)$, the lensing potential is defined as:

$$\hat{\psi}(\vec{\theta}) = \frac{D_{LS}}{D_L D_S}\frac{2}{c^2}\int \phi(D_L\vec{\theta}, z)\mathrm{d}z, \tag{5.8}$$

while its adimensional counterpart is $\psi = \dfrac{D_L^2}{\xi_0^2}\hat{\psi}$. The lensing potential is linked to the deflection angle and to the convergence through two simple relations:

1. $$\vec{\nabla}_x\psi(\vec{x}) = \vec{\alpha}(\vec{x}), \tag{5.9}$$

   in fact, given $\vec{\nabla}_x = \xi_0\vec{\nabla}_\perp$, it is demonstrate that

   $$\vec{\nabla}_x\psi(\vec{x}) = \xi_0\vec{\nabla}_\perp\frac{D_{LS}D_L}{\xi_0^2 D_S}\frac{2}{c^2}\int\phi(\vec{x},\vec{z})\mathrm{d}z = \frac{D_{LS}D_L}{\xi_0 D_S}\frac{2}{c^2}\int\vec{\nabla}_\perp\phi(\vec{x},\vec{z})\mathrm{d}z = \vec{\alpha}(\vec{x}).$$

2. $$\Delta_x\psi(\vec{x}) = 2\kappa(\vec{x}), \tag{5.10}$$

   which is similar to the Poisson equation $\Delta\phi = 4\pi G\rho$.

Using the bidimensional notation, we express the deflection angle through κ as

$$\hat{\alpha}(\vec{\xi}) = \frac{4G}{c^2}\int\Sigma(\vec{\xi}')\frac{\vec{\xi}-\vec{\xi}'}{|\vec{\xi}-\vec{\xi}'|^2}\mathrm{d}^2\vec{\xi}'\frac{\pi}{\pi}\frac{D_L D_{LS}}{D_S}\frac{D_S}{D_L D_{LS}} = \frac{1}{\pi}\frac{D_S}{D_L D_{LS}}\int\kappa(\vec{\xi}')\frac{\vec{\xi}-\vec{\xi}'}{|\vec{\xi}-\vec{\xi}'|^2}\mathrm{d}^2\vec{\xi}'. \tag{5.11}$$

From the adimensional distance $x \equiv \dfrac{\vec{\xi}}{\vec{\xi}_0}$ we obtain

$$\hat{\alpha}(\vec{x}) = \frac{1}{\pi}\int\kappa(\vec{x})\frac{\vec{x}-\vec{x}'}{|\vec{x}-\vec{x}'|^2}\mathrm{d}^2\vec{x}'.$$

Finally, from $\vec{\nabla}\ln|\vec{x}| = \dfrac{\vec{x}}{|\vec{x}|^2}$, we relate the convergence to the lensing potential:

$$\psi = \frac{1}{\pi}\int\kappa(\vec{x}')\ln|\vec{x}-\vec{x}'|\mathrm{d}^2\vec{x}' \tag{5.12}$$

5.3 Distortion, Magnification And Multiple Images

From equation (5.7) we deduce that the deflection of light beams is differential, that is the deflection angle depends on the projected distance between the source and the center of the lens. Considering extended sources, this implicates the deformation of the

image and the source magnification. The deformation is described at the first order by the Jacobian matrix A:

$$A \equiv \frac{\partial \vec{y}}{\partial \vec{x}} = \delta_{ij} - \frac{\partial \alpha_i(\vec{x})}{\partial x_j} = \delta_{ij} - \frac{\partial^2 \psi}{\partial x_i \partial x_j} = \delta_{ij} - \psi_{ij},$$

having defined $\psi_{ij} \equiv \dfrac{\partial^2 \psi}{\partial x_i \partial x_j}$.

The anisotropic part of the tensor A is defined as

$$\left(A - \frac{1}{2}\mathrm{Tr}A \times \mathrm{I}\right) = \delta_{ij} - \psi_{ij} - \frac{1}{2}\left(2 - \psi_{11} - \psi_{22}\right)\delta_{ij} = -\psi_{ij} + \frac{1}{2}\left(\psi_{11} + \psi_{22}\right)\delta_{ij} =$$

$$= \begin{vmatrix} -\dfrac{1}{2}(\psi_{11} - \psi_{22}) & -\psi_{12} \\ -\psi_{21} & \dfrac{1}{2}(\psi_{11} - \psi_{22}) \end{vmatrix}$$

and since the matrix is symmetrical and with null trace, we define the *shear* as the pseudo-vector $\vec{\gamma} = (\vec{\gamma}_1, \vec{\gamma}_2)$ with components

$$\gamma_1 = \frac{1}{2}(\psi_{11} - \psi_{22}) \quad \text{e} \quad \gamma_2 = \psi_{12} = \psi_{21}. \tag{5.13}$$

On the other hand, the isotropic part is

$$\left(\frac{1}{2}\mathrm{Tr}A \times \mathrm{I}\right)_{ij} = \left[1 - \frac{1}{2}\left(\psi_{11} + \psi_{22}\right)\right]\delta_{ij} = (1 - \kappa)\delta_{ij}$$

since, as we already saw, $\dfrac{1}{2}\Delta\psi = \kappa$.

The tensor A can be then written as

$$A = \begin{vmatrix} 1 - \kappa - \gamma_1 & -\gamma_2 \\ -\gamma_2 & 1 - \kappa + \gamma_1 \end{vmatrix},$$

which has the following determinant $\det A = (1 - \kappa)^2 - \gamma^2 = (1 - \kappa - \gamma)(1 - \kappa + \gamma)$. The diagonalisation leads to

$$A = \begin{vmatrix} \lambda_t & 0 \\ 0 & \lambda_r \end{vmatrix}, \tag{5.14}$$

where $\lambda_t \equiv 1 - \kappa - \gamma$ and $\lambda_r \equiv 1 - \kappa + \gamma$ are the tangential and radial eigenvalues, respectively. The relation (5.14) is very useful to understand the meaning of convergence and shear. Considering a circular source, described on the source plane by the equation $y_1 + y_2 = R^2$, and neglecting the shear ($\gamma = 0$), we have that the lens equation is

$$\begin{vmatrix} y_1 \\ y_2 \end{vmatrix} = A \begin{vmatrix} x_1 \\ x_2 \end{vmatrix} = (1 - \kappa)\delta_{ij} \begin{vmatrix} x_1 \\ x_2 \end{vmatrix},$$

that is equivalent to the system

$$\begin{cases} y_1 = (1 - \kappa)x_1 \\ y_2 = (1 - \kappa)x_2 \end{cases}.$$

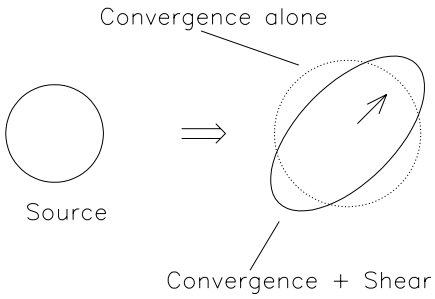

Figure 5.4: The effect of convergence and shear on a circular source (Narayan & Bartelmann 1996).

Adding the squares of the rwo equations we obtain

$$R^2 = (1-\kappa)^2(x_1^2 + x_2^2).$$

Hence, a circular source with radius R is mapped on the lens plan with circular image with scaled radius $\dfrac{R}{(1-\kappa)}$. Therefore the convergence represents the effect of the isotropic component of the Jacobian and modifies the size of the image without changing the shape.

Including also the shear in the example, we have that

$$\begin{vmatrix} y_1 \\ y_2 \end{vmatrix} = (1-\kappa)\delta_{ij} \begin{vmatrix} x_1 \\ x_2 \end{vmatrix} - \begin{vmatrix} \gamma_1 & \gamma_2 \\ \gamma_2 & -\gamma_1 \end{vmatrix} \begin{vmatrix} x_1 \\ x_2 \end{vmatrix},$$

so the system becomes

$$\begin{cases} y_1 = (1-\kappa-\gamma)x_1 \\ y_2 = (1-\kappa+\gamma)x_2 \end{cases},$$

and adding the squares we obtain

$$R^2 = (1-\kappa-\gamma)^2 x_1^2 + (1-\kappa+\gamma)^2 x_2^2.$$

In this case, a circular source is mapped in the lens plane with an elliptical image with dimensions $a = \dfrac{R}{1-\kappa-\gamma}$ and $b = \dfrac{R}{1-\kappa+\gamma}$. The shear quantify the effect of the anisotropic component of the tensor A and the deformation of the image, which from circular becomes elliptical (Figure 5.4).

The lens equation maps a surface element in the source plane δy^2 in a surface element in the lens plane δx^2. The Liouville theorem and the absence of photon emission or absorption during the lensing event guarantee the the photon density in the phase space is conserved, so the source flux must change. The ratio of source and image fluxes is reflects the ratio of the surfaces in source and lens planes occupied by the source and by the image. The *magnification* μ is therefore the ratio of the solid angle sottended

by the image and the solid angle sottended by the source, and it is defined as the determinant of the magnification tensor M, that is the inverted A tensor:

$$\mu \equiv \det M = \frac{1}{\det A} = \frac{1}{(1-\kappa)^2 - \gamma^2}.$$

Since M is a second order tensor, it admit two eigenvalues, linked to the eigenvalues of A:

$$\begin{cases} \mu_t = \dfrac{1}{\lambda_t} = \dfrac{1}{1-\kappa-\gamma} \\ \mu_r = \dfrac{1}{\lambda_r} = \dfrac{1}{1-\kappa+\gamma} \end{cases},$$

where μ_t and μ_r are the tangential and radial components of μ, respectively.

The eigenvalues of A, namely $\lambda_t(\vec{x})$ and $\lambda_r(\vec{x})$, are functions of the coordinates on the lens plane. In the points on the the lens plane $\vec{x}$ where $\lambda_t(\vec{x})$ or $\lambda_r(\vec{x})$ are null, called *critical points*, the magnification diverges in the tangential or radial direction, respectively. Critical points form two separate curves on the lens plane: from the condition $\lambda_r(\vec{x}) = 0$ the *radial critical line* is generated in the inner region of the lens, while from $\lambda_t(\vec{x}) = 0$ the *tangential critical line* is defined, which lies more externally on the lens plane. Using the lens equation, one can map the critical lines from the lens plane to the source plane, finding the radial or tangential *caustic lines*. The divergence of the magnification on the critical lines suggests that in those regions of the lens plane images from background galaxies appear very deformed, as we will see just below.

Image Distortion Near Critical Lines

We now analyse how images get deformed near critical lines. We consider a generic axially symmetrical lens, so that $\Sigma(\vec{\xi}) = \Sigma(|\vec{\xi}|)$, and we let the lens center correspond to the optical axis. In order to know how is the deformation near the critical lines, we compute the Jacobian and we apply it to a point close to the critical line. The deflection angle of an axially symmetrical lens is

$$\hat{\alpha}(\xi) = \frac{4GM(\xi)}{c^2 \xi},$$

which has the following adimensional form:

$$\alpha(x) = \frac{m(x)}{x},$$

where $m(x) = \dfrac{M(x)}{\pi \xi_0^2 \Sigma_{cr}}$ is the adimensional mass included in x, while $M(x)$ is its physical counterpart. The adimensional lens equation is therefore

$$y = x - \frac{m(x)}{x}. \tag{5.15}$$

Since we know that $\vec{\alpha}(x) = \dfrac{m(x)}{x^2}\vec{x}$ and that $\nabla\psi = \vec{\alpha}$, we derive the following form for the convergence

$$\kappa = \frac{1}{2}(\psi_{11} + \psi_{22}) = \frac{1}{2}\left(\frac{\partial \alpha_1}{\partial x_1} + \frac{\partial \alpha_2}{\partial x_2}\right) = \frac{1}{2x}\frac{\mathrm{d}m}{\mathrm{d}x} \tag{5.16}$$

and the following for the first component of shear

$$\gamma_1 = \frac{1}{2}(\psi_{11} - \psi 22) = \frac{1}{2}(x_2^2 - x_1^2)\left(\frac{2m}{x^4} - \frac{\mathrm{d}m}{\mathrm{d}x}\frac{1}{x^3}\right), \tag{5.17}$$

and for the second one

$$\gamma_2 = \psi_{12} = x_1 x_2 \left(\frac{\mathrm{d}m}{\mathrm{d}x}\frac{1}{x^3} - \frac{2m}{x^4}\right). \tag{5.18}$$

Therefore, the Jacobian matrix is given by $A_{ij} = \delta_{ij} - \psi_{ij} = \delta_{ij} - \dfrac{\partial \alpha_i}{\partial x_j}$ and

$$A = 1 - \frac{m}{x^4}\begin{vmatrix} x_2^2 - x_1^2 & -2x_1x_2 \\ -2x_1x_2 & x_1^2 - x_2^2 \end{vmatrix} - \frac{\mathrm{d}m}{\mathrm{d}x}\frac{1}{x^3}\begin{vmatrix} x_1^2 & x_1x_2 \\ x_1x_2 & x_2^2 \end{vmatrix}. \tag{5.19}$$

With equations (5.16), (5.17) and (5.18) we derive that, for axially simmetrical lenses, shear and convergence are related in this way:

$$\bar{\gamma}^2 = \left(\frac{m(x)}{x^2} - \kappa\right)^2,$$

where $\bar{\kappa}(x) = \dfrac{m}{x^2}$ represents the mean value of κ in the region delimited by x. Consequently, we have

$$\gamma(x) = \bar{\kappa}(x) - \kappa(x).$$

Since the tangential critical line was defined as the location of points that satisfy the condition $1 - \kappa(x) - \gamma(x) = 0$, then inside the region enclosed by the tangential critical line we have that $\bar{\kappa} = 1$.

For this kind of lens the determinant of the Jacobian is given by

$$\det A = \frac{y}{x}\frac{\mathrm{d}y}{\mathrm{d}x} = (1 - \bar{\kappa})(1 - 2\kappa + \bar{\kappa}) = \lambda_t \lambda_r$$

and it gives the equations that define the critical lines: $1 - \bar{\kappa} = 0$ for the tangential critical line, while $1 - 2\kappa + \bar{\kappa} = 0$ describe the radial one. These equations represent two circumferences on the lens plane, the first one inner (radial) and the second one outer (tangential). From the equation (5.15) we see that the tangential critical line is mapped in the point $y = 0$ in the source plane, so the tangential caustic line of an axially symmetrical lens is a point. On the other hand, the radial caustic has a circular shape. We will see that when the source lies inside the caustic radial line, multiple images form in the lens plane.

Now we consider the point $(x_c, 0)$, very close to the tangential critical line, thus it satisfies $\dfrac{m}{x^2} = 1 - \delta$, with $|\delta| \ll 1$. The Jacobian matrix in the point $(x_c, 0)$ is given by equation (5.19) (where $m' \equiv \dfrac{\mathrm{d}m}{\mathrm{d}x}$):

$$A(x_c, 0) = 1 - \frac{m(x_c)}{x_c^2}\begin{vmatrix} -1 & 0 \\ 0 & 1 \end{vmatrix} - \frac{m'(x_c)}{x_c}\begin{vmatrix} 1 & 0 \\ 0 & 0 \end{vmatrix} =$$

$$= \begin{vmatrix} 1 + \dfrac{m}{x_c^2} - \dfrac{m'}{x_c} & 0 \\ 0 & 1 - \dfrac{m}{x_c^2} \end{vmatrix} = \begin{vmatrix} 2 - \dfrac{m'}{x_c} & 0 \\ 0 & \delta \end{vmatrix}.$$

Let's suppose that the image in $(x_c, 0)$ of a circular source were elliptical, thus described by the equation

$$\vec{c}(\phi) = \vec{x}_c + \begin{vmatrix} \rho_1 \cos\phi \\ \rho_2 \sin\phi \end{vmatrix}, \tag{5.20}$$

where ρ_2 and ρ_1 are the tangential and radial semiaxis, respectively. Using the lens equation we derive the equation that describes the source:

$$\vec{d}(\phi) = A(x_c, 0)\vec{c}(\phi) = \vec{y}_c + \begin{vmatrix} 2 - \dfrac{m'}{x_c} & 0 \\ 0 & \delta \end{vmatrix} \begin{vmatrix} \rho_1 \cos\phi \\ \rho_2 \sin\phi \end{vmatrix} = \vec{y}_c + \begin{vmatrix} \left(2 - \dfrac{m'}{x_c}\right) \rho_1 \cos\phi \\ \delta\rho_2 \sin\phi \end{vmatrix}.$$

Having assumed a circular source, the terms $\left(2 - \dfrac{m'}{x_c}\right) \rho_1$ e $\delta\rho_2$ must be equivalent, so

$$\left(2 - \frac{m'}{x_c}\right) = \delta\rho_2,$$

from which we have the ratio between the tangential and the radial semiaxis of the image:

$$\frac{\rho_2}{\rho_1} = \frac{2 - m'/x_c}{\delta} \gg 1.$$

Hence, the elliptical image near the tangential critical line has the semiaxis ρ_2 much larger than ρ_1: here a *tangential arc* is formed.

If an elliptical image forms on a point $(x_c, 0)$ close to the radial critical line, so that $1 + \dfrac{m}{2} - \dfrac{m'}{x} = \delta$, the Jacobian will be

$$A(x_c, 0) = \begin{vmatrix} 1 + \dfrac{m}{x_c^2} - \dfrac{m'}{x_c} & 0 \\ 0 & 1 - \dfrac{m}{x_c^2} \end{vmatrix} = \begin{vmatrix} \delta & 0 \\ 0 & 1 - \dfrac{m}{x_C^2} \end{vmatrix}.$$

The ellipse (equation (5.20) is mapped on the source plane as

$$\vec{d}(\phi) = \vec{y} + \begin{vmatrix} \delta\rho_1 \cos\phi \\ \left(1 - \dfrac{m}{x_c^2}\right) \rho_2 \sin\phi \end{vmatrix}.$$

As we supposed a circular source, we have

$$\delta\rho_1 = \left(1 - \frac{m}{x_c^2}\right) \rho_2,$$

so the ratio between tangential and radial semiaxis is

$$\frac{\rho_2}{\rho_1} = \frac{\delta}{1 - m/x_c^2} \ll 1.$$

In this case, the radial semiaxis is much larger than the tangential one, so we get a *radial arc.*

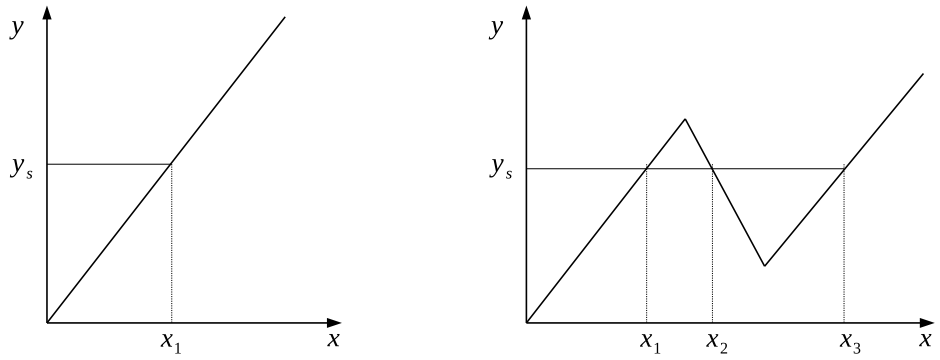

Figure 5.5: The only way to get multiple images is that at least for one y the function $y(x)$ inverted the monotonicity, so $\mathrm{d}y/\mathrm{d}x$=0. If this condition is satisfied, thus exists at least one point y_s corresponding to more values of x.

The Generation Of Multiple Images

Axially symmetrical lenses produce mupltiple images from the same source if at least in one point the following condition is satisfied:

$$\frac{\mathrm{d}y}{\mathrm{d}x} = 1 - 2\kappa + \bar{\kappa} < 0, \tag{5.21}$$

because if in any point $y(x)$ is decreasing, hence a certain value y_s on the source plane will be mapped in more points x on the lens plane (see Fig. 5.5). The change in the sign of $\frac{\mathrm{d}y}{\mathrm{d}x}$ implies that in one point we have $\frac{\mathrm{d}y}{\mathrm{d}x} = 0$: for an axially symmetrical lens this condition correspond to the equation of the critical radial line.

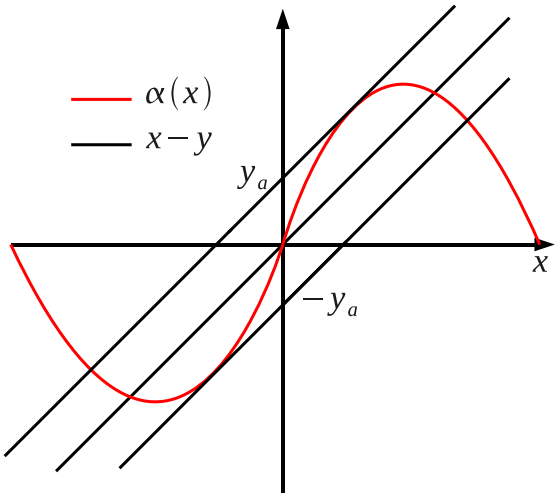

Figure 5.6: The red curve represents a generical function $\alpha(x)$. If $|y| < |y_a|$ lines $y - x$ intercept the curve more than once, while if $|y| > |y_a|$ there is only one intersection.

Projecting on a plane the function $\alpha(x) = \frac{m(x)}{x}$ and observing where $x - y = \alpha(x)$, one defin the *multiple image diagram*. The number of intersections between the line $x-y$ and the curve $\alpha(x)$ is equal to the number of multiple images (the latter being dependent on the source position y) originated by the lensing system (see Fig. 5.6). The condition $\frac{\mathrm{d}\alpha}{\mathrm{d}x} = 1$ defines the radial critical line, as $\frac{\mathrm{d}\alpha(x)}{\mathrm{d}x} = \frac{\mathrm{d}}{\mathrm{d}x}(x - y) = 1$ is satisfied only if $\frac{\mathrm{d}y}{\mathrm{d}x} = 0$. Like in Fig. 5.6, the values y_a that satisfy $\frac{\mathrm{d}y_a}{\mathrm{d}x} = 0$ identify lines which are tangent to the curve $\alpha(x)$: if $|y| > |y_a|$ (the source is outside the radial caustic line) we have one image, while if $|y| < |y_a|$ (the source is inside the radial caustic line) we find more than one image.

5.3.1 Time Delay Surface

A way to study the number and position of multiple images is given my the *time delay surface* analysis. However, before starting this issue, we must introduce the *time delay*. Gravitational lensing is essentially given by a change in the light path from a source to an observer, caused by local space-time distortion due to the presence of a gravitational field. This change implies a difference between times that light takes to travel along straight and bended paths, called *geometrical delay*, Δt_{geom}. Moreover, the presence of a weak gravitational field acts as an effective refraction index $n \approx 1 - \frac{2\phi}{c^2}$ which delays the light beam, causing the so-called *Shapiro delay*, Δt_{grav}. Both those two delays hence contribute to the total time delay $\Delta t = \Delta t_{grav} + \Delta t_{geom}$.

The Shapiro delay is given by the difference among travel times with and without gravitational perturbations:

$$\Delta t_{grav} = \int \frac{\mathrm{d}l}{c'} - \int \frac{\mathrm{d}l}{c} = \frac{1}{c}\int (n-1)\mathrm{d}l = -\frac{2}{c^3}\int \phi \mathrm{d}l, \tag{5.22}$$

where $c' = c/n$ is the effective speed of light in presence of gravitational field. On the other hand, the geometrical time delay is given by

$$\Delta t_{geom} = \frac{\Delta l}{c} = \frac{1}{2c}(\theta - \beta)^2 \frac{D_L D_S}{D_{LS}}. \tag{5.23}$$

Adding equations (5.22) and (5.23) we get the total time delay:

$$\Delta t(\vec{\theta}) = \Delta_{grav} + \Delta_{geom} = \frac{D_L D_S}{D_{LS}} \frac{1}{c}\left[\frac{1}{2}(\vec{\theta} - \vec{\beta})^2 - \hat{\psi}(\vec{\theta})\right](1 + z_l), \tag{5.24}$$

where the definition of lensing potential has been used (equation 5.8). Using the scale lenght ξ_0, we have the following adimensional form for the time delay

$$\Delta t(\vec{x}) = \frac{D_S}{D_L D_{LS}} \frac{\xi_0^2}{c}\left[\frac{1}{2}(\vec{x} - \vec{y})^2 - \psi(\vec{x})\right](1 + z_l),$$

, which defines the time delay surface. The gradient of the time delay surface is given by

$$\nabla(\Delta t) = \frac{D_S}{D_L D_{LS}} \frac{\xi_0^2}{c}\left[(\vec{x} - \vec{y}) - \alpha(\vec{x})\right](1 + z_l), \tag{5.25}$$

since $\nabla\psi(\vec{x}) = \alpha(\vec{x})$ for the property of the lensing potential. Inside the square brackets of equation (5.25) we note the lens equation, therefore images form where $\nabla(\Delta t) = 0$, as requested by the Fermat principle.

Fixed the source position, the time delay is characterise by the paraboloid $f(\vec{x}) = (\vec{x}-\vec{y})^2$ and the function $g(\vec{x}) = \psi(\vec{x})$, the latter being determined by the lens potential. The Hessian matrix of the time delay surface is related to the magnification through the following relation:

$$T_{ij} = \frac{\partial^2(\nabla t)}{\partial x_i \partial x_j} \propto \delta_{ij} - \psi_{ij} = A_{ij} = \frac{1}{\mu_{ij}} \tag{5.26}$$

that is telling us that the more bended the surface where image forms, the less magnified the image; on the ather hand, the less curve the surface, the more magnified the image.

From the time delay surface analysis is clear that the density profile of the lens is essential to determine how many multiple images form and where these are located in the lens plane. In the next section we will examine the image configurations for the simplest analytical models of lens.

5.4 Analytical Lens Models

Since the efficiency of a given object in producing gravitational lensing effects is given by its mass distribution, let's see how we can analytically derive the lensing properties of objects with given known mass distributions. This is also useful to understand how much different realistic lenses and ideal situations are. Nevertheless, the modeling of realistic lenses can take advantage of ideal cases, as we will see.

5.4.1 Singular Isotermal Sphere (SIS)

The SIS has a projected density profile described by

$$\Sigma(\vec{\xi}) = \frac{\sigma_v^2}{2G|\vec{\xi}|} \propto |\xi^{-1}|,$$

since $\Sigma(\vec{\xi}) = 2\int_0^\infty \rho(r,z)\mathrm{d}z$, with $\rho(\vec{r}) = \dfrac{\sigma_v^2}{2\pi G r^2}$, where σ_v is the velocity dispersion of particles. We rescale the projected density profile with $\vec{\xi}_0 = 4\pi\dfrac{\sigma_v^2}{c^2}\dfrac{D_L D_{LS}}{D_S}$ and we use the critical density to write the folling:

$$\Sigma(\vec{\xi}) = \frac{\sigma_v^2}{2G}\frac{\vec{\xi}_0}{\vec{\xi}}\frac{1}{\vec{\xi}_0} = \frac{1}{2x}\Sigma_{crit}. \tag{5.27}$$

From the definition of convergence $\kappa \equiv \dfrac{\Sigma}{\Sigma_{crit}}$ and equation (5.27) we derive the following expression of $\kappa(x)$:

$$\kappa(x) = \frac{1}{2|x|}, \tag{5.28}$$

where the absolute value is used, as the convergence is defined positive. We derive the lensing potential from its general relation with κ - equation (5.9) - and we find

$$\psi = |x|. \tag{5.29}$$

The deflection anglge is given by the gradient of the potential, as stated by the relation (5.10), so we have:

$$\vec{\alpha} = \frac{\vec{x}}{|\vec{x}|} \tag{5.30}$$

with which we write the lens equation in the following way

$$y = x - \frac{x}{|x|}. \tag{5.31}$$

Positions and multiplicity of images are given by the solutions of the equation (5.31): if $|y| < 1$ two solutions (therefore two images) exist, one positive $x_+ = y + 1$ and one negative $x_- = y - 1$, fixed separation $x_+ - x_- = 2$; if $|y| > 1$ we have only one solution.

Fig. 5.7 illustrates the multiple image diagram for a SIS lens. The interception between $\vec{\alpha}(\vec{x})$ and lines $x - y$ occurs two times only for source positions $|y| < 1$. Hence, if the source lie inside a certain scale, there will be two images on the lens plane. In

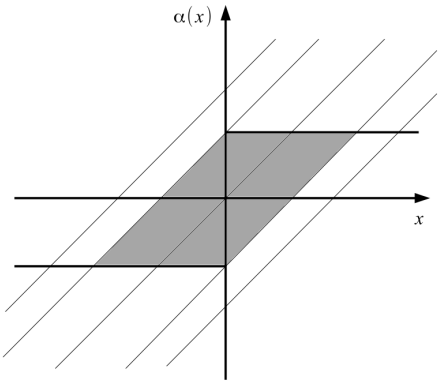

Figure 5.7: Multiple images diagram for a SIS lens. Lines $x - y$ intercept the lines $\vec{\alpha} = \vec{x}/|\vec{x}|$ in two points only for those $|y| < 1$; if $|y| > 1$ there is only one interception and, therefore, one image.

order to define the scale the defines the region where the source has to be to form two images, we consider the normalisation lenght $\vec{\xi}_0 = 4\pi\frac{\sigma_v^2}{c^2}\frac{D_L D_{LS}}{D_S}$, minding that, for a isothermal sphere, we have

$$M(\xi) = 2\pi\int_0^\xi \Sigma(\xi')\xi' \mathrm{d}\xi' = 2\pi\int_0^\xi \frac{\sigma_v^2}{2G}\mathrm{d}\xi' = \frac{\pi\sigma_v^2}{G}\xi.$$

From the latter equation we derive σ_v^2 and we insert it in the definition of ξ_0, getting the following expression for θ_0:

$$\theta_0 = \sqrt{\frac{4GM(\theta_0)}{c^2}\frac{D_{LS}}{D_L D_S}} = \theta_E, \tag{5.32}$$

where θ_E defines the *Einstein radius*. If $y = 0$ the image is a ring with radius that subtend θ_E, while if $y \neq 0$ we must distinguish two cases, depending on β:

1. if $|\beta| < \theta_E$ then $|y| < 1$, two images are generated;
2. if $|\beta| > \theta_E$ then $|y| > 1$, only one image is produced.

Genrally speaking, the Einstein radius separate the strong lensing regime from the weak one and it defines the efficiency of a lens in generating multiple images.

The SIS model is characterised by a prticular relation among shear and convergence: from equations (5.13) we get the component of shear γ_1 and γ_2, so that we can write it as

$$\gamma = \sqrt{\gamma_1^2 + \gamma_2^2} = \frac{1}{2|x|} = \kappa, \tag{5.33}$$

so, for a SIS lens, the measurement of γ gives an estimate of the convergence profile. From this relation, critical lines, defined as the eigenvalues of the Jacobian matrix, are found. The tangential critical line is given by

$$\lambda_t = 1 + \kappa + \gamma = 0$$

and, thanks to the relation (5.33) we obtain

$$x = 1,$$

that is, again, the Einstein radius. The radial critical line is given by

$$\lambda_r = 1 + \kappa - \gamma = 0,$$

but $\gamma = \kappa$, then

$$\lambda_r = 1$$

and it is never null. Thus, this lens model does not originate radial critical lines.

Let's see now the image magnification. Since the radial magnification is $\mu_r = \frac{1}{\lambda_r} = 1$, the image is not magnified in the radial direction, but only in the tangential direction, so

$$\mu = \mu_t = \frac{1}{\lambda_t} = \frac{|x|}{|x| - 1}.$$

Assuming that the source lies inside the Einstein radius, so $|y| < 1$, and considering the positive solution $|x_+| = x_+ = y + 1$, the magnification will be $\mu_+ = 1 + \frac{1}{y}$; if $y \to \infty$ then $\mu_+ = 1$, while if $y \to 0$ then $\mu \to \infty$, as expected: if the source is far from the center of the lens the image does not undergo magnification, while if it is exactly behind the center, the Einstein ring is formed on the tangential critical line, that is the place on the lens plane where $\mu \to \infty$.

In this case, the time delay surface is given by the sum of $(x-y)^2$ with the opposite of the potential $\psi_{SIS}(x)$, where ψ_{SIS} is defined by equation 5.29, and it is characterised by a central cusp (dashed line in Fig. 5.8). If the source is perfectly aligned with the lens, so $\beta = 0$, then the paraboloid is centered in the origin (black line in Fig. 5.8). The time delay surface is shaown in Fig. 5.8 as a red curve, while the points indicate where images form, that is where the Hessian matrix of the surface is null. We find the two symmetrical lateral points, corresponding to the solutions x_+, x_- of the lens equation and to the Einstein radius. Here the curvature is zero and the magnification is infinite, as described by the relation (5.26) between Hessian matrix and magnification. In the

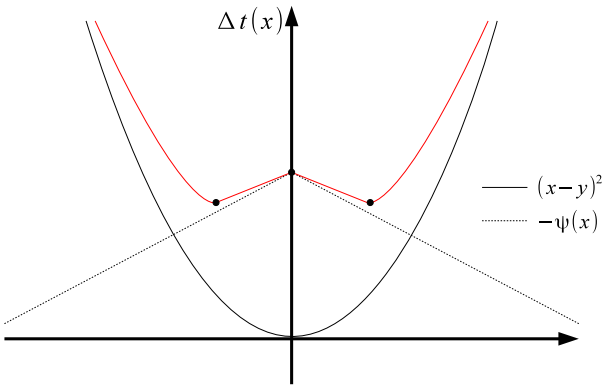

Figure 5.8: The red line represents the bidimensional section of the time delay surface, given adding the palabola $(x-y)^2$ (solid line) with the opposite of the potential (dashed line). We show the case with $\beta = 0$, that is when the source is exactly behind the lens. Points indicate the image positions: the lateral ones correspond to the solutions x_+ and x_-; in the central point the curvature diverges, so the central image is infinitely demagnified and, therefore, invisible.

central cusp, though there is a relative maximum, there is no image since the curvature diverges and the magnification is zero.

We saw that singular spherical lenses produce two images is the sources is closer than the Einstein radius to the lens center. Both images form along the tangential critical line, so they form two tangential arcs, one long and one short, known as *counter-arc*; if the source is exactly behind the lens, the two arcs merge to form the Einstein ring. Moreover, the central singularity of this model does not allow the formation of the radial critical line, so no radial arc is produced.

This kind of image configuration is often observed in strong lensing from galaxies (Bolton et al. 2008), hence it seems they are consistent with a spherical singular profile. It is not clear how the Dark Matter halo (which is supposed to have a NFW profile) combines with baryons to generate this kind of profile. On the other hand, galaxy clusters usually show much complex configurations: radial arcs are found, no counter-arcs are observed and multiple images are much more than two. Thus, it is clear that the most suitable model to describe galaxy cluster must be much more complex than a singular isothermal sphere.

5.4.2 Non-singular Isothermal Sphere (NIS)

We now remove the central singularity from the SIS model adding a *core* inside a certain radius x_c and we obtain a non-singular isothermal sphere (NIS). The lensing potential is given by the following

$$\psi = \sqrt{x^2 + x_c^2}.$$

We note that, in this case, the time delay surface has no central cusp and, then it produces even the central image. From the potential, the deflection angle is derived:

$$\vec{\alpha} = \vec{\nabla}\phi = \frac{\vec{x}}{\sqrt{x^2 + x_c^2}}$$

and therefore the lens equation

$$\vec{y} = \vec{x} - \frac{\vec{x}}{\sqrt{x^2 + x_c^2}}.$$

Convergence and shear are derived from the first derivatives of the components of $\vec{\alpha}$, obtaining

$$\kappa = \frac{1}{2}\left[\frac{x^2 + 2x_c^2}{(x^2 + x_c^2)^{3/2}}\right]$$
$$\gamma = \frac{1}{2}\frac{x^2}{(x^2 + x_c^2)^{3/2}}. \tag{5.34}$$

Like the SIS model, the NIS model shows a simple relation between γ and κ profiles too, which is

$$\kappa = \frac{1}{2}\frac{x^2 + 2x_c^2}{(x^2 + x_c^2)^{3/2}} = \frac{1}{2}\frac{x^2}{(x^2 + x_c^2)^{3/2}}\left(1 + \frac{2x_c^2}{x^2}\right) = \gamma\left(1 + \frac{2x_c^2}{x^2}\right). \tag{5.35}$$

The tangential critical line is defined by relation (5.35), so the condition $\lambda_t = 0$, that is $1 - \kappa - \gamma = 0$, becomes

$$1 - \gamma\left(1 + \frac{2x_c^2}{x^2}\right) - \gamma = 0.$$

Using the expression (5.34) we define the tangential critical line as points that satisfy

$$x_t = \sqrt{1 - x_c^2},$$

so the line exists if the condition $|x_c| < 1$ on the core radius is satisfied.

The same for the radial critical line, define by points where $1 - \kappa + \gamma = 0$, that becomes

$$1 - \gamma\left(1 + \frac{2x_c^2}{x^2}\right) + \gamma = 0.$$

Again, from this equation we derive the following formulation for points on the radial critical line $x_r^2 = x_c^{4/3}(1 - x_c^{3/2})$. We see that both critical lines have the condition $|x_c| < 1$ to exist, so the core radius must be smaller than the Einstein radius.

As we saw in Section 5.3, the condition for critical lines to exist transform in the condition for multiple images to exist. Note in Fig. 5.9 (right-hand panel) that if $x_c = 0$, the multiple images diagram becomes equivalent to the typical step diagram of the SIS case; enhancing x_c, the step gets less steep and the intersection points between curve and $x - y$ the line (so where the curvature of the time delay surface is null and therefore the multiple images) are three. If $x_c = 1$ the curve is tangent to the line, so if $x_c \geq 1$ a single image is generated. In Fig. 5.9 the time delay surface for a NIS lens is shown (left-hand bottom panel), with a source off-axis w.r.t. the lens center (in the top panel β is the source position while the dotted line indicate the center of the lens). Besides the tangential arcs represented by the two lateral points, as in the SIS case, but the

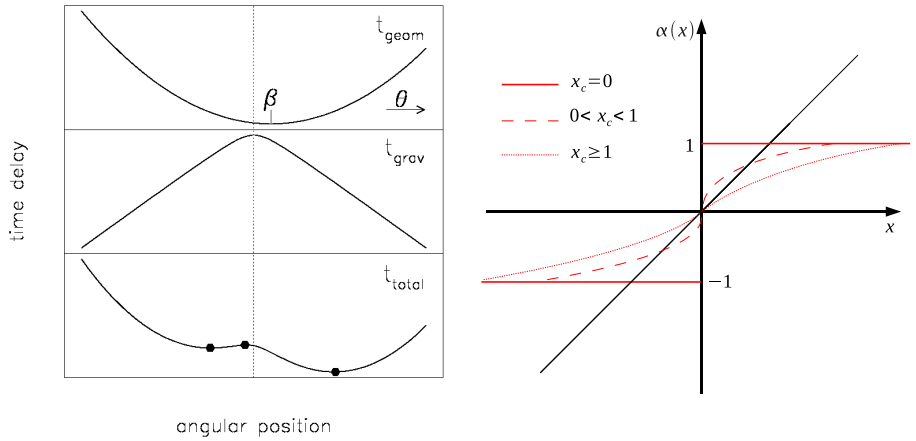

Figure 5.9: *Left-hand panel*: bidimensional representation of geometrical, gravitational and total time delays, top, middle and bottom panels, respectively; β indicates the source position, while black points indicate the image positions; the dotted line depicts the center of the lens (Narayan & Bartelmann 1996). *Right-hand panel*: multiple image diagram for a NIS lens. If the core radius x_c is zero, we find the SIS case (solid line); if the core radius is smaller than the Einstein radius, $0 < x_c < 1$, the line $x - y = 0$ intercept the diagram in three points, where multiple images form; if the core radius is larger than the Einstein radius, $x_c \geq 1$, the intersection is one and no multiple images are formed.

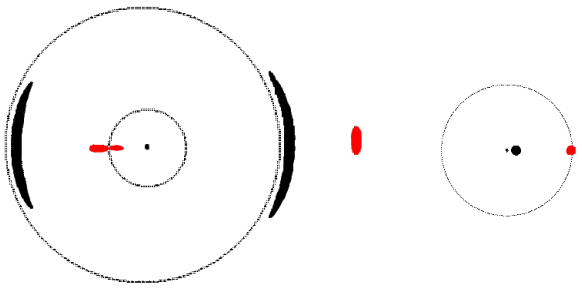

Figure 5.10: Lens and source planes (left-hand and right-hand panel, respectively) of a lensing system with NIS lens. On the lens plane we see the tangential and radial critical lines (outer and inner circle, respectively), while on the source plane we see the tangential caustic line (the central point) and the radial caustic line (the outer circle).

central image has now finite magnification because the time delay surface is continually

deformed in the central point, without any singularity. Therefore, the central image is visible. Fig. 5.10 reports a visulisation of what we described in this section. The lensing configuration with an axially symmetrical lens is shown in the lens and the source plane, left-hand and right-hand panels, respectively. Note critical lines on the left and caustic lines on the right. Also note that critical lines are both circles (the outer one being the tangential critical, while the inner one the radial), and that caustic tangential and radial lines are given by a central point and a circle, respectively. We consider two source positions, depicted in red and black. In red we consider the source lying on the caustic radial line and, consequentely, the formation on the lens plane of three multiple images, two of them deformed in the radial direction and merged in a radial arc. Then we put the source very close to the tangential caustic curve, shown in black on Fig. 5.10. Images on the lens plane are still three, the central one being very demagnified, while the other two are elongated along the tangential direction.

Let's suppose to follow the movement of the source rightward from the center of the lens. The paraboloid of Fig. 5.9 moves rightward and the time delay surface changes: the minimum at the left and the central maximum get closer. between the two points is the radial critical line, more precisely on the point where the curvature changes and where there is the maximum radial magnification. This means that the tangential arcs at the left in Fig. 5.10 moves rightward and get closer to the radial critical line, while the central image moves leftward approaching the tangential arc. The arc tangential magnification decreases and its radial magnification increases. When the source is very near to the radial caustic, the two images higly deform in the radial direction and merge forming a radial arcs. This moment corresponds to the formation of a saddle point in the time delay surface.

Once the source get out the radial caustic, the two images vanish and only the right image remains, in the meanwhile tangetially demagnified. In this moment, the time delay surface has only one stationary point. We now are in the weak lensing regime, where images are single and deformations are very weak in the tangential direction.

5.4.3 Elliptical Lenses

We examined the deformation of images near critical lines for simple spherical models of lens, and we saw that those models are characterised by circular critical and caustic lines and more precisely that the tangential caustic line is a point. The ellipticity of the lens radically changes this configuration, as it is shown in Fig. 5.11, where caustic lines for three different values of ellipticity (from 0 to 4, from the left to the right) are plotted. The tangential caustic, from being a point on the left, get a diamond shape, while the radial caustic becomes an ellipse. Cusps are the points of maximum magnification and the configuration of images depends on whether the source lies near a cusp or near a fold.

In Fig. 5.12 image configurations from a source passing through a fold (on the top panel) and through a cusp (on the bottom) are shown. In the left-hand panel we show the lens plane, while in the right-hand panel the source plane is shown. Every source position and the relative image on the lens plane is marked with different colours.

When the source is perfectly aligned with the lens center, we have five images: the central one and four other ones forming a cross (marked in red in Fig. 5.12). If the source gets close to a fold of the tangential caustic, two of the four images deform in the tangential direction and merge, forming a tangential arc, as it is shown in Fig. 5.12

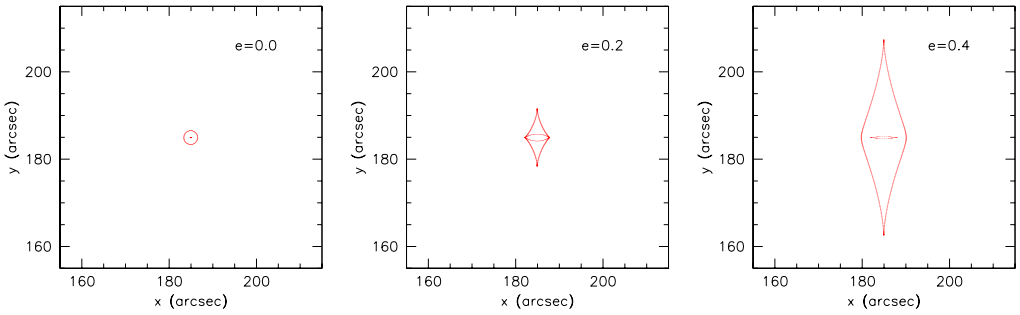

Figure 5.11: From left to right, caustic lines for lenses with different ellipticity, namely 0, 0.2 and 0.4 (Meneghetti et al. 2003a).

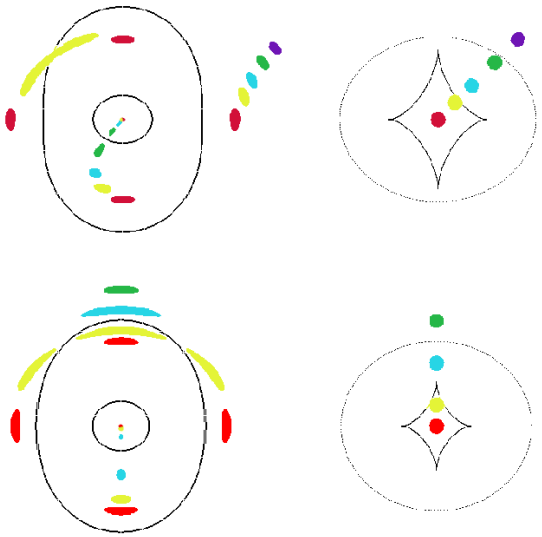

Figure 5.12: Image configuration relative to a source that lies close to a fold (on top panel) or a cusp (on bottom panel); in left-hand panels the lens planes are shown, while in right-panels the source planes are shown. Coloured points indicates the source positions on the source planes and the relative image positions on the lens planes (Narayan & Bartelmann 1996).

with yellow.

When the source passes through a cusp, deformed and merging images are three rather than two (see the bottom panel of Fig. 5.12). The gravitational arc formed this way has larger lenght-to-width (l/w) ratio. When the l/w ratio becomes larger than 10, we define the arc as a *giant gravitational arc*. Going on on following the source toward the outer regions, when it source gets off the tangential caustic, the multeplicity of images decrease of two units; when the source approaches the radial caustic line, the central image and the image outside the radial critical line get closer until they merge to form a radial arc, when the source touches the radial caustic line (see the green configuration in the top panel of Fig. 5.12). When the source is outside the radial custic line, in the lens plane only a weakly tangentially deformed image remains, in the weak lensing regime.

We therefore saw that the formation of gravitational arcs occurs when the source is close to caustic lines. Larger arcs, that means with large lenght-to-width ratio, originate when three images merge, in other words when the source lie on one cusp of the tangential caustic line. Moreover, if the lens is elliptical, the presence of a gravitational arc does not presuppose the existence of any counter-arc, like we noted for spherical lenses.

5.5 Modeling Strong Gravitational Lensing From Galaxy Clusters

We define the Strong Lensing Cross Section (SLCS or $\sigma_{l/w}$) as the area on the source plane where the source must lie to produce arcs with given l/w. Every strong lens is characterised by a $\sigma_{l/W}$, which is a complex function of the geometry of the lensing system, which defines the Σ_{cr}, and the lens structural properties, which determine the projected mass density.

Since one of the aims of this thesis is to do realistic predictions of the number of visible arcs in the sky, we need to model as much realistic strong lenses as possible. The complexity of systems like galaxy clusters makes this task very challenging, even because it is a well established fact that they usually are elliptical, asymmetric, clumpy systems which may contain on-going merger events or an Active Galactic Nucleus (AGN). Since we are interested on the strong lensing efficiency of such systems, quantified by the SLCS, the first thing we must considerate is to identify those structural features that have significant role in the SLCS definition.

In the end of the previous section we concluded observing that lenns ellipticity allows the formation of giant gravitational arcs by merging two or three multiple images, when the source lies on a fold or a cusp of caustic lines. Recently, theoretical studies based on N-body simulations found that the cosmic structures are triaxial and collapsed by elliptical collapse rather than spherical (Sheth & Tormen 1999; Despali et al. 2014; Bonamigo et al. 2014). Moreover, from observations we know that giant gravitational arcs very rarely present counter-arcs, so we deduce that galaxy clusters, which present giant arcs, have elliptical geometry rather than spherical (Grossman & Narayan 1988). Comparing shperical and elliptical models, Meneghetti et al. (2007) and conclude that, for elliptical lenses, triaxiality is responsable of 40% of the SUSL of the lens. Therefore, we conclude the triaxiality is the first feature we must keep in consideration to perform realistic models of strong lenses, especially in dealing with strong lensing galaxy clusters.

5.5.1 Asymmetry, Substructure And Mergers

We saw in section 5.4.3 that giant gravitational arcs form when the source is close to a cusp of the tangential caustic line. The large abundance of giant arcs with respect to small arcs can be interpreted as largely cuspy tangential caustics. Bartelmann et al. (1995) compared numerical models with spherical models of galaxy clusetr with the same observational properties (radius of the nucleus and velocity dispersion) and found that the likelihood of giant arc formation with numerical models is, on average, two order of magnitude larger.

The presence of asymmetry and substructure of a galaxy cluster, as well as enhancing the convergence field, enhances the shear field and heavely contributes to the formation of cusps in the caustic line (Bartelmann et al. 1995); furthermore, asymmetry and substructure are responsable of 40% of the total SUSL of a galaxy cluster (Meneghetti et al. 2007).

In the hierarchical scenario, the evolution of a cluster of galaxies is full of dynamical events among the subhaloes that lie inside the main halo. These mergers modify both the convergence and sehar maps, so it is more likely that in some regions the convergence becomes supercritical and the caustic lenght enhances. This merging phoenomenons may enlarge the SUSL of even one order of magnitude (Torri et al. 2004).

5.5.2 The Baryonic Component

The baryonic content of clusters is mainly in form of:

1. cluster galaxies which occupy the underlying substructure;
2. bright central galaxy (BCG);
3. hot gas;
4. Active Galactic Nucleus (AGN.)

Every of these features may change the convergence and shear maps leading to an enlargement of the SUSL and in the last 15 years a large amount of works investigated on their weight on the enlargement.

The impact of cluster galaxies was discussed by Meneghetti et al. (2000) comparing the SUSL of ismulated clusters with and without cluster galaxies. They found no significative difference among the two options, but a very slight thinning and, rarely, breaks of arcs in the case of clusters with galaxies. A different role is played by the BCG. Meneghetti et al. (2003c) inserted a BCG in simulated galaxy clusters and studied how much the SUSL size modified. The presence of the BCG leads to an enhancement of the SUSL of 50-100%, depending on the BCG mass, profile and orientation. Moreover, from simulations Dalal et al. (2004) found that the BCG influences the angular distribution of arcs. In particular, they distribute more uniformely around the lens center when the BCG is inserted.

The most important effect related to the hot gas which may influence the SUSL size is the cooling flow with star formation, as it steeps the central galaxy cluster density profile. It has been studied that this event could enlarge the SUSL of 100% (Puchwein et al. 2005). However, the presence of an AGN in the center of the galaxy cluster has the opposite effect on the mass profile, since it warms the environment and inhibites

the star formation. (Mead et al. 2010) found that the net combined effect of cooling flows and AGNs is not relevant, as they avoid each other .

Therefore, we conclude that the only baryonic component which must to be considered in modeling strong lensing galaxy clusters is given by the BCG.

5.6 MOKA: A Semi-Analytical Tool For Gravitational Lensing

When dealing with galaxy clusters as gravitational lenses and, in particular, with the modeling of galaxy clusters as strong lenses, there are some structural properties that cannot be ignored. We can summerise them into:

- mass profile,
- triaxiality,
- asymmetry,
- substructure,
- BCG.

Any simulation of galaxy clusters as strong gravitational lenses that does not take into account one or some of those features, could lead to an underestimate of the SUSL size. Of course, including all those characteristics in a model means making use of numerical simulations, which is not always possible or just easy to do. In this context, semi-analytical tools become very important and allow a quick and precise modeling, sometimes reaching the same level of precision given by N-body simulations.

One of those semi-analytical tools is the MOKA code (Giocoli et al. 2012a). MOKA collects simulation-calibrated analytical relations to describe the shape and the content of clusters and creates bidimensional maps of any desired lensing features of the created object, the most important for us being the convergence map. In fact, using the latter one can derive the relative SUSL via ray-tracing technique.

In Giocoli et al. (2012a) is tested that all characteristics listed above are essential for an optimal reproducing of simulated galaxy clusters strong lensing behavior. Finally, it is also very important to note that MOKA is very efficient and allows to quickly generate a lens model within a few seconds of CPU time on a powerful personal computer. Since we aim at simulating a (almost) full-sky survey of strong lensing clusters and at sampling a large number of lines of sight, which requires generating a large number of lenses, in this work we use MOKA to produce the mass distributions which are then analyzed by means of ray-tracing methods.

Chapter 6

Arc Statistics In New Technology Era

6.1 The Number Of Gravitational Arcs As A Cosmological Tool

In the previous chapter we stated that every galaxy cluster has a given efficiency in producing SL features, depending on its structure properties and on the lensing system geometry. We saw that this efficiency is quantified with the Strong Lensing Cross Section (SLCS), the area on the source plane where a source must be in order to be osberved as an arc with given l/w ratio. Once the SLCS is known, the number of arcs produced by an arbitrary strong lens cluster with mass M at redshift z_l is obtained by the following

$$N_{l/w}(M, z_l) = \int_{z_l}^{\infty} \sigma_{l/w}(M, z_l, z_s) n_S(z_s) dz_s, \tag{6.1}$$

where $n_S(z_s)$ is the number density at redshift z_s of sources with surface brightness higher than S. The number of visible arcs in a given survey is therefore given by

$$N_{l/w} = \int_0^{\infty} \int_{M_{min}}^{M_{max}} \frac{dN(z_l)}{dM} \int_{z_l}^{\infty} \sigma_{l/w}(M, z_l, z_s) n_S(z_s) dz_s dz_l dM, \tag{6.2}$$

where dN/dM is the number of strong lenses of given mass M at redshift z_l. It is evident from equation (6.2) that $N_{l/w}$ is strongly affected by the cosmological parameters through the following factors:

- the lens structure: since galaxy clusters are the last results of the cosmic structure evolution, their structure is very sensitive to cosmological parameters;
- the lens spatial abundance, in other words the mass function;
- the lensing system geometry.

The number of observed arcs in the sky, therefore, can be used to constrain the cosmological parameters. This kind of approach to the cosmological research is called *arc statistics*. Since giant gravitational arcs are relatively rare events, their cosmological purpose makes sense only if very large, highly resolved and deep catalogs are available.

Actually there is no catalog that allowed such an application, but it is very likely that in the near future we will have appropriate instruments to get it.

It is worth to mention an almost twenty-year old study by Bartelmann et al. (1998) (hereafter B98), which was determinant for the development of strong gravitational lensing research, in particular of strong lensing from galaxy clusters. Comparing the number of arcs produced by simulated spherical dark matter haloes with the extrapolated number from observations by Luppino et al. (1999), B98 found that in a flat ΛCDM model the expected number of arcs in the whole sky is about one order of magnitude less than the extrapolated observed number. The so-called *arc statistics problem* was source of animated debate in the scientific community, and it led to a strong intensification of the study of cosmic structure features which may increase the SLCS. Though it is evident that a possible origin of the problem lies on the semplicity of B98 lens models, nobody has still solved it and the issue remains open.

6.2 Realistic Arc Statistics Forecasts In A ΛCDM Cosmology

We are living days of strong and quick technological advancement that is conditioning all aspects of our lives, either trivial or important. In the astrophysical and cosmological contexts this is true more then ever. Recent progresses permit both higher resolution power and larger storing space, thus the very recent and the next future observational campaigns are characterized by larger and larger amounts of excellent quality data. From the astronomical point of view, this is the most important feature of the historical moment we are living: the possibility to have access to huge amounts of data, hence the possibility to conduct some kind of investigations which need good statistics. Arc statistics is one of these.

The advent of such large surveys is combined with the need to know the quality of the science that will be possible with the next arc statistics measurements. Therefore, the first thing we wonder is how many arcs will be visible in a next-future wide survey. We refer to the wide field survey performed by the future European Space Agency (ESA) Euclid mission (Laureijs et al. 2011), since it has all characteristics (size, depth) that presume the creation of the largest gravitational arc catalog ever collected.

6.2.1 The Euclid Mission

The Euclid project is part of the ESA program "Cosmic vision 2015-2025", that involves scientits from all ESA member countries. The aim of the program is to fix the most open issues and the necessary technology needed to study them. The main four questions that structure the ESA research plan include all the astrophysical research fields:

1. what are the conditions for planets and life on them to form?
2. how does it works the solar system?
3. which are the fundamental law of the Universe?
4. how was the Universe born and what are its constituents?

Every question includes a set of research themes and the projects for the relative necessary instruments, elaborated by scientists and aerospatial engineers. The need of a

long-term plan comes from the need for aerospatial missions of, on average, 15 years from the proposal to the realization of a given project. Previous successes like the Cassini-Huygens probe, which took 17 years of work, would not have been possible without a solid plan, thus ESA members convinced theirselves to continue to scrupulously plan the missions.

Euclid Main Goals

Euclid is one of the proposed missions answering the "Cosmic Vision" announcement, that enters in the above fourth issue, and it is aimed at the study of the *Dark Universe*. The expression "Dark Universe" involves all components of the Unvierse that still have a misterious nature or behaviour, namely:

- the Dark Energy: it is the presumed responsible of the accelerated expansion of the Universe, the study of its nature passes through the definition of the value of w with the accuracy of 1%, in order to understand whether it is a constant density field (so $w = -1$ and we are dealing with the cosmological constant Λ) or depending on time;

- Dark Matter: its nature is investigated through the parameter m_ν, that is the sum of the three known kind of neutrinos. The larger m_ν, the larger the minimum mass allowed in the structure formation, so its footprint should be visible in the observed power spectrum;

- gravity: the validity of General Relativity can be tested through the measurement of the growth factor γ, related to the growth rate of structures $f(z) = \Omega_M(z)^\gamma$. If measurements led to $\gamma \neq 0.55$, General Relativity should be rejected in favor of another gravity theory. Euclid is supposed to measure γ with a precision of 0.02;

- the initial condition of the Universe: Euclid will measure the power spectrum index of initial fluctuations which, following the simplest inflationary models, should not be dependent on the scale. Combined with Planck[1] results, these mesurements will constraint the promirdial power spectrum and inform about the Gaussianity level of primordial fluctuations, improving Planck results.

The first Euclid main probe is cosmic shear, that is the weak lensing effect originated from the entire cosmic matter content and undergone by all galaxies, through which the matter (either dark and visible) distribution can be determined. The second is baryonic acoustic oscillations (BAO), oscillations in the primordial plasma detectable either at very high z in the angular power spectrum of CMB or at low z in the spatial distribution of galaxies, since a comoving cyclic separation among galaxies has been observed (Eisenstein et al. 2005).

Weak lensing measurements require a resolution better than 1 arcsecond to optimally get the shape of galaxies and to perform photometry in visible and NIR bands to evaluate redshifts of galaxies at $z \geq 2$. Clustering observations require precise spectroscopic measurements in NIR band for galaxies at redshift $0.7 < z < 2.1$, when Dark Energy begain to dominate (Refregier et al. 2010; Laureijs et al. 2011).

[1]The Planck probe, launched by ESA in 2009, maps the CMB on the whole sky with unprecedent precision and angular resolution. Its measurements are significatively contributing to the investigation on the primordial Universe and on the origin of cosmic structures.

Telescope Description

Euclid will detect a main wide survey of about 15000 deg^2 of extragalactic sky and two deeeper (2 magnitudes w.r.t. the main survey) 40 deg^2 secondary survey, which test the slitless spectroscope and control the teloscope stability, focussing more than once the same sky region; nevertheless, even those smaller surveys will play an important role in deep data collecting.

Such measurements can be done only by a stable instrument which suffers of systematics as little as possible and focus on a wide portion of extragalactic sky. The best way to minimize the PSF and to optimize the instrument stability, and, consequently, to get excellent and deep imaging, is to build the telescope in space. Furthermore, atmospheric absorption and emission lines may interfer with spectroscopic measurements which have the target in the near infrared, where the Hα line coming from galaxies at redshift $0.7 < z < 2.1$ should be shifted.

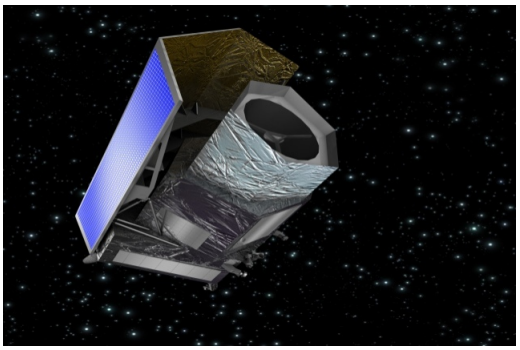

Figure 6.1: A preview of how the spatial telescope Euclid will appear when floating in the sky.

Euclid will be equipped with a 1.2 m Korsch telescope which directs the light through a dicroic filter to the two collecting instruments, both covering the same field of view of 0.54 deg^2: VIS, the visual band instrument, and NISP, that contains a channel for spectroscopy and a channel for the NIR photometry.

The VIS camera is made up of 36 CCD. It will be used to measure galaxy shapes with a 0.1 arcsec resolution in the wide optical band (R+I+Z), from 550 to 950 nm, with sensitivity of 24.5 AB magnitude. The PSF Full Width Half Maximum will be less than 0.2". The NISP spectroscopic channel works in slitless modality in the range 1.1-2.0 micrón, with an average spatial resolution of $l = \frac{\lambda}{\Delta\lambda} \sim 250$; every pixel covers 0.3 arcseconds. The NIR photometry will be in three bands (Y, J, H) with an AB magnitude limit of 24. Therefore, the total covered band by VIS and NISP goes from 550 nm to 2000 nm. While VIS and NISP works in parallel and frame up the same field of view, the two NISP channels works serially through a grism wheel for the spectroscopy and a filter wheel for the photometry (Refregier et al. 2010; Laureijs et al. 2011).

Strong Lensing With Euclid

It has been estimated that in the main survey Euclid will reveal about 60000 galaxy clusters in the redshift range $0.2 < z < 2$, 10000 of them at $z > 1$. We expect that the majority of them will be strong gravitational lenses. The excellent quality imaging and the high magnitude limit will allow an accurate observation of gravitational arcs, adn it will be useful for arc statistics studies.

Since galaxy clusters are the final results of non-linear growth of structure and since SL events trace regions with higher projected density, the identification of SL events at high redshift is useful to constrain the non-linear growth of structures.

Gravitational arcs put constraints on the lens structure, in particular radial arcs constrain the lens inner density profile, while tangential arcs contrain the mass inside

their curvature radius. Moreover, from arc morphology the abundance and distribution of substructures in the main halo can be estimated. Finally, the combination of SL and WL measurements give a precise estimate of the density profiles until large lens radii, from which one can test the ΛCDM model predictions through the concentration parameter. The mass estimated with gravitational lensing measurements is totally independent on assumptions as hydrostatic or virial equilibrium, which are necessary to infer the mass with other known methods.

Finally, gravitational arcs originated from sources at various redshifts are useful to constrain the cosmic geometry. In fact, the difference of the lensing power from the same mass distribution is only due to the system geometry. (Refregier et al. 2010; Laureijs et al. 2011).

6.2.2 Synthetic Haloes

We already said that `MOKA` allows to create mock lenses using a fast semi-analytic approach, through which all the cluster properties that are relevant for strong lensing are incorporated in the lenses. Since we want our modeled strong lensing halos to be as similar as possible to numerically simulated galaxy clusters, we include all features that significantly influence the strong lensing behavior in our computation. In Boldrin et al. (2012) we decided to adopt, among all prescriptions available in the code, the following recipes to model our strong lensing galaxy clusters:

- clusters are assumed to possess a triaxial dark matter halo. The axial-ratios describing the elongation of these halos are drawn following the prescriptions of Jing & Suto (2002). To each halo, a random orientation is assigned;

- dark matter is distributed in the halos such that the averaged azimuthal density profile resembles the Navarro-Frenk-White (NFW) density profile (Navarro et al. 1997). The halo concentration and its dependence on mass and redshift is modeled using the $c - M$ relation of Zhao et al. (2009). A concentration scatter is assumed, which is also based on the analysis of numerically simulated dark matter halos. These typically show that concentrations at fixed mass are log-normally distributed with a rms ~ 0.25, almost independent of redshift;

- dark matter substructures are added to the lens models according to the substructure mass function found by Giocoli et al. (2010). Their spatial distribution is modeled following the cumulative density distribution by Gao et al. (2004). Each substructure is approximated with a truncated Singular-Isothermal-Sphere;

- a central Brightest-Cluster-Galaxy (BCG) is added at the center of the dark matter halos. The stellar content of the BCG is approximated by a Hernquist (1990) density profile. We take into account the influence of the presence of the BCG on the dark matter distribution near the halo center using the recipe by Blumenthal et al. (1986), which analytically describes the adiabatic contraction. The influence of baryons settled on the halo center on the surrounding dark matter distribution has been studied both using analytical calculations and numerical simulations, and during the last years the problem has also been addressed from an observational point of view (Schulz et al. 2010). However recently Newman et al. (2011), modeling the triaxiality of Abell 383, have ruled out baryonic physics which serve to steepen the central dark matter profile. Nowadays this phenomenology is still

an open debate both from a theoretical – where the dark matter behavior seems to strongly depend on the gas physics and treatment of the simulations – and an observational point of view, and further investigations are out of the purposes of this paper. However we want to stress that in the light of what has been shown by Giocoli et al. (2012a) in comparing the strong lensing cross sections of triaxial haloes without and with BCG plus adiabatic contraction, we expect to find a difference of the order of $5 - 10\%$ between clusters with and without adiabatic contraction.

6.2.3 Ray-Tracing Simulations And Cross Sections

By using `MOKA`, we generate three-dimensional cluster models, which we project along arbitrary lines-of-sight. The usage of a semi-analytic formalism allows to quickly compute for each projected mass distribution its deflection angle field on the lens plane. This is used to distort the images of a large number of background sources in order to compute the lens cross sections for giant arcs. The methods employed to measure the cross sections are explained in details elsewhere (see e.g. Meneghetti et al. 2000). Here, we only summarized briefly the procedure.

We use the lens deflection angle maps to trace bundles of light rays from the observer position back to a source plane at redshift $z_{\rm s} = 2$. This is populated with an adaptive grid of elliptical sources, whose spatial resolution increases toward the caustics of the lens. The caustics are lines on the source plane along which the lensing magnification diverges. Therefore, those sources which will be placed near the caustics will be characterized by large magnifications. The magnifications induced by lensing can either be tangential (near the *tangential* caustic) or radial (near the *radial* caustic). The adaptive source refinement artificially increases the number of highly magnified and distorted images. In the following analysis, a statistical weight, w_i, which is related to the spatial resolution of the source grid at the source position, is assigned to each source. If a is the area of one pixel of the highest resolution source grid, then the area on the source plane of which the i-th source is representative is given by $A_i = aw_i$. By collecting the rays hitting each source on the source plane, we produce distorted images of these sources on the lens plane. The images are analyzed individually by measuring their lengths and widths using the method outlined in Meneghetti et al. (2000).

We define the lensing cross section for giant arcs, $\sigma_{l/w}$, as

$$\sigma_{l/w} = \sum A_i \ , \tag{6.3}$$

where the sum is extended to all sources that produce at least one image with $(l/w) \geq (l/w)_{\rm min}$.

6.2.4 Redshift Evolution Of The Cross Section

The cross section is sensitive to several lens properties and it depends on the cosmological parameters and the redshifts of the lens and of the sources. If we pack all the relevant lens properties into the vector of parameters $\vec{p}$ and the cosmological parameters into the vector $\vec{c}$, then the expected number of arcs with $(l/w) \geq (l/w)_{\rm min}$ and surface brightness larger than S that the lens can produce is given by

$$N_{l/w}(\vec{p}, \vec{c}, z_l, S) = \int_{z_l}^{\infty} \sigma_{l/w}(\vec{p}, \vec{c}, z_{\rm l}, z_{\rm s}) n(z_{\rm s}, S) {\rm d}z_{\rm s} \ , \tag{6.4}$$

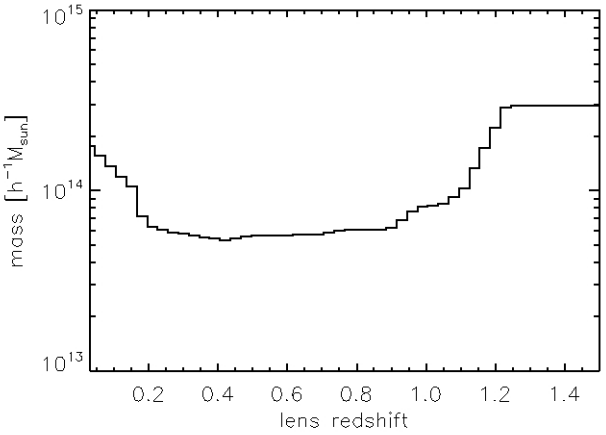

Figure 6.2: Minimal mass for producing giant arcs as a function of redshift, as derived from the simulations by Meneghetti et al. (2010a).

where z_l and z_s are the lens and the source redshifts, respectively, and $n(z_\mathrm{s}, S)$ is the number density of sources with surface brightness larger than S at redshift z_s.

As explained above, we measure the lens cross sections for a fixed source redshift, $z_\mathrm{s} = 2$. The previous formula shows that the cross sections need to be measured at all redshifts above z_l in order to calculate the number of arcs expected from a single lens. In principle, this would imply running ray-tracing simulations for many source planes, which is computationally very demanding, given the number of lenses we are using in this work. Following Meneghetti et al. (2010a), we prefer to determine a *scaling function* to describe the redshift evolution of the cross section. To construct this scaling function we proceed as follows.

Although $\sigma_{l/w}$ depends on a large number of lens properties, $\vec{p}$, we can identify the mass as the primary parameter characterizing the lens. Then, fixing the cosmological framework, we can write:

$$\sigma_{l/w}(M, z_\mathrm{l}, z_\mathrm{s}) \equiv \langle \sigma_{l/w}(\vec{p}, \vec{c}, z_\mathrm{l}, z_\mathrm{s}) \rangle_{\vec{\tilde{p}}} \,, \tag{6.5}$$

where the average is taken over the remaining lens properties, $\vec{\tilde{p}}$ (i.e. substructure content, concentration, triaxiality and orientation). We start by producing halos with `MOKA` spanning three orders of magnitude in mass, in the range $[10^{13} - 10^{16}]$, distributed over the redshift interval $[0 - 1.5]$. Halos are subdivided in 100 logarithmically equi-spaced mass bins and 50 linearly equi-spaced redshift bins. In each (M, z_l) cell, we generate 100 halos with varying properties, $\vec{\tilde{p}}$, to be used for ray-tracing simulations as explained above. Therefore, the number of lenses we should process is $100 \times 50 \times 100 = 500,000$, which is huge and computationally very demanding. The numerical study performed by Meneghetti et al. (2010a) shows that there is a minimal mass $M_\mathrm{min}(z_\mathrm{l})$ at each redshift below which halos are not capable to produce giant arcs. To reduce the computational time, we use their results to avoid the computation of the cross section of halos with $M(z_\mathrm{l}) < M_\mathrm{min}(z_\mathrm{l})$, for which we assume that $\sigma_{l/w} = 0$. This allows us to the reduce the number of halos to be processed using ray-tracing to $\sim 340,000$. The minimal mass adopted in our study is shown as a function of redshift in Fig. 6.2.

We measure $\sigma_{l/w}(M, z_\mathrm{l}, z_\mathrm{s} = 2)$ by averaging the cross sections of all halos in the

$(M, z_{\rm l})$ cell. This allows us to obtain $\sigma_{l/w}(M, z_{\rm l}, z_{\rm s} = 2)$ on a grid in the $(M, z{\rm l})$ plane. Then, we use subsamples of 32 halos randomly chosen in each $(M, z_{\rm l})$ cell to repeat the calculation of the cross sections for source planes at 32 different redshifts between $z_{\rm l}$ and $z_{\rm s,max} = 6$. These source planes are defined such to take into account how rapidly the strong lensing efficiency is expected to to grow with redshift. In particular, for each lens redshift $z_{\rm l}$, we use the *lensing distance* function

$$D_{\rm lens} \equiv \frac{D_{\rm ls} D_{\rm l}}{D_{\rm s}} \, , \tag{6.6}$$

where $D_{\rm l}$,$D_{\rm s}$ and $D_{\rm ls}$ are the angular diameter distances between the observer and the lens plane, between the observer and the source plane, and between the lens and the source planes, respectively. We normalize these functions such that $D_{\rm lens}(z_{\rm s} = 6) = 1$, and we determine the redshifts of the source planes by uniformly sampling the normalized lensing distance at intervals $\Delta D_{\rm lens} = 1/32$. In Fig. 6.3 we show the normalized lensing distances as a function of the source redshift for several lens redshift. Our method to define the redshifts of the source planes ensures that many more source planes are placed in the redshift range where the lensing distance grows rapidly, while less planes are placed where the $D_{\rm lens}$ function becomes flat.

A critical aspect of the ray-tracing simulations and of the measurement of the cross sections may be given by the assumed size of the source galaxies, which is redshift dependent. Gao et al. (2009) studied how strongly the lensing cross sections depend on the source sizes. They found that this dependency is very weak. However, as it does not delay the computation time, we include in our simulations the redshift evolution of the galaxy sizes, which is modeled as follows. Gao et al. (2009) used COSMOS data (Scoville et al. 2007) to measure the redshift evolution of the galaxy effective diameter up to redshift 3 (see their Fig. 1). The median effective diameter measured by Gao et al. (2009) as a function of redshift is shown in Fig. 6.4. The curve has been extended to redshift 6 by assuming no evolution of the galaxy sizes above $z = 3$. We use this function for setting the size of the sources as a function of redshift in our ray-tracing simulations.

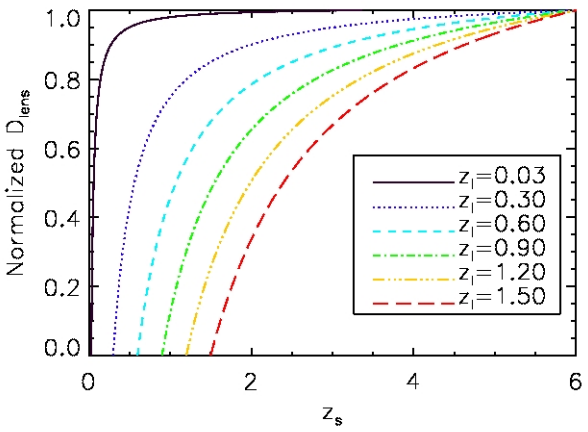

Figure 6.3: Normalized lensing distance as a function of z_s for 5 different z_l values, as shown in the label.

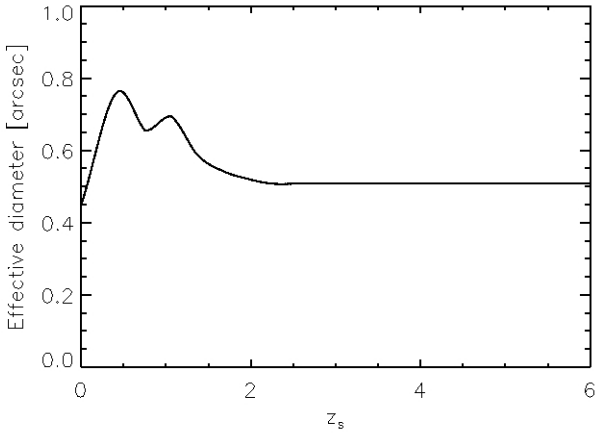

Figure 6.4: Apparent effective diameter as a function of redshift, as found by Gao et al. (2009).

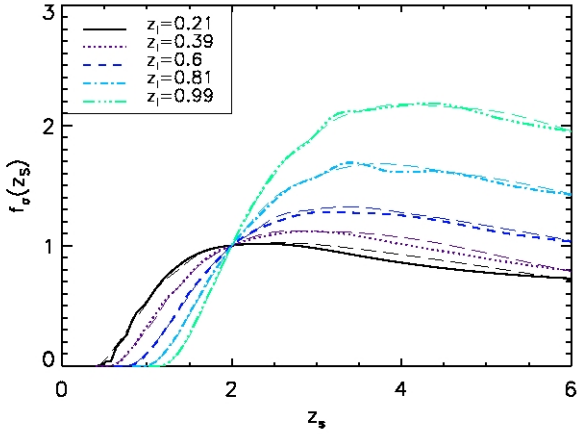

Figure 6.5: Median scaling functions derived from a sample of 32 lenses with $M \approx 10^{15}h^{-1}M_{\odot}$ for five z_l values, as shown in the figure label. The thick (long-dashed) lines refer to functions computed without accounting for the source size dependence on redshift while thin lines are not.

Having measured the cross sections for the different source planes, we can construct the scaling functions

$$f_{\sigma}(M, z_{\rm l}, z_{\rm s}) \equiv \frac{\sigma_{l/w}(M, z_{\rm l}, z_{\rm s})}{\sigma_{l/w,0}(M, z_{\rm l}, z_{\rm s} = 2)} \,, \tag{6.7}$$

where $\sigma_{l/w}(M, z_{\rm l}, z_{\rm s})$ is estimated by averaging over the 32 halos for each source plane. Some examples of the scaling functions for halos with mass $10^{15}h^{-1}M_{\odot}$ at several redshifts are shown in the Fig. 6.5. By construction all scaling functions intercept at $z_{\rm s} = 2$, where $f_{\sigma} = 1$. In Fig. 6.5, the thin lines that almost overlap the curves represent the scaling functions listed above computed without accounting for the source size dependence on redshift. As we can see, there is no remarkable difference among curves, hence

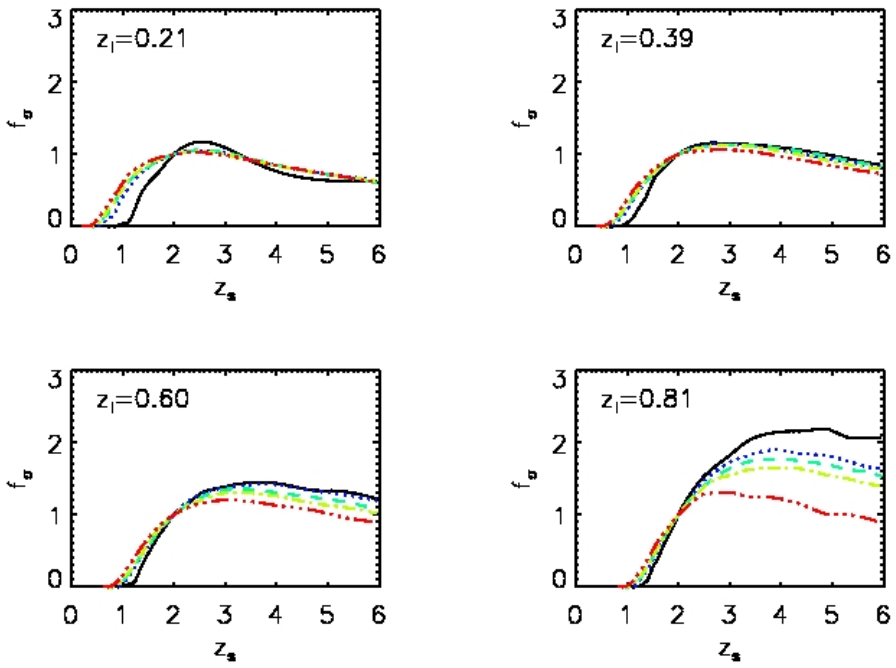

Figure 6.6: Scaling functions at four different lens redshifts. Starting from the upper left panel and continuing to the bottom right, the results refer to lenses at $z_l = 0.21, 0.39, 0.6$ and 0.81, respectively. In each plot we show the curves corresponding to five different masses, namely $2 \times 10^{14} h^{-1} M_\odot$ (black solid line), $4.5 \times 10^{14} h^{-1} M_\odot$ (blue dotted line), $7.5 \times 10^{14} h^{-1} M_\odot$ (cyan dashed line), $10^{15} h^{-1} M_\odot$ (green dot-dashed line) and $3.2 \times 10^{15}\, h^{-1} M_\odot$ (red double dot-dashed line).

we can state that source size dependence on redshift does not significantly affect the final number of arcs. Anyway, as already said, adding this feature does not change the computational time, so we decide to consider it in our implementation.

Note that the scaling functions depend not only on the lens redshift, but also on the halo mass. This is clear in Fig 6.6, which shows the scaling functions measured at different redshifts and for halos of different mass. We see that, at any redshift, the scaling functions for low-mass lenses start to rise at larger z_s compared to lenses with higher mass. They also tend to reach their maxima at significantly higher redshift. This is due to the fact that small lenses are efficient at producing giant arcs only when the sources are distant. Therefore, it is of fundamental importance to evaluate the scaling functions in different mass and redshift bins, as we do here.

By using the scaling functions, we can re-write Eq. 6.4 as

$$N_{l/w}(\vec{p}, \vec{c}, z_l, S) = \sigma_{l/w}(\vec{p}, \vec{c}, z_\mathrm{l}, z_\mathrm{s} = 2) \times \tag{6.8}$$

$$\times \int_{z_l}^{\infty} f_\sigma(M, z_\mathrm{l}, z_\mathrm{s}) n(z_\mathrm{s}, S) \mathrm{d}z_\mathrm{s} \,, \tag{6.9}$$

which allows us to estimate the number of arcs produced by any lens for a given number density of sources just by measuring its cross section at $z_\mathrm{l} = 2$.

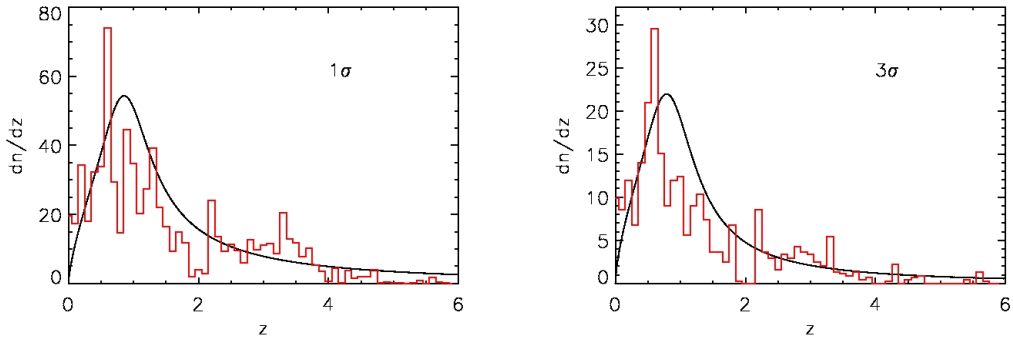

Figure 6.7: Source density distribution as a function of redshift for galaxies detected at 1σ and 3σ above the mean background level. The red histograms show the distributions derived from the analysis of the Euclid simulated observations. The solid lines show the best fit to the distributions using the functional proposed by Fu et al. (2008). Numbers in the y axis are in unit of arcmin^{-2}.

6.2.5 Source Number Density

The last ingredient needed in Eq. 6.9 to be able to compute the number of giant arcs expected from a single lens is the number density of sources as a function of redshift and limiting surface brightness, $n(z_s, S)$.

For deriving the source redshift distribution function, we make use of simulated observations with the `SkyLens` software (Meneghetti et al. 2008, 2010b; Bellagamba et al. 2012; Rasia et al. 2012). This code uses a set of real galaxies decomposed into shapelets (Refregier 2003) to model the source morphologies on a synthetic sky. In particular, we use here 10,000 galaxies in the B, V,i,z bands from the Hubble-Ultra-Deep-Field (HUDF) archive (Beckwith et al. 2006). Most galaxies have spectral classifications and photometric redshifts available (Coe et al. 2006), which are used to generate a population of sources whose luminosity and redshift distributions resemble those of the HUDF. `SkyLens` allows us to mimic observations with a variety of telescopes, both from space and from the ground. For this work, we simulate wide-field observations with the optical camera which will be onboard the Euclid satellite. For setting up these simulations, we stick to the Euclid description (throughput, PSF, telescope size, CCD characteristics, etc.) contained in the Euclid Red-Book (Laureijs et al. 2011). More details on Euclid simulations carried out with the `SkyLens` software can be found in Bellagamba et al. (2012).

We simulate 400" × 400" fields to the depth which will be reached by Euclid ($m_{riz} \sim 24.5$), and we derive the number density and the redshift distribution of all sources detected in the simulated images. To analyze the images, we use the software `SExtractor` (Bertin & Arnouts 1996), which we use also to estimate the background rms. We derive source catalogs imposing different detection thresholds, i.e 1 and 3 times the background rms.

The redshift distributions obtained for these two detection limits are shown by the histograms in Fig. 6.7, where we plot the number density of detected sources as a function of their redshift. We fit these distributions with the functional proposed by Fu

et al. (2008), which has the form

$$n(z) = A\frac{z^a + z^{ab}}{z^b + c} \ , \tag{6.10}$$

with

$$A = \left(\int_0^{+\infty} \frac{z^a + z^{ab}}{z^b + c}\mathrm{d}z\right)^{-1}$$

and a, b, c free parameters. We find that the *observed* distributions are fitted by the functional with bets-fit parameters $(a, b, c) = (0.764, 5.998, 0.751)$ and $(a, b, c) = (0.662, 5.502, 0.633)$ for sources 1σ and 3σ above the mean sky level, respectively. These best fits are shown by the solid lines in Fig. 6.7 from the same figures.

6.2.6 Construction Of The Light-Cones

The procedure outlined above describes how we can calculate the number of arcs with a given l/w ratio produced by a single lens. By investigating all lenses on our (M, z_l) grid, we end up with a list of $\sim 340,000$ cross sections for sources at redshift $z_\mathrm{s} = 2$, which we can transform into cross sections for other source redshifts using the previously defined scaling functions. In particular, for each cell of the grid, we have 100 cross sections of halos with similar mass but different structural properties.

In this section, we explain how we estimate the number of arcs expected in a given area of the sky. To achieve this goal, we obviously need to consider all lenses within the light-cone with vertex on the observer, which subtends the surveyed area. More specifically, aiming at simulating the wide survey which will be operated by Euclid, we construct light-cones subtending an area of 15,000 squared degree. The depth of the light-cones should be such to contain all lenses capable to produce giant arcs. According to the simulations by Meneghetti et al. (2010a), we expect no lenses producing giant arcs from sources at $z_\mathrm{s} = 2$ above $z_\mathrm{l} \sim 1.3$. To be more conservative, given that our simulations use source planes until redshift $z_\mathrm{s} = 6$, we extend the light-cones up to $z_\mathrm{l} = 1.5$. It is worth mentioning, however, that a giant arc has been recently discovered behind the galaxy cluster IDCS J1426.5+3508 at $z = 1.75$ using deep HST/ACS+WFC3 observations (Gonzalez et al. 2012a). On the basis of the arc color, the arc redshift has been constrained to be at $z < 6$, most likely $z \sim 4$. The integrated magnitude in the F814W ACS filter is 24.29 ± 0.31, thus close to the detection limit of Euclid. As we will show later, in our simulations no giant arcs are produced by lenses at $z_\mathrm{l} > 1.3$. Thus, our results confirm the peculiarity of this arc detection, which may have interesting cosmological implications (Gonzalez et al. 2012a).

Once defined the size of the light-cones, we populate them with lenses with different mass and redshift. To do so, we divide the cone into 50 redshift slices, equi-spaced in redshift with $\Delta z = 0.03$. This is the same redshift spacing used to construct the grid (M, z_l) over which the cross sections were evaluated. Thus, we define 50 lens planes, with the first plane at $z = 0.03$ and the last plane placed at redshift 1.5.

We calculate the number of the lenses with a given mass to be placed on each lens plane by using the Sheth & Tormen mass function (Sheth & Tormen 1999). Masses are drawn again in the interval $[10^{13}, 10^{16}]\, h^{-1} M_\odot$. To consider effects of cosmic variance, we produce 128 realizations of the light-cone.

In order to calculate the number of giant arcs expected to be detectable in the surveyed area, for each halo of mass M and redshift z_l, we randomly select one of

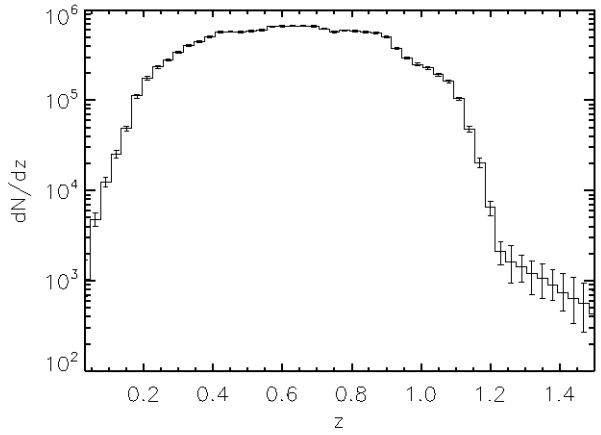

Figure 6.8: Median number of halos as a function of redshift in the 128 realizations of the light cone corresponding to the Euclid wide survey. The error-bars indicate the minimum and maximum number of halos in each redshift bin, again from the 128 light-cone realizations.

		N_{med}	I quartile	III quartile	N_{min}	N_{max}
$l/w \geq 5$	1σ	8912	8839	8991	8623	9308
	3σ	2409	2381	2433	2294	2482
$l/w \geq 7.5$	1σ	2914	2889	2952	2810	3100
	3σ	790	779	800	746	819
$l/w \geq 10$	1σ	1275	1260	1297	1216	1387
	3σ	346	340	352	323	362

Table 6.1: N_{med} is the median number of arcs with $l/w \geq 5$, 7.5, and 10, computed from the results of 128 different $15,000$ deg^2 mock light-cone realizations, from sources 1σ and 3σ upon the mean sky level. In fourth and fifth columns are the 25% and 75% percentiles, while in sixth and seventh columns are the minimum and maximum values.

the 100 cross sections in the corresponding (M, z_l) cell. Then, we assign to the halo the scaling function previously measured for halos with its mass and redshift. We use Eq. 6.9 to compute the number of arcs expected from each lens. The total number of arcs expected in the survey is then calculated as

$$N_{l/w}^{tot} = \sum_{i=1}^{N_{lens}} N_{l/w,i} \, , \tag{6.11}$$

where N_{lens} is the total number of arcs in the light-cone and $N_{l/w,i}$ is the number of arcs produced by the i-th lens.

6.2.7 The Total Number Of Arcs

The total number of arcs expected in the Euclid wide survey on the basis of our simulations is given in Tab. 6.1 for different minimal length-to-width ratios ($l/w_{\rm min} = 5, 7.5, 10$) and for two detection thresholds, namely 1 and 3 times the background rms

These values represent the threshold above the background for which a group of connected pixels are identified by `SExtractor` (Bertin & Arnouts 1996). We report the median number of arcs derived from the 128 realizations of the light-cones (N_{med}), as well as the quartiles of the distributions. To allow for better quantification of the cosmic variance, we also report the minima and the maxima of the distributions.

If we consider the detections above the background rms, the median numbers of arcs with $l/w \geq 5$, 7.5 and 10 are 8912^{+79}_{-73}, 2914^{+38}_{-25} and 1275^{+22}_{-15} respectively. If we consider the detections at higher significance (3 times the background rms) the respective numbers are 2409^{+24}_{-28}, 790^{+10}_{-12} and 346 ± 6. The quoted errors correspond to the inter-quartile ranges of the distributions. We notice that those values are dependent somehow on the source redshift distribution adopted, which is consistent with the simulations performed with the Euclid telescope equipment. A source redshift distribution with a pick shifted 10% below or above our fiducial one produces a total number of arcs which is 20% smaller or larger.

We would like to stress that these arcs will be *potentially* detectable in the future Euclid wide survey. At this stage, we are not considering several practical difficulties which may complicate the recognition of gravitational arcs in real observations. For example, arcs can be easily confused with edge-on spiral galaxies or with other elongated structures on the CCDs. Additionally, arcs form in dense regions of cluster galaxies. Since these are typically very bright and extended, arcs are frequently hidden behind them. Aiming at analyzing huge datasets such as the data that will be delivered by Euclid, it will be particularly important to develop softwares for the automatic detection of gravitational arcs. Few such tools exist already (Alard 2006; Seidel & Bartelmann 2007; Cabanac et al. 2007; More et al. 2012) and have been tested extensively. In a work in progress, we are currently addressing the task of quantifying the degree of contamination and completeness of the arc catalogs delivered from these arc finders through the analysis of simulated images.

Nevertheless, these results indicate that Euclid will be able to detect an unprecedented number of strong lensing features such as giant arcs and arclets. These will represent a treasury for any future study focusing not only on arc statistics but also aiming at using these features to construct and calibrate lens models and to map the mass distribution in galaxy clusters.

6.2.8 Arc production as a function of the lens redshift

It is interesting to study the redshift distribution of the lenses producing giant arcs. This is important to assess which lenses will be better constrained by strong lensing data. Moreover, given its sensitivity to the dynamical evolution of clusters, it is important to understand up to which redshift gravitational arcs can be used to trace cluster evolution.

In Fig. 6.9 we show the number of arcs produced by lenses at different redshifts. We use solid red, dashed orange and long-dashed green lines to display the results for arcs with $l/w \geq 5$, 7.5, and 10, respectively. Shown are the medians of the 128 realizations of the Euclid survey (thick lines) and the corresponding ranges among minimum and maximum values (thin lines). The left and the right panels refer to detections at the levels of 1 and 3 times the background rms

We note that, independently of the minimal l/w ratio, the number of arcs reaches its maximum at redshift ~ 0.6. It drops quickly to zero at redshifts $z \lesssim 0.2$ and $z \gtrsim 1.2$. Such behavior results from a combination of different reasons. First, at low redshift,

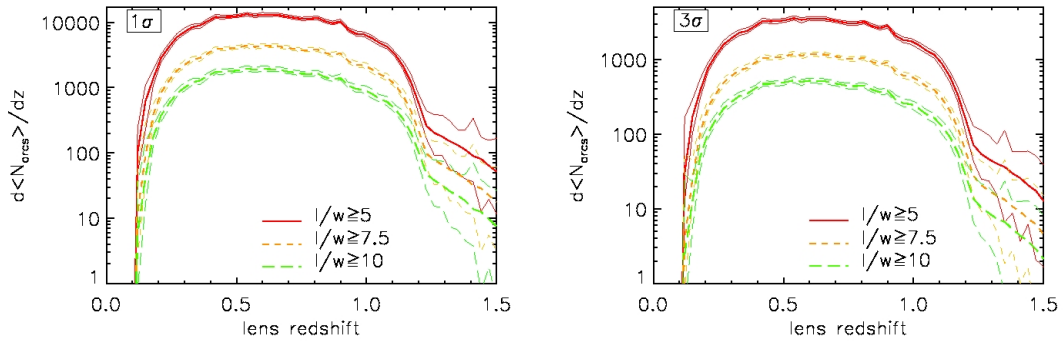

Figure 6.9: Number of arcs as a function of the lens redshift. The thick (thin) lines are the median (quartiles) among the 128 light-cone realizations and they refer to arcs with $l/w \geq 5$ (solid red), 7.5 (dashed orange), and 10 (long-dashed green), respectively. The left and the right panels refer to detections at the level of 1 and 3 times the background rms.

the cosmic volume contained in the light-cone is small, thus a relatively small number of lenses are present at these redshifts. This is clear from Fig. 6.8, which shows that the number of halos drops by almost two orders-of-magnitude between $z = 0.4$ and $z = 0.2$ and by an additional order-of-magnitude between $z = 0.2$ and $z = 0.1$. Second, the lensing cross section of individual halos is small both at low- and at high-redshift, i.e. when the lens is too close to the observer or to the bulk of sources. To illustrate this, we show in Fig. 6.10 the lensing cross section for arcs with $l/w \geq 7.5$ (solid lines) and $l/w \geq 10$ (dashed lines) as a function of redshift for a halo with mass $7 \times 10^{14}\ h^{-1}\ M_{\odot}$. Given the redshift distribution of the sources expected in the Euclid observations, the median source redshift in the case of arcs detectable at the level of 1 and 3 times the background rms are $z_s = z_{s,1\sigma}^{med} = 1.24$ and $z_s = z_{s,3\sigma}^{med} = 1.03$, respectively. In the upper and bottom panels of Fig. 6.10, we use these source redshifts to calculate the cross sections. This explains why the curve in the upper panel reaches its maximum at a slightly larger redshift than the curve in the bottom panel. Third, as the redshift grows, increasingly less massive halos are expected, which implies that the number of gravitational arcs produced by these lenses is substantially lower. Fourth, although high-redshift sources can be more efficiently distorted, their surface brightness is dimmed, and their images are more difficult to detect.

As we can see from Fig. 6.10, the lensing cross sections of each individual halo exhibit several local maxima at different lens redshifts. We remind that `MOKA` produces mock lenses which include substructures whose mass and positions are drawn from recipes calibrated on numerical simulations. In particular, halos may be produced with mass configurations resembling a merging phase. In fact, the bumps in Fig. 6.10 correspond to such events, which are known to boost the lensing cross section and the production of arcs, (Torri et al. 2004) significantly. The same events are responsible for the irregular behavior of the curves in Fig. 6.9.

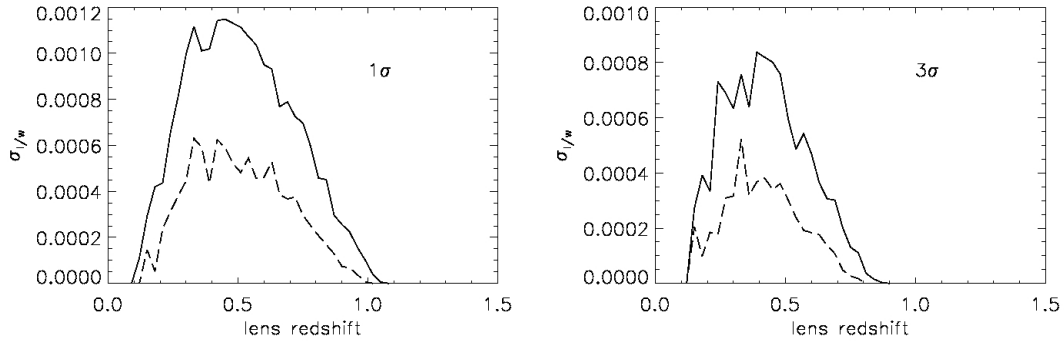

Figure 6.10: Lensing cross section as a function of the lens redshift for a halo with mass $7 \times 10^{14} h^{-1} M_{\odot}$. The upper and the bottom panels refer to detections at the level of 1 and 3 times the background rms, respectively. The solid and the dashed lines indicate the cross sections for arc with $l/w \geq 7.5$ and with $l/w \geq 10$, respectively (cross sections for arcs with $l/w \geq 5$ have a similar behavior).

6.3 Sensitivity To Ω_m And σ_8

In the previous paragraph we illustred the method adopted in Boldrin et al. (2012) to forecast the number of visible arcs in the wide survey be detectable by Euclid. A further step is the analysis of the sensitivity of arc statistics on cosmological parameters. In particular, we study how arc counts are sensitive to the variation of two cosmological parameters: the (total) matter density parameter, Ω_m, and the normalisation of the primordial power spectrum, expressed in terms of σ_8. Both these parameters influence the abundances of collapsed structures and their internal structure. We compute the expected number of gravitational arcs with various length-to-width ratios in mock light cones, by varying these cosmological parameters in the ranges $0.1 \leq \Omega_m \leq 0.5$ and $0.6 \leq \sigma_8 \leq 1$. We find that the arc counts dependence on Ω_m and σ_8 is similar, but not identical, to that of the halo counts. We investigate how the precision of the constraints on the cosmological parameters based on arc counts depends on the survey area. We find that the constraining power of arc statistics degrades critically only for surveys covering an area smaller than 10% of the whole sky. Finally, we consider the case in which the search for arcs is done only in frames where galaxy clusters have been previously identified. Adopting the selection function for galaxy clusters expected to be detected from photometric data in future wide surveys, we find that less than 10% of the arcs will be missed, with only a small degradation of the corresponding cosmological constraints.

6.3.1 Number Of Arcs As A Function Of Redshift

For each combination of cosmological parameters, we produce a catalog of cluster-sized lenses with different masses and redshifts, as described in Section 6.2.6. In order to minimize the computational time, we define 8 redshift bins, having $\Delta z = 0.03$ and centered at redshifts 0.21, 0.36, 0.54, 0.6, 0.84, 1.02, 1.14, and 1.26. The choice of such redshift bins is optimised for the expected redshift distribution of the lenses producing giant arcs, which we derived in Boldrin et al. (2012) for a Euclid-like survey. For each

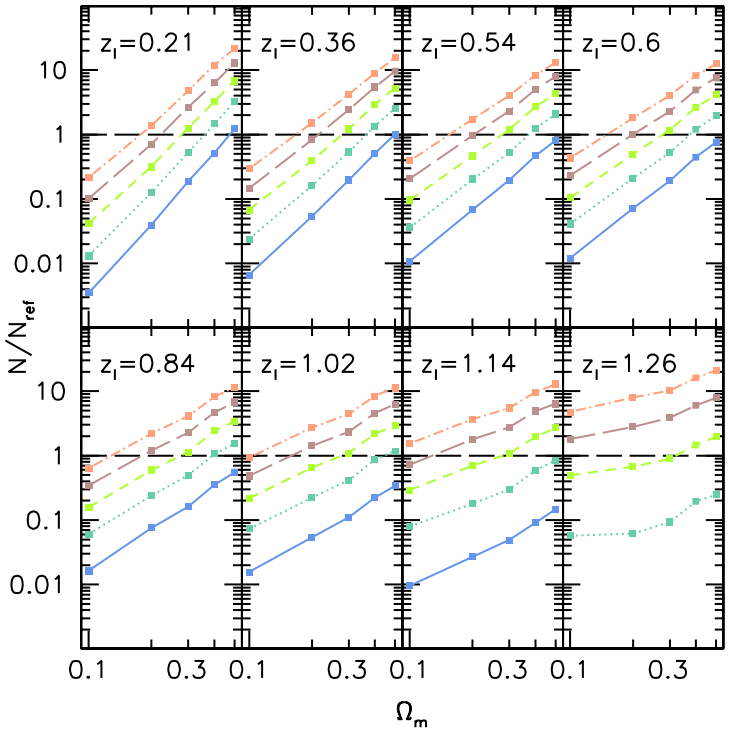

Figure 6.11: Number of arcs (normalised to the reference WMAP7 cosmology) as function of Ω_m and for different values of σ_8. Different panels refer to different redshift bins between $z = 0.21$ and $z = 1.26$, as labeled. The reported counts represent the median of 128 different light-cone realisations for each combination of the cosmological parameters. Solid blue, dotted cyan, dashed green, long-dashed brown and dot-dashed dark orange lines indicate the results for $\sigma_8 = 0.6$, 0.7, 0.8, 0.9 and 1, respectively. The results refer to arcs with $l/w \geq 10$ and sources 1σ above the mean background noise level.

combination of redshift and mass we use `MOKA` to generate 100 halos with different structural properties and measure their $\sigma_{l/w}$, from which we can derive the number of giant arcs they produce, as discussed above.

The catalog of lenses is then used to generate 128 realisations of lens distributions (light-cones) for every above mentioned redshift bin. In each light-cone, which subtends an area of 15,000 square degrees, we calculate the number of lenses of mass M and redshift z_l according to the Sheth & Tormen (1999) mass function, and estimate the total number of arcs by summing up the contributions from each individual lens. Finally, we combine the different light-cones to measure the median number of arcs per square degree and the relative scatter as a function of the considered cosmological parameters.

In Fig. 6.11 we show the number of arcs, normalized to the reference WMAP7 cosmology, as function of Ω_m. The different panels refer to the eight redshifts where the calculations were performed. Different colors and line styles are used to display the results for several values of σ_8: solid blue, dotted cyan, dashed green, long-dashed brown and dot-dashed dark orange lines refer to σ_8=0.6, 0.7, 0.8, 0.9 and 1, respectively. Long-dashed black horizontal lines correspond to unity, i.e. to the reference cosmology.

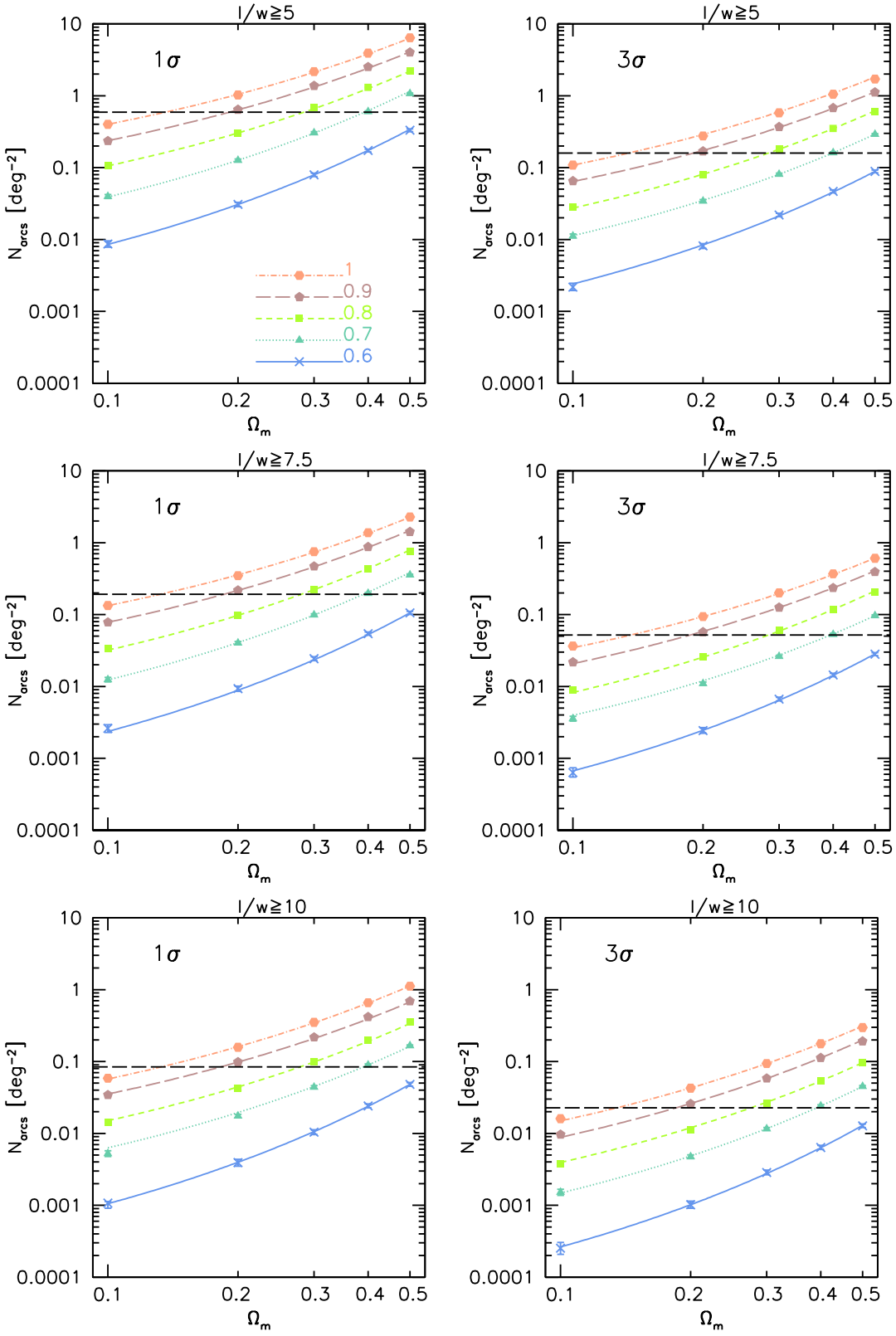

Figure 6.12: Number density of arcs as a function of Ω_m for different values of σ_8. The right and left columns refer to sources detectable at 1σ and 3σ above the mean background noise level, respectively. From top to bottom, the different panels show the results for three choices of minimum l/w, namely 5, 7.5 and 10. Line and color styles are as in Fig. 6.11. In each panel the horizontal dashed line shows the counts in the considered reference model.

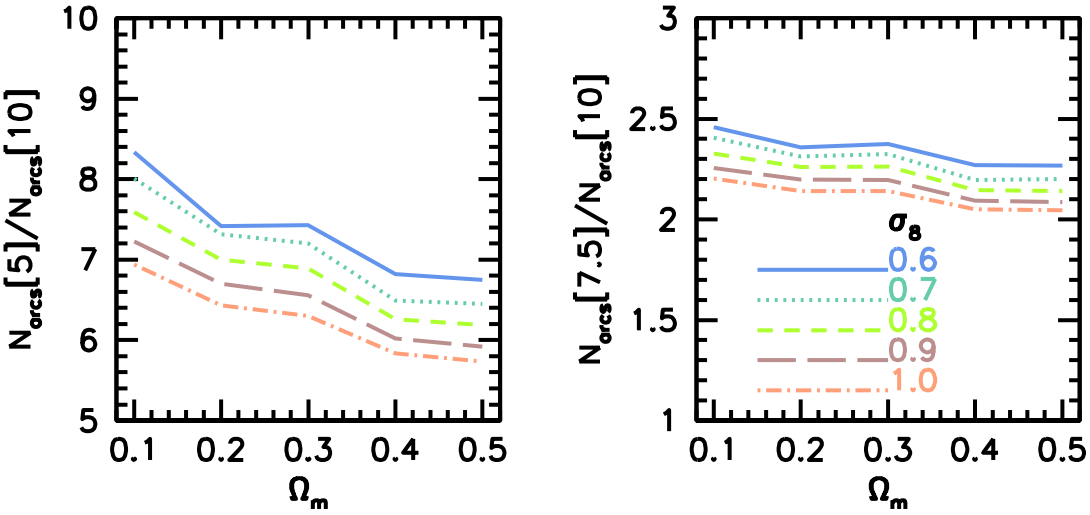

Figure 6.13: The abundances of arcs with $l/w \geq 5$ (left panel) and $l/w \geq 7.5$ (right panel) relative to the abundances of arcs with $l/w \geq 10$ as a function of Ω_m. Line and color styles are as in Fig. 6.11. The results refer to arcs detectable at 1σ above the mean background level.

The lack of a blue solid line in the last panel is due to the inefficiency of clusters at $z_l = 1.26$ to produce giant arcs in the cosmology with $\sigma_8 = 0.6$. As expected, at all redshifts, the arc counts grow as a function of Ω_m and as a function of σ_8, indicating that the abundance of giant gravitational arcs is higher in cosmological models with more matter and higher normalisation of the power spectrum of the primordial density fluctuations.

We also notice that the change of arc counts as a function of cosmology depends on the lens redshift. The dependence on Ω_m is stronger at lower redshift, and flattens off as z_l increases. On the contrary, it appears that the value of σ_8 affects the results more significantly at high redshift.

While the results in Fig. 6.11 refer to arcs with $l/w \geq 10$ and sources above the 1σ background level, the trends remain similar for other l/w ratios and detection limits.

6.3.2 The Total Number Of Arcs In The Light Cone

From the distributions obtained from the 128 different light-cone realizations, we measure the median number of arcs per square degree expected in each cosmological model. This has been done by performing a spline interpolation through the above-mentioned 8 redshifts up to a maximum lens redshift of $z_l = 1.5$.

In the reference WMAP7 cosmology, the expected number densities of arcs per square degree with $l/w \geq 5$, 7.5, and 10 are 0.594±0.016, 0.194±0.006, and 0.085±0.003, respectively. These are in excellent agreement with our estimates reported in Boldrin et al. (2012), although these were obtained using a larger number of redshift bins and avoiding the interpolation.

In Fig. 6.12, we show the median arc number counts per square degree as a function

		C	D	E	F
$l/w \geq 5$	1σ	0.424	0.746	-3.118	1.587
	3σ	0.437	0.731	-3.975	0.952
$l/w \geq 7.5$	1σ	0.375	0.831	-3.073	0.998
	3σ	0.418	0.778	-3.181	0.562
$l/w \geq 10$	1σ	0.381	0.853	-3.160	0.700
	3σ	0.423	0.798	-3.281	0.285

Table 6.2: Best fit parameters for equations (6.13) and (6.14), indicating the number of arcs in function of Ω_m, σ_8, l/w and the minimum deviation between the source brightness and the mean sky level.

of Ω_m. We also show how the counts vary by changing the value of σ_8, using the same color and line styles used in Fig. 6.11. From top to bottom, we show the results for $l/w \geq 5$, 7.5, and 10, respectively. The left and the right panels refer to detections at 1- and 3σ above the level of the background. Obviously, the results show the same dependence on Ω_m and σ_8 reported in Fig. 6.11.

We also see that the ratios between counts of arcs with different l/w depend on the cosmological parameters. As shown in Fig. 6.13, for low Ω_m, the abundance of arcs with $l/w \geq 5$ or $l/w \geq 7.5$, relative to that of arcs with $l/w \geq 10$, is higher, indicating that halos in these cosmological models have smaller critical lines and are thus less efficient at producing large distortions. The ratios also depend on σ_8; in cosmologies with higher σ_8 halos are able to produce a higher abundance of arcs with large l/w. The results (here shown only for sources 1σ above the mean background level) are insensitive to the assumed detection limit. Therefore, in the following discussion we will show the results only for arcs detectable at the 1σ level. We will also focus on arcs with $l/w \geq 10$.

We were able to find an analytical form for density of arcs $N_{arcs}(\Omega_m, \sigma_8, l/w, \sigma)$ deg^{-2}. The curves that link data points in Fig. 6.12 have the following form:

$$\log[N_{arcs}(\Omega_m, \sigma_8, l/w, S_{min})\,\mathrm{deg}^{-2}] = A(\sigma_8, l/w, S_{min})\Omega_m^{1/\ln 10} + B(\sigma_8, l/w, S_{min}), \tag{6.12}$$

where A and B are given by

$$A(\sigma_8, l/w, S_{min}) = \exp\left(\frac{C(l/w, S_{min})}{\sigma_8} + D(l/w, S_{min})\right) \tag{6.13}$$

and

$$B(\sigma_8, l/w, S_{min}) = \frac{E(l/w, S_{min})}{\sigma_8} + F(l/w, S_{min}). \tag{6.14}$$

Parameters C, D, E and F depend on the values of l/w (5, 7.5 or 10) and S_{min}, the minimum considered source brightness w.r.t. the mean sky level (1σ or 3σ). Best fit values for C, D, E and F are shown in Table 6.2.

The upper panel in Fig. 6.14 shows the difference in the arc counts relative to the reference WMAP7 cosmology in the $\Omega_m - \sigma_8$ plane. Within the ranges explored in this work, we may find differences of up to one order of magnitude for the predicted arc counts between cosmological models. We also notice that the cosmological parameters Ω_m and σ_8 are degenerate with respect to the arc counts. Indeed, the same number of arcs is expected in cosmologies whose combination of Ω_m and σ_8 lays in a banana-like region extending from the upper left to the bottom right corner of the plane. The origin

of this degeneracy will be better discussed in Section 6.3.3. Interestingly, a Planck-like cosmology with $\Omega_m = 0.3086$ and $\sigma_8 = 0.8288$ (Planck Collaboration et al. 2013) produces 54% more arcs than the reference WMAP7 cosmology.

We find that in the case of the reference WMAP7 model, the equation describing

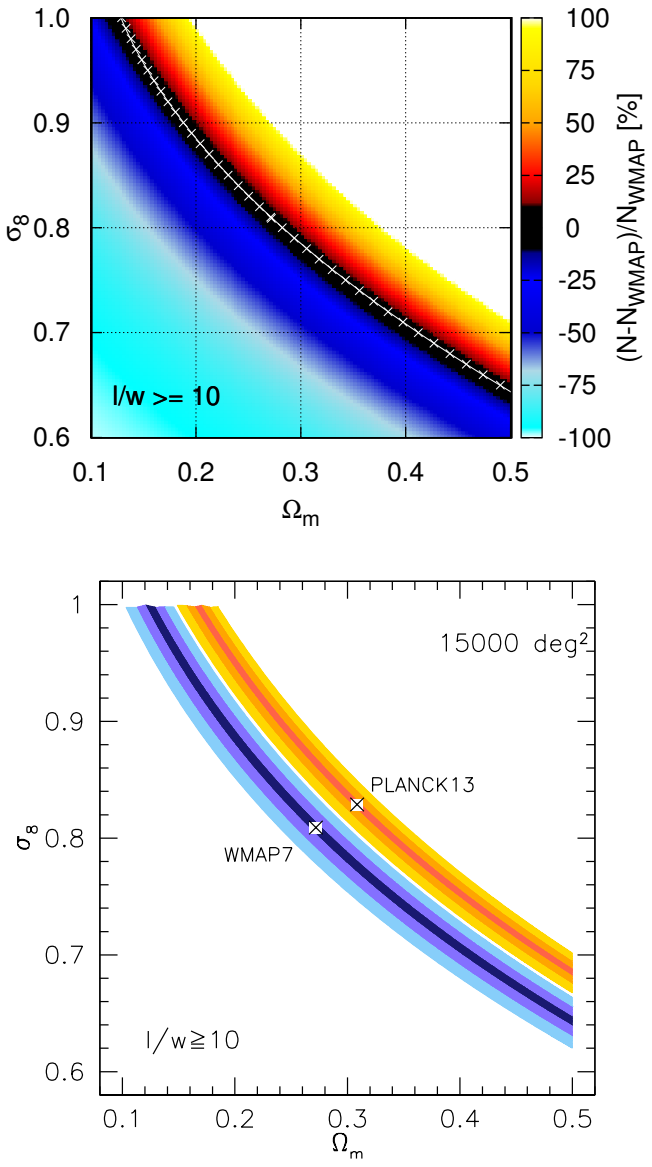

Figure 6.14: *Upper panel:* difference in the arc counts with respect to the reference WMAP7 cosmology in the $\Omega_m - \sigma_8$ plane. The results are shown for arcs with $l/w \geq 10$ detectable at 1σ above the background level. The white crosses represent the cosmological models having the same arc counts as the reference WMAP7 model [relation (6.15)]. *Bottom panel:* levels corresponding to 1, 3, and 5σ deviations (from dark to light colors) from the WMAP7 (blue) and the Planck (yellow) cosmologies in the $\Omega_m - \sigma_8$ plane, assuming a 15,000 deg^2 survey to the expected depth of the Euclid wide survey. The crosses indicate the position of the two reference models.

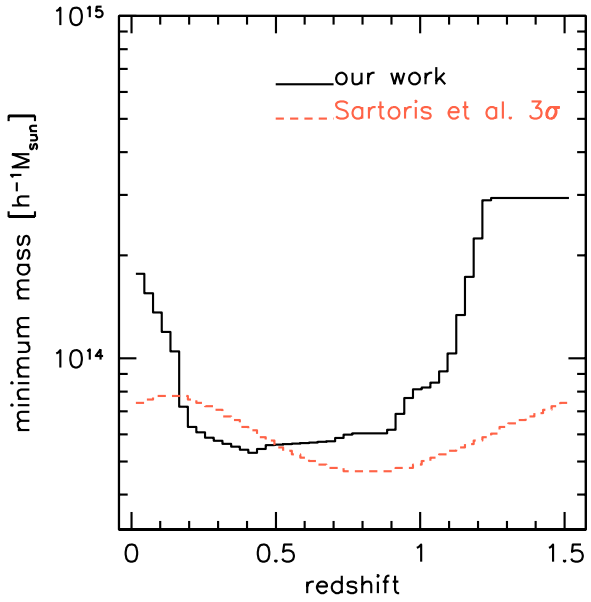

Figure 6.15: The strong lensing selection function (black solid curve), i.e. the minimum galaxy cluster mass expected to produce critical lines for sources located at $z_s = 2$ (Meneghetti et al. 2010a; Boldrin et al. 2012). For comparison, the red dashed curve represents the minimum mass of galaxy clusters which are expected to be detected above three times the rms of the field galaxy counts in the Euclid photometric survey (Sartoris et al. 2016).

the degeneracy curve between the cosmological parameters has the following form:

$$\Omega_m = A\sigma_8^2 + B\sigma_8 + C, \tag{6.15}$$

where $A = 1.771$, $B = -3.952$ and $C = 2.31$. Such function is given by the white line in the upper panel of Fig. 6.14.

In the attempt to quantify the uncertainty in the arc counts, we define the 1σ uncertainty on the number counts as $\sigma \equiv (\sigma_{CV}^2 + \sigma_P^2)^{1/2}$, where σ_{CV} is the cosmic variance, which is estimated from the 16th and 84th percentiles of the distributions derived from the 128 light-cone realisations of each tested cosmological model. The other term appearing in the equation, $\sigma_P \equiv \sqrt{N}$, is the associated Poisson noise on the number counts.

In the bottom panel of Fig. 6.14, we perform an error analysis showing the levels corresponding to 1, 3, and 5 σ deviations (from dark to light colors) from the WMAP7 and the Planck cosmologies in the $\Omega_m - \sigma_8$ plane. The results were obtained assuming a survey covering 15,000 sq. degrees of the sky to the depth expected for the Euclid mission. It is interesting to notice that a survey with the Euclid characteristics will be able to distinguish these two cosmological models at more than 5σ level.

6.3.3 Influence Of The Cosmological Parameters On Arc Statistics

In this section we will discuss in more detail some aspects of the influence of Ω_m and σ_8 on arc statistics. In general, the cosmological parameters play an important role in arc statistics through the lens mass function and their strong lensing cross section, the

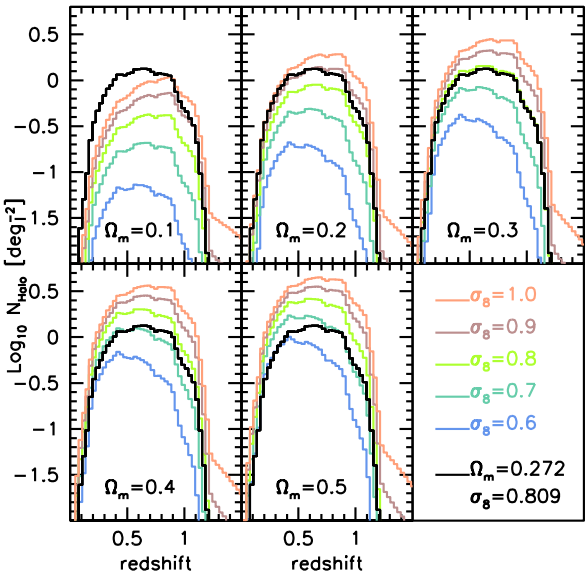

Figure 6.16: Number density of expected strong lenses as a function of redshift, for cosmologies with different Ω_m and σ_8. Plots from left to right and from up to bottom refer to increasing values of Ω_m. Different colors represent counts for various values of σ_8, as labeled on the bottom right. The black line shown in all panels represents the results for the reference WMAP7 model.

latter depending on the geometry of the Universe and on the structural properties of the lens halo.

In particular, the number of arcs is directly related to the number of lenses able to produce arcs. Following Meneghetti et al. (2010a, 2011), this can be estimated including in the mass function describing the lens distribution a sharp cut at the minimum mass corresponding to the smallest systems in which we expect to find critical lines for sources at $z_s = 2$. The shape of the adopted selection function as a function of redshift is shown by the black curve in Fig. 6.15 (see also Boldrin et al. 2012).

In Fig. 6.16, we present the number density (given per square degree) of the lenses as a function of redshift. In each panel, we keep fixed Ω_m as labeled and we vary the value for σ_8, using the color code indicated on the bottom right. To facilitate the comparison, the lens number density in the reference WMAP7 cosmology is shown in black in all panels. From the figure, the strong effect of the different matter density on the lens abundances and the anticipated structure formation originated by a higher power spectrum normalization are clear.

In Fig. 6.17, adopting the same color code as in the upper panel of Fig. 6.14, we show the difference in the lens counts relative to the reference WMAP7 cosmology in the $\Omega_m - \sigma_8$ plane. The white solid curve in the figure represents the degeneracy between Ω_m and σ_8 for the halo counts, for which we find the following relation:

$$\sigma_8(\Omega_m/0.272)^{0.304} = 0.809\,. \tag{6.16}$$

Even if with some differences, this curve is close to the relation (shown by the white crosses) representing the degeneracy we found in the $\Omega_m - \sigma_8$ plane for the arc counts (see also Fig. 6.14): this is clearly due to the fact that the most important ingredient

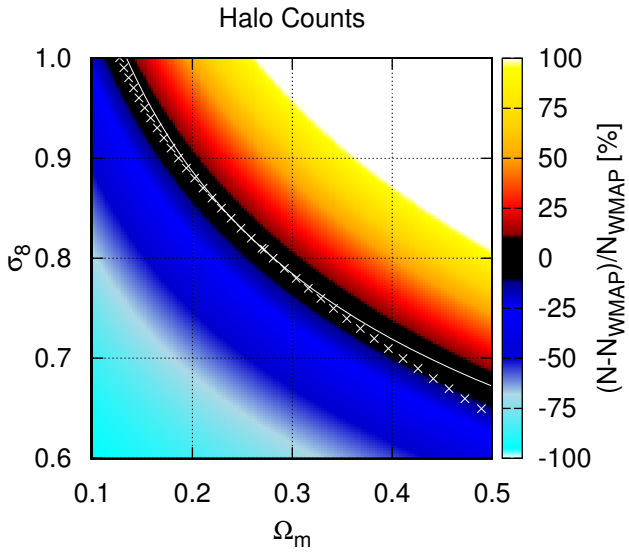

Figure 6.17: Relative difference of halo counts on the σ_8-Ω_m plane with respect to the reference WMAP7 model. The white crosses represent the degeneration curve relative to the arc counts, while the white solid line refers to the degeneracy curve for halo counts.

for arc statistics is the lens mass function. However, if one compares the amplitude of the count variation by looking at the width of the coloured strips, it is evident that the arc density is more sensitive to the cosmological parameters than the simple

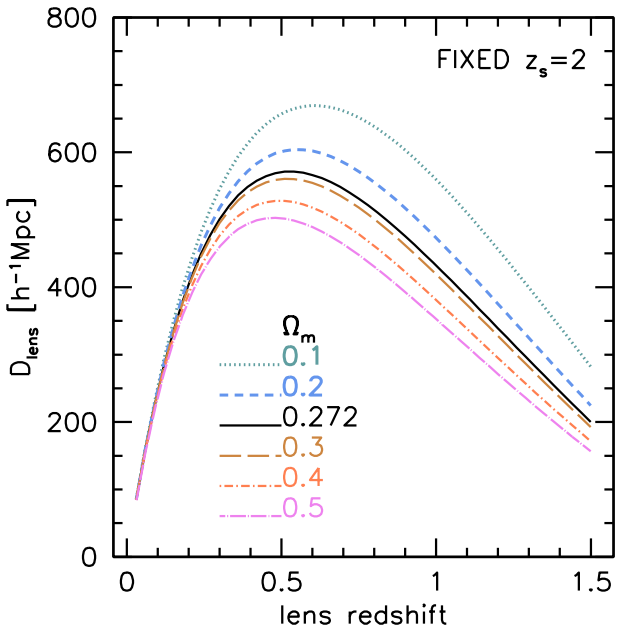

Figure 6.18: Lensing distance for different values of Ω_m. Sources are kept fixed at redshift $z_s = 2$.

halo density: consequently, a wide survey of gravitational arcs could potentially give significant constraints.

The larger sensitivity of arc statistics is due to the cosmological dependence of the other main ingredients, such as the angular diameter distances of lenses and sources and the lens structural properties. We know that the first condition for an axially symmetric lens to act like a strong lens is that in some points $\vec{x}$ on the lens plane the condition

$$\kappa(\vec{x}) > 1 \tag{6.17}$$

occurs, where $\kappa \equiv \Sigma(\vec{x})/\Sigma_{cr}$ is the so-called convergence, $\Sigma(\vec{x})$ is the lens projected mass density and

$$\Sigma_{cr} \equiv \frac{c^2}{4\pi G} D_{lens}^{-1} \tag{6.18}$$

represents the critical value of the two-dimensional mass density in order to have strong lensing effects. The quantity D_{lens} is the so-called *lensing distance*, defined as

$$D_{lens} \equiv \frac{D_{LS} D_L}{D_S}\,, \tag{6.19}$$

where D_S, D_L and D_{LS} are the angular diameter distances of the source, of the lens and between source and lens, respectively. Although for elliptical lenses we have to add the effect of shear to the condition (6.17), we can infer, to first approximation, what are the system configurations which are more efficient in producing strong lensing features by investigating how D_{lens} changes in the different cosmological models, once the lens properties and the source redshifts are kept fixed. We remind the reader that D_{lens} contains the full dependence on the geometry of the system and does not depend on σ_8, but only on Ω_m. We fix the source position at redshift $z_s = 2$ and we study $D_{lens}(z_l)$, that is we keep fixed the length of the lensing system and we move the lens from the observer towards the source plane. The results are shown in Fig. 6.18: we see that increasing the value of Ω_m, the strong lensing efficiency reaches its maximum at lower lens redshifts. In particular the peak around which the production of gravitational arcs is expected to be boosted shifts from $z \approx 0.6$ to $z \approx 0.4$ when the value of Ω_m is increased from 0.1 to 0.5.

The effect of the anticipation of structure formation due to a higher value of σ_8 (Giocoli et al. 2007, 2012b) has consequences on several halo structural properties that may influence the size of $\sigma_{l/w}$. Considering the concentration parameter, at fixed σ_8, large Ω_m values lead to larger concentrations because the structures form and grow in denser environments. At the same time, keeping fixed the value of Ω_m, in cosmologies with high σ_8 the concentration increases because of both the higher contrast between primordial perturbations and background, and the anticipated formation time (Neto et al. 2007; Giocoli et al. 2012b; Macciò et al. 2008).

Haloes triaxiality is also an important feature that depends on cosmological parameters (Despali et al. 2014; Bonamigo et al. 2015). In particular, the level of sphericity of a halo, which is directly related to the ratio between its minor and major semi-axes a/c, is an increasing function of σ_8 and a decreasing function of Ω_m. As an example, if we consider haloes with a mass equal to $7.5 \times 10^{14}\ h^{-1}\mathrm{M}_\odot$ at redshift $z = 0.54$ in a cosmological model with $\Omega_m = 0.3$, the median ratio among 128 realizations varies from $a/c = 0.353^{+0.049}_{-0.056}$ in a model with $\sigma_8 = 0.6$, to $a/c = 0.417^{+0.057}_{-0.066}$ in a model with $\sigma_8 = 1.0$. The quoted uncertaintes correspond to 1σ errors. On the other hand, if we fix $\sigma_8 = 0.8$, the ratio changes from $a/c = 0.419^{+0.058}_{-0.066}$ in a model with $\Omega_m = 0.1$, to $a/c = 0.388^{+0.053}_{-0.061}$ in a model with $\Omega_m = 0.5$.

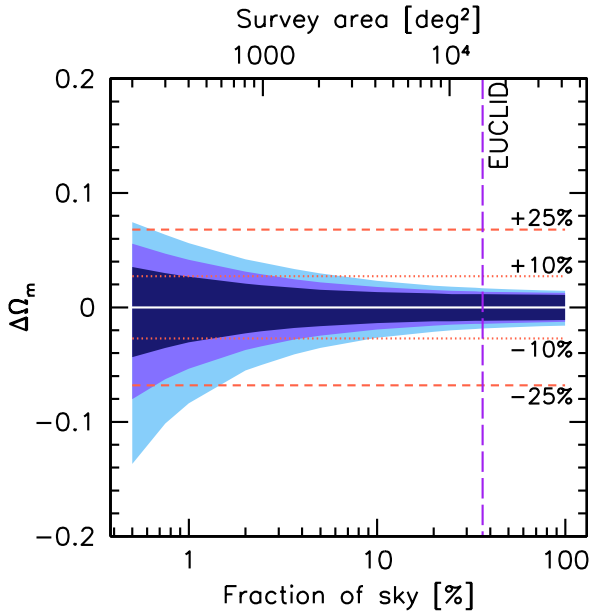

Figure 6.19: The amplitude of the 3σ error bar on Ω_m as a function of the survey area. The vertical dashed line shows the size of the future Euclid wide survey. The red horizontal dotted and dashed lines represent a variation of Ω_m corresponding to $\pm 10\%$ and $\pm 25\%$, respectively.

6.3.4 Effects Of Completeness And Cluster Selection Function

In the following subsections we will discuss how our results change when we take into account the lack of completeness and when we introduce a realistic photometric galaxy cluster selection function.

The effect of sample completeness and survey area

Let us consider here the case in which a fraction of arcs are missed, independently of the properties of the lens configurations (l/w, z_l, z_s). This may happen because some arcs may escape detection for some particular configurations of the light distribution within the cluster, or when the separation between cluster and foreground galaxies is made difficult by the lack of precise color information. The total arc counts may also diminish because we are performing our search in a reduced effective area, smaller than the one of the running survey. In this situation losing 10% of the counts is equivalent to observe a portion of sky 10% smaller than the original survey. The obvious consequence of a reduction of the number of observed arcs is that the Poissonian uncertainty grows and can start to dominate with respect to the cosmic variance, when accounting for the total error budget. To quantify this effect, in Fig. 6.19 we show, as a function of the fraction of the sky covered by the arc search, the variation of the 3σ error bar on the parameter Ω_m, when the value of σ_8 is a priori fixed to its reference value ($\sigma_8 = 0.809$), as it may happen if independently measured from other cosmological probes. Dark, medium and light blue regions refer to the cases of arcs with $l/w \geq 5$, 7.5 and 10, respectively, while the horizontal dotted (dashed) lines indicate an accuracy of 10 (25) per cent on Ω_m. From the figure it is clear that arcs with $l/w \geq 5$, being more numerous, give

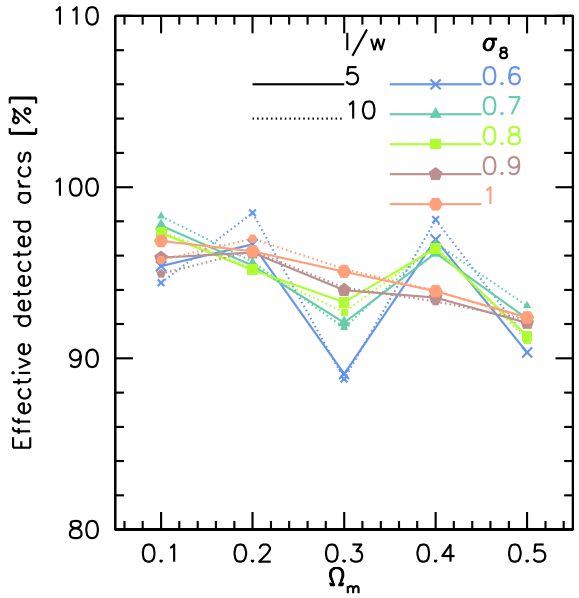

Figure 6.20: Percentage of arcs effectively detected by considering only lenses having a mass larger than the Euclid cluster photometric selection function. Different color refer to different values of σ_8, as labeled; solid and dotted lines are for arcs with $l/w \geq 5$ and 10.

stronger contraints and are less affected by possible incompleteness problems. However, there is a difficulty when dealing with them because they can look like simple edge-on galaxies. For this reason the loss and misidentification of arcs are expected to depend on l/w, being stronger for low-l/w ratios. From this point of view, Fig. 6.19 is quite encouraging: if the survey area is sufficiently wide (larger than 10% of the whole sky), or equivalently if the arc finders are sufficiently efficient, the error budget is dominated by cosmic variance and there is not a significant difference in the constraining power between using arcs with $l/w \geq 5$ or with $l/w \geq 10$. We remind that the SDSS (York et al. 2000) has an area of about 10,000 deg^2, while the Euclid wide survey is expected to cover 15,000 deg^2 (Laureijs et al. 2011).

The Effect Of The Cluster Selection Function

Due to the high computational cost of the algorithms for arc detection, a possible strategy in future wide surveys is to run these codes only on small-size frames where galaxy clusters have been previously identified. Obviously, this originates a reduction of the effective number of arcs, which is strongly dependent on the specific cluster selection function of the survey.

As a worked example, here we consider again the future ESA Euclid mission. Given the amount and quality of its data covering an area of 15,000 deg^2, there will be at least three main ways to identify galaxy clusters: (i) from photometric data, (ii) from spectroscopic data, and (iii) from cosmic shear maps. As shown in Sartoris et al. (2016) , the one based on photometric data (see, for example, Bellagamba et al. 2011, and references therein) is expected to be largely the most efficient one. In this case, the minimum mass of galaxy clusters having a number of members larger than 3 times

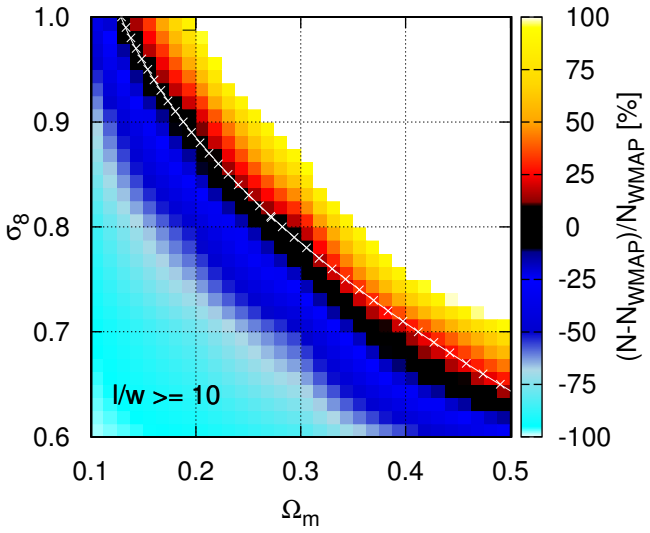

Figure 6.21: As the upper plot of Fig. 6.14, but for arcs produced by lenses having a mass larger than the Euclid cluster photometric selection function (Sartoris et al. 2016). The crossed line represents the degeneracy curve obtained when no selection function is applied.

the r.m.s. of the field galaxy counts is expected to be between $5 \times 10^{13}\, M_{\odot}/h$ and $8 \times 10^{13}\, M_{\odot}/h$ in the redshift range here considered (Sartoris et al. 2016). Compared to the minimum mass needed to produce critical lines for sources located at redshift $z_s = 2$ (see Fig. 6.15), the Euclid cluster selection is then slighly higher on a limited redshift range only, namely between $z = 0.2$ and $z = 0.5$. This means that limiting the search for arcs to frames where galaxy clusters have been already identified is expected to not reduce dramatically the number of detected arcs. This is confirmed in Fig. 6.20, where we show the fraction of arcs that can be effectively detected following this strategy. Same colors indicate same values of σ_8, as labeled in the figure, while solid and dotted lines refer to arcs with $l/w \geq 5$ and 10, respectively. For the cosmological models here considered, the reduction varies between 2 and 10 per cent and is almost independent of l/w. For the reference WMAP7 model, the percentage of effectively detected arcs remains about 95 per cent.

In Fig. 6.21 we show the relative differences in the arc counts between each cosmological model and the reference WMAP7 cosmology, considering only arcs produced by galaxy clusters above the Euclid photometric selection function. In the figure, the color scale is identical to that adopted in the upper panel of Fig. 6.14. The white crosses represent the degeneration curve we found considering the total number of arcs, i.e. without applying the cluster selection function. Although similar, the curve changes in a non negligible way, especially considering extreme values of the parameters. This underlines the importance of taking into account every kind of selection function when combining theory and observations in arc statistic studies, avoiding possible systematics.

The presence of strong lensing features like arcs can represent a complementary way to confirm the presence of a galaxy cluster. Moreover arcs can be used to improve the estimates of the mass of galaxy clusters, a fundamental ingredient to fully exploit the evolution of their abundance as cosmological probe. For this reason it is important to

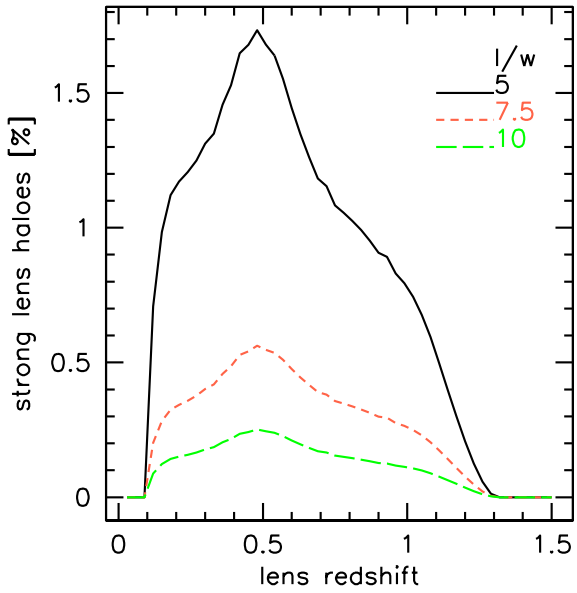

Figure 6.22: Fraction of galaxy clusters having a mass larger than the Euclid cluster photometric selection function producing at least one giant arc. Results are shown for the reference WMAP7 model. Different line styles refer to different length-to-width ratios, as labeled.

compute what is the fraction of the galaxy clusters identified in the Euclid photometric survey, which are able to produce at least one giant arc. The result for the reference WMAP7 cosmology as a function of redshift is shown in Fig. 6.22 for arcs with $l/w \geq 5$, 7.5 and 10 (black solid, red dashed and green long-dashed lines, respectively). Typical mean values are around 1 per cent, 0.33 per cent and 0.15 per cent for $l/w \geq 5$, 7.5 and 10, respectively. From the figure we notice that the strong lens fraction peaks around $z = 0.5$: this behaviour is a combined effect between the well of the photometric selection function around redshift $z = 0.75$ and the peak – around the same redshifts – of the strong lens counts. Interestingly, for redshift $z \geq 1.3$ the percentage tends to vanish. Finally we notice that the fact that the strong lensing selection function can be smaller than the photometric cluster one would allow in principle to add extra objects to the Euclid cluster sample by looking for strong lensing features only. However this would require to run the algorithms for arc detection blindly in different areas of the survey. Considering the reference WMAP7 model and arcs with $l/w \geq 5$, the gain would correspond to approximately 300 extra objects only, all having a relatively low redshift ($0.2 \leq z \leq 0.5$).

Therefore, we can conclude that arc statistics represents a complementary tool to identify galaxy clusters or eventually to prove their presence. In particular, arcs with a small l/w ratio are the best tracers, since they are more numerous, but, at the same time, they are the more difficult to identify because of their similarity with non-lensed galaxies. Finally, our results underline that the codes for arc identification can be run on single frames where galaxy clusters have been already detected with no consequences on the cosmological predictive power of arc statistics.

6.3.5 A Test-Bed For The Method: The CLASH Survey

While this paper focuses on the sensitivity of arc statistics to cosmological parameters like Ω_m and σ_8, it is worth mentioning that another paper has been recently submitted by our collaborators Xu et al. (2015) to compare theoretical predictions of arc abundances in a ΛCDM cosmological model and observations. More precisely, in this other work MOKA has been used to build up halos reproducing the properties of the X-ray selected galaxy clusters belonging to the CLASH sample (Postman et al. 2012). Numerical hydro-dynamical simulations tailored to reproduce the CLASH selection function (Meneghetti et al. 2014) are also used to derive theoretical predictions. Thus, the work of Xu et al. (2015) provides the best opportunity for validating our methodology against more complex models of the cluster mass distribution and against observed clusters with a known selection function.

The results of this study show that there is an excellent agreement between expectations based on MOKA halos and numerical simulations and the arc counts in the CLASH clusters. More specifically, the lensing efficiency measured in the CLASH sample is 4 ± 1 arcs (with $l > 6$" and $l/w > 7$) per cluster. MOKA simulations return exactly the same number (4 ± 1), while numerical simulations give 3 ± 1 arcs per cluster. Therefore, according to Xu et al. (2015), in terms of efficiency to produce long and thin arcs, observations and simulations based on MOKA and numerical hydro-dynamical techniques come into full agreement. It is particularly significant that the methodology we have developed for modeling cluster lenses for arc-statistics calculations is fully capturing the complexity of numerically simulated halos, as evinced from the fact that the cross sections for giant arcs of MOKA generated halos are well matching those of the halos described in Meneghetti et al. (2014).

6.3.6 Conclusions

In this work we have investigated how the number of gravitational arcs depends on cosmology, focusing our attention on the (total) matter density parameter Ω_m and on the initial normalisation power spectrum parameter σ_8. In more detail we have considered the ranges $\Omega_m = [0.1 - 0.5]$ and $\sigma_8 = [0.6 - 1.0]$. Our main results can be summarised as follows.

- We confirm that arc statistics is very sensitive to the couple of parameters $\Omega_m - \sigma_8$. In particular we find that the expected number of arcs is an increasing function of both parameters: this is mostly due to the fact that increasing these parameters boosts the number of lenses.

- The efficiency in producing arcs in cosmologies with high values of σ_8 is larger, since it has an effect also on the structure formation time, that in turn affects some lens structural properties (mainly concentration and triaxiality) relevant for strong lensing.

- A strong degeneracy exists between the two considered cosmological parameters for the number of arcs N_{arcs}; for the reference WMAP7 model this is expressed by the relation (6.15), that is similar, but not equal, in shape to the degeneracy derived from galaxy cluster counts (see eq. 6.16). The differences between the two arise from the non negligible contribution to $\sigma_{l/w}$ given by the lens structural

properties – triaxiality, asymmetries, concentration, substructures and the BCG – and the lensing distance relation.

- Arcs with small l/w ratio are more suitable to constrain cosmological parameters, since they are more numerous. On the other hand, they could be more difficultly identified in the surveys because of their similarity with non-lensed galaxies. We find that if the survey area is sufficiently larger (more than 10% of the full sky) the error budget is dominated by cosmic variance, and the constraining power of arc counts becomes almost independent of the value of l/w. In particular a survey covering 15,000 deg^2 will be able to distinguish at more than 5σ level the two cosmological models supported by WMAP7 and Planck CMB data.

- Considering future wide surveys, like the ESA Euclid mission, we find that searching for arcs only in frames where galaxy clusters have been previously detected will produce a loss of 2-10% of arcs only (depending on the cosmological model) and a consequent limited degradation of the constraining power of arc counts. This suggests that it will be not necessary to run the computationally expensive algorithms for arc detection on whole wide surveys.

List of Figures

List of Tables

Bibliography

Alard, C. 2006, ArXiv Astrophysics e-prints

Bartelmann, M., Huss, A., Colberg, J. M., Jenkins, A., & Pearce, F. R. 1998, A&A, 330, 1

Bartelmann, M. & Schneider, P. 2001, Physics Report, 340, 291

Bartelmann, M., Steinmetz, M., & Weiss, A. 1995, A&A, 297, 1

Beckwith, S. V. W., Stiavelli, M., Koekemoer, A. M., et al. 2006, AJ, 132, 1729

Bellagamba, F., Maturi, M., Hamana, T., et al. 2011, VizieR Online Data Catalog, 741, 31145

Bellagamba, F., Meneghetti, M., Moscardini, L., & Bolzonella, M. 2012, MNRAS, 422, 553

Bertin, E. & Arnouts, S. 1996, A&AS, 117, 393

Blumenthal, G. R., Faber, S. M., Flores, R., & Primack, J. R. 1986, ApJ, 301, 27

Boldrin, M., Giocoli, C., Meneghetti, M., & Moscardini, L. 2012, MNRAS, 427, 3134

Bolton, A. S., Burles, S., Koopmans, L. V. E., et al. 2008, ApJ, 682, 964

Bonamigo, M., Despali, G., Limousin, M., et al. 2014, ArXiv e-prints

Bonamigo, M., Despali, G., Limousin, M., et al. 2015, MNRAS, 449, 3171

Bond, J. R., Cole, S., Efstathiou, G., & Kaiser, N. 1991, ApJ, 379, 440

Cabanac, R. A., Alard, C., Dantel-Fort, M., et al. 2007, A&A, 461, 813

Coe, D., Benítez, N., Sánchez, S. F., et al. 2006, AJ, 132, 926

Couchman, H. M. P., Thomas, P. A., & Pearce, F. R. 1995, ApJ, 452, 797

Dalal, N., Holder, G., & Hennawi, J. F. 2004, ApJ, 609, 50

Despali, G., Giocoli, C., Angulo, R. E., et al. 2016, MNRAS, 456, 2486

Despali, G., Giocoli, C., & Tormen, G. 2014, ArXiv e-prints

Eisenstein, D. J., Zehavi, I., Hogg, D. W., et al. 2005, ApJ, 633, 560

Eke, V. R., Cole, S., & Frenk, C. S. 1996, MNRAS, 282, 263

Fu, L., Semboloni, E., Hoekstra, H., et al. 2008, A&A, 479, 9

Gao, G. J., Jing, Y. P., Mao, S., Li, G. L., & Kong, X. 2009, ApJ, 707, 472

Gao, L., White, S. D. M., Jenkins, A., Stoehr, F., & Springel, V. 2004, MNRAS, 355, 819

Giocoli, C., Meneghetti, M., Bartelmann, M., Moscardini, L., & Boldrin, M. 2012a, MNRAS, 421, 3343

Giocoli, C., Meneghetti, M., Ettori, S., & Moscardini, L. 2012b, ArXiv e-prints

Giocoli, C., Moreno, J., Sheth, R. K., & Tormen, G. 2007, MNRAS, 376, 977

Giocoli, C., Tormen, G., Sheth, R. K., & van den Bosch, F. C. 2010, MNRAS, 404, 502

Giocoli, C., Tormen, G., & van den Bosch, F. C. 2008, MNRAS, 386, 2135

Gonzalez, A. H., Stanford, S. A., Brodwin, M., et al. 2012a, ArXiv e-prints

Grossman, S. A. & Narayan, R. 1988, ApJ, 324, L37

Hernquist, L. 1990, ApJ, 356, 359

Jing, Y. P. & Suto, Y. 2002, ApJ, 574, 538

Laureijs, R., Amiaux, J., Arduini, S., et al. 2011, ArXiv e-prints

Luppino, G. A., Gioia, I. M., Hammer, F., Le Fèvre, O., & Annis, J. A. 1999, A&AS, 136, 117

Macciò, A. V., Dutton, A. A., & van den Bosch, F. C. 2008, MNRAS, 391, 1940

Mead, J. M. G., King, L. J., Sijacki, D., et al. 2010, MNRAS, 406, 434

Meneghetti, M., Argazzi, R., Pace, F., et al. 2007, A&A, 461, 25

Meneghetti, M., Bartelmann, M., & Moscardini, L. 2003a, MNRAS, 340, 105

Meneghetti, M., Bartelmann, M., & Moscardini, L. 2003c, MNRAS, 346, 67

Meneghetti, M., Bolzonella, M., Bartelmann, M., Moscardini, L., & Tormen, G. 2000, MNRAS, 314, 338

Meneghetti, M., Fedeli, C., Pace, F., Gottlöber, S., & Yepes, G. 2010a, A&A, 519, A90+

Meneghetti, M., Fedeli, C., Zitrin, A., et al. 2011, A&A, 530, A17+

Meneghetti, M., Melchior, P., Grazian, A., et al. 2008, A&A, 482, 403

Meneghetti, M., Rasia, E., Merten, J., et al. 2010b, A&A, 514, A93+

Meneghetti, M., Rasia, E., Vega, J., et al. 2014, ApJ, 797, 34

More, A., Cabanac, R., More, S., et al. 2012, ApJ, 749, 38

Narayan, R. & Bartelmann, M. 1996, ArXiv Astrophysics e-prints

Navarro, J. F., Frenk, C. S., & White, S. D. M. 1997, ApJ, 490, 493

Neto, A. F., Gao, L., Bett, P., et al. 2007, MNRAS, 381, 1450

Newman, A. B., Treu, T., Ellis, R. S., & Sand, D. J. 2011, ApJ, 728, L39+

Planck Collaboration, Ade, P. A. R., Aghanim, N., et al. 2013, ArXiv e-prints

Planck Collaboration, Ade, P. A. R., Aghanim, N., et al. 2014, A&A, 571, A16

Planck Collaboration, Ade, P. A. R., Aghanim, N., et al. 2011, A&A, 536, A1

Postman, M., Coe, D., Benítez, N., et al. 2012, ApJS, 199, 25

Press, W. H. & Schechter, P. 1974, ApJ, 187, 425

Puchwein, E., Bartelmann, M., Dolag, K., & Meneghetti, M. 2005, A&A, 442, 405

Rasia, E., Meneghetti, M., Martino, R., et al. 2012, New Journal of Physics, 14, 055018

Refregier, A. 2003, MNRAS, 338, 35

Refregier, A., Amara, A., Kitching, T. D., et al. 2010, ArXiv e-prints

Sartoris, B., Biviano, A., Fedeli, C., et al. 2016, MNRAS, 459, 1764

Schulz, A. E., Mandelbaum, R., & Padmanabhan, N. 2010, MNRAS, 408, 1463

Scoville, N., Aussel, H., Brusa, M., et al. 2007, ApJS, 172, 1

Seidel, G. & Bartelmann, M. 2007, A&A, 472, 341

Sheth, R. K. & Tormen, G. 1999, MNRAS, 308, 119

Sheth, R. K. & Tormen, G. 2004, MNRAS, 349, 1464

Springel, V., Yoshida, N., & White, S. D. M. 2001a, New Astronomy, 6, 79

Torri, E., Meneghetti, M., Bartelmann, M., et al. 2004, MNRAS, 349, 476

van den Bosch, F. C., Tormen, G., & Giocoli, C. 2005, MNRAS, 359, 1029

Xu, B., Postman, M., Meneghetti, M., Coe, D. A., & Clash Team. 2015, in American Astronomical Society Meeting Abstracts, Vol. 225, American Astronomical Society Meeting Abstracts, 418.03

York, D. G., Adelman, J., Anderson, Jr., J. E., Anderson, S. F., & SDSS Collaboration. 2000, AJ, 120, 1579

Zel'Dovich, Y. B. 1970, A&A, 5, 84

Zhao, D. H., Jing, Y. P., Mo, H. J., & Bnörner, G. 2009, ApJ, 707, 354

Zhao, D. H., Jing, Y. P., Mo, H. J., & Börner, G. 2003, ApJ, 597, L9